AUTOMATED SPORE ANALYSIS USING BRIGHT-FIELD IMAGING AND RAMAN MICROSCOPY

by

Phillip G. Wilcox

A dissertation submitted to Johns Hopkins University in conformity with the requirements for the degree of Doctor of Philosophy

Baltimore, Maryland

January 2020

ABSTRACT

In 2015, it was determined that the United States Department of Defense had been shipping samples of *B. anthracis* spores which had undergone gamma irradiation but were not fully inactivated. In the aftermath of this event alternative and orthogonal methods were investigated to analyze spores determine their viability. In this thesis we demonstrate a novel analysis technique that combines bright-field microscopy imaging with Raman chemical microscopy.

We first developed an image segmentation routine based on the watershed method to locate individual spores within bright-field images. This routine was able to effectively demarcate 97.4% of the *Bacillus* spores within the bright-field images with minimal over-segmentation. Size and shape measurements, to include major and minor axis and area, were then extracted for 4048 viable spores which showed very good agreement with previously published values. When similar measurements were taken on 3627 gamma-irradiated spores, a statistically significant difference was noted for the minor axis length,

ratio of major to minor axis, and total area when compared to the non-irradiated spores. Classification results show the ability to correctly classify 67% of viable spores with an 18% misclassification rate using the bright-field image by thresholding the minimum classification length.

Raman chemical imaging microscopy (RCIM) was then used to measure populations of viable, gamma irradiated, and autoclaved spores of *B. anthracis* Sterne*, B. atrophaeus. B. megaterium,* and *B. thuringiensis kurstaki*. Significant spectral differences were observed between viable and inactivated spores due to the disappearance of features associated with calcium dipicolinate after irradiation. Principal component analysis was used which showed the ability to distinguish viable spores of *B. anthracis* Sterne and *B. atrophaeus* from each other and the other two *Bacillus* species.

Finally, Raman microscopy was used to classify mixtures of viable and gamma inactivated spores. A technique was developed that fuses the size and shape characteristics obtained from the bright-field image to preferentially target viable spores. Simulating a scenario of a

A practical demonstration of the technique was performed on a field of view containing approximately 7,000 total spores of which are only 12 were viable to simulate a sample that was not fully irradiated. Ten of these spores are properly classified while interrogating just 25% of the total spores.

Primary Reader: Jin U. Kang

Secondary Reader: Amy C. Foster

ACKNOWLEDGEMENTS

I would like to thank all the members of the Combat Capabilities Development Command Chemical Biological Center (CCDC CBC) Spectroscopy Branch for their support throughout this effort. Specifically, Drs. Ashish Tripathi, Jason Guicheteau, Darren Emge, Erik Emmons, and Steven Christesen for teaching me how to be a researcher since I started working there in 2005 knowing nothing about spectroscopy. Dr. Tripathi, in particular, has been extremely helpful with this effort and I'm eternally grateful for allowing me to latch onto his project (and funding) and allowing me to expand it to cover the work presented in this thesis.

Additionally, I'd like to thank my advisor Dr. Jin U. Kang and my CCDC CBC supervisor Mr. Richard Vanderbeek. The two of them were both extremely helpful and understanding as I tried to juggle my Ph.D. studies along with a full time job.

Finally, I'd like to thank my Sarah, Grant, and Cynthia for their patience and support through the late nights and weekends as I've been finalizing my "book."

Acknowledgments

Funding for the work presented in this thesis was provided by the United States Army via the In-house Laboratory Independent Research Program (PE 0601101A Project 91A) at the Combat Capabilities Development Command Chemical Biological Center.

CONTENTS

LIST OF TABLES

LIST OF FIGURES

CHAPTER 1

INTRODUCTION

1.1 Thesis Statement and Outline

The objective of this thesis is to develop a novel method using optical technologies to detect and screen for viable bacterial spores. Specifically an optical sensing method that rapidly and non-destructively screens *Bacillus* spores to determine their viability (i.e., capability of causing infection) was developed and validated. The current methodology to determine bacterial viability requires a sampling of spores to be placed into growth media and monitored for 14 days to confirm a lack of germination. This dissertation will detail an optical imaging technique that integrates two analysis methods, bright-field microscopic imaging and Raman microscopy, to more rapidly determine spore viability. These techniques are first studied individually and then fused into a single smart-targeting system.

1.2 Threats from Biological Agents

Methods of biological warfare (BW) have been documented since at least the 6th century B.C when militaries attempted to poison well water with toxic fungi and herbs [1, 2]. Later, around 400 B.C., the first documented cases of projectile BW assaults occurred when archers contaminated their arrowheads with feces and decaying flesh [1]. In the Middle Ages, the projectile attack evolved to include having cadavers, dead animals, and fecal waste launched over city walls via catapult [2]. In the 1700's, blankets from hospitals treating smallpox patients were given to Native American tribes with the intention of infecting the recipients [1-3].

These crude methods became more sophisticated leading up to World War I with the acceptance of germ theory and birth of modern microbiology. These developments allowed for specific pathogens to be identified, isolated, and produced in quantities for weaponization. During World War I, the German army reportedly used *Bacillus anthracis* and *Burkholderia mallei* to infect livestock destined for the United States and other Allied countries with the intention of spreading anthrax and glanders, respectively, however, these BW efforts had little strategic impact on the German war effort [1-3]. The much more widespread use of chemical weapons in World War I led to the international community to form an agreement against the use of weapons of mass destruction which included BW threats. In 1925, the Geneva Protocol (officially the "Protocol for the Prohibition of the Use in War of Asphyxiating, Poisonous, or Other Gases and of Bacteriological Methods of Warfare") was signed by 108 countries [1-3].

The Geneva Protocol, however, did not curtail research in BW. The Protocol only prohibited BW *use* and not research or development. Additionally, it had no method of

verification or compliance and several signatories began BW programs after ratification [1-3]. France, the Soviet Union, and Great Britain publicly stated that the agreement would not prevent them from retaliating in kind if attacked by chemical or biological weapons first [1].

During World War II, the notorious Japanese Unit 731 experimented on prisoners of war with *Bacillus anthracis* (anthrax), *Clostridium botulinum* (botulism), *Clostridium perfringens* (gas gangrene), *Neissseria meningitides* (meningitis), *Vibrio cholera* (cholera), *Shingella* spp (shigellosis), and *Yersinia pestis* (plague) which led to more than 10,000 deaths [1, 2]. Germany also infected prisoners with pathogens during World War II including *Rickettsia prowazekii* (typhus), hepatitis A, and malaria, but did not have an offensive BW program [1, 2]. The British government researched anti-crop and anti-animal biological agents. As part of their research, *Bacillus anthracis* spores were released on Gruinard Island off the Scottish coast which resulted in the island being uninhabitable for 48 years until it was decontaminated in 1990 [1, 4, 5]. The success of the testing at Gruinard Island resulted in the British government making 5 million feed cakes for cattle contaminated with *B. anthracis* to retaliate against a potential German BW attack, however these were never used [1].

The United States did not ratify the Geneva Protocol until 1975 and also built up a BW program through World War II which included the establishment of Camp Detrick (now known as Fort Detrick) in 1943 [1-3]. Camp Detrick had pilot plants that were used to produce *B. anthracis*, botulinum toxin, and *B. globigii* (non-pathogenic *anthracis* surrogate) [1]. Dispersal methods were also being developed which included the SPD MK I anthrax bomb. The United States government placed an order for 1 million of these

bombs, but cancelled it at the conclusion of World War II [1]. Eventually, the United States military scientists weaponized seven biological agents: *B. anthracis*, botulinum toxin, *Francisella tularensis* (tularemia), *Brucella suis* (swine brucellosis), Staphylococcal enterotoxin B (toxic shock syndrome), and Venezuelan equine encephalitis virus [3]. The United States government had facilities capable of producing 650 tons per month to load into weaponry [6]. This program was abandoned in 1969 with an executive order signed by Richard Nixon [1, 6]. Three years later, the Convention on the Prohibition of the Development, Production and Stockpiling of Bacteriological (Biological) and Toxin Weapons and on their Destruction was created. This treaty, commonly referred to as the Biological Warfare Convention (BWC), went further than the Geneva Protocol by prohibiting not just the use of biological weapons, but the "development, production, and stockpiling" of BW materials as well as dissemination systems [1]. Furthermore, the signatories were required to destroy agent stockpiles and weapons after ratification. However, like the Geneva Protocol before it, the BWC had no method for inspection or verification [1, 2].

Few of the early details of the Soviet BW program are known, however, ratifying the BWC did not stop their research. In 1979, the town of Sverdlosk experienced an outbreak of respiratory anthrax that was eventually determined to have been an accidental release of over 100 g of *B. anthracis* spores from a military facility which resulted in 105 deaths. The Soviet BW program eventually developed antibiotic resistant strains of *Y. pestis*, *B. anthracis*, and *B. mallei*, and *F. tularensis* that could be loaded into weaponry and ready to deploy in about a week [1]. Iraq began its BW program two years after signing the BWC in 1974. Despite claims from the Iraqi government that they abandoned their program at

the end of the Persian Gulf War in 1991, they were believed to have had stockpiled 380,000 liters of Botulinum toxin, 84,250 liters of *B. anthracis* spores, and 3,400 liters of *C. perfringens* spores as well as weapons delivery systems [6].

In addition to these state sponsored BW programs, bioterror threats also exist from smaller non-state groups. In 1981 a group called Dark Harvest delivered *anthracis* contaminated soil from Gruinard Island to the British BW research facility at Porton Down and the site of a Conservative Party political meeting to protest the island's continued contamination [1]. In 1984, the Rajneeshee cult contaminated a salad bar in The Dalles, Oregon with *Salmonella typhimurium* causing 751 people to fall ill with gastroenteritis [1]. During an investigation of Aum Shinrikyo, the group responsible the Sarin gas attack on the Tokyo subway system in 1995, it was discovered that the group had attempted at least eight times to infect the Tokyo population with *B. anthracis* spores and botulinum toxin between 1990 and 1995 [1, 7]. And in 2001, shortly after the attacks of September 11th, letters filled with *B. anthracis* spores were through the mail to politicians, journalists, and the media leading to the exposure of thousands of individuals and five deaths. Additionally this incident, known as Amerithrax, closed 35 postal facilities, 26 buildings on Capitol Hill, and required $27 million from the Environmental Protection Agency for decontamination [1, 7, 8].

1.2.1 Inadvertent Anthrax Mailing

The long history of biological warfare means that governments need to be prepared to protect their soldiers and general populations with items such as personal protective equipment, detectors, and medical treatments, as well as strategic planning such as

evacuation routes, triage, and decontamination. As such, a significant amount of biodefense research is performed by federal agencies, private contractors, and academic institutions which requires the shipment of bacteria, spores, and toxins around the US and the globe to aid in testing and validation. When testing new equipment and procedures it is desirable to use materials as close to the true threat as safely possible. *B. anthracis*, which has been extensively studied as a BW threat, is rated as a bio-safety level 3 (BSL-3). This means that the bacteria can only be used at certified facilities with specialty trained personnel and engineering controls which adds cost and complexity to development and testing. There are two main methods to overcome this burden. The first is to use a surrogate material at a lower BSL [9]. The second is to take the virulent bacteria and inactivate it so it is longer capable of causing illness. In the case of *B. anthracis* spores this is typically done using three main methods: wet heat, chemical treatment, or gamma-irradiation [10-12].

Of these three inactivation methods, gamma irradiation has become the most widely used because the effects to the spore structure and physical properties are minimal compared to wet heat and chemical inactivation. Additionally, gamma inactivated spores can be used to test detection assays using antibodies and polymerase chain reaction (PCR) without effecting the sensitivity compared to viable *B. anthracis* spores [12, 13].

To ensure the safety of the receiving laboratories, these materials are confirmed to be inactive through a two week monitoring of a sampling of spores on media to ensure that no growth occurs. Despite this procedure, it came to light in 2015 that the United States Department of Defense had been inadvertently shipping samples that were not fully inactivated. In the aftermath of this discovery, an analysis was performed of the

inactivation procedures which found inconsistencies in the procedures performed in different laboratories [14]. This resulted in the creation of a standard method to be used gamma irradiation of *B. anthracis* spores [12].

The new method set a metric for efficacy by using the sterility assurance level (SAL). The SAL is a term used for medical devices and pharmaceuticals that have been sterilized with radiation. The new method sets a target sterility assurance level (SAL) of 10^{-6} meaning that there should be one or fewer viable spores for every million sampled [12, 15].

To confirm inactivation samples are still placed into growth media and monitored for lack of growth over 14 days, however, the effort presented in this thesis demonstrates a novel optical method to confirm spore deactivation which can serve as an orthogonal technique to this existing procedure.

1.3 *Bacillus* Endospores

As described in Section 1.2, the idea of using *Bacillus anthracis* as a bioweapon has been around since at least World War I with research being performed at some level by numerous state programs and terrorist organizations continuously since that time [1-3, 7, 16, 17]. *B. anthracis* is an appealing bioweapon for a number of reasons. First, the spores are naturally occurring and can be easily found in nature. Once obtained, the process to replicate the spores in a laboratory environment is relatively easy [18]. Additionally, the spores themselves have a long shelf life with no special storage restrictions (i.e. refrigeration) and are resistant to heat, ultraviolet (UV) radiation, and chemicals [19]. The sporulated form is also easily disseminated as a spray, powder, or in contaminated food. Finally, the infection caused by the spore has serious (potentially fatal) health effects with

symptoms appearing from 1 day to 2 months after exposure [20]. The following sections detail the composition of *Bacillus* spores, the health effects from exposure, how spore viability is currently determined, and information about the spores used in this effort.

1.3.1 Spore Composition

The term "spore" refers to a lifecycle stage of certain bacteria that occurs when a vegetative cell enters a nutrient deficient environment. There are different types of sporulation processes, but bacteria in the phylum Firmicutes (which includes *B. anthracis*) generate endospores. It should be noted that other phyla generate different types of spores (e.g., Actinomycetes generate exospores and Cyanobacteria generate akinetes [21]), but in this paper the term spore refers specifically to bacterial endospores.

In order to prevent starvation, a vegetative *Bacillus* cell undergoes a five stage process to create a spore as shown in Figure 1.1. First, the cell undergoes an asymmetric division with a copy of the cell's DNA in each partition. The smaller section is called the prespore with the larger portion being called the mother cell. Next, the mother cell engulfs the prespore. The DNA from the mother cell is then broken down and the cortex made of peptidoglycan is created around the prespore which is now called a forespore. Subsequently the mother cell produces dipicolinic acid and removes moisture from the forespore. Finally, the outer coat hardens and the mother cell dissolves to release the now dormant spore. The spore can remain viable in this state for years [22, 23] and will germinate into a vegetative cell when habitable conditions are present [19, 21, 24].

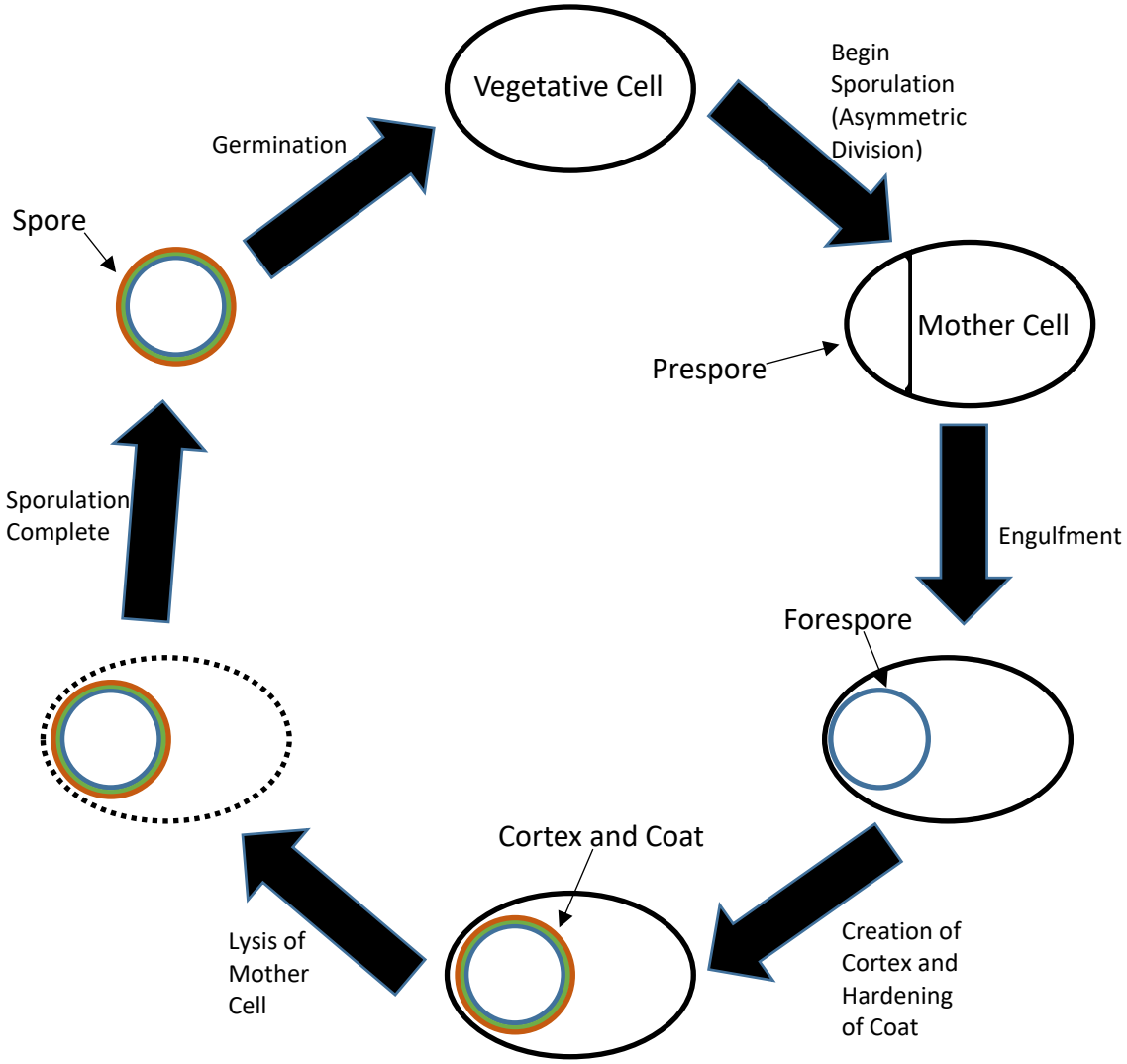

Figure 1.1. Sporulation process for *B. anthracis*

The spores themselves are made up of concentric shells centered on the core as shown in Figure 1.2. The core contains the spore's genetic information and has a low water concentration. It also has proteins known as small acid-soluble proteins (SASPs) and a high concentration of calcium dipicolinate (CaDP). This combination of low moisture, SASPs, and CaDP are believed to provide the spore's protection from heat and UV degradation. Outside the core is the cortex. The cortex is made of peptidoglycan and is believed to keep the moisture level low inside the core. Outside the cortex is the spore

coat. The coat is a multilayered shell made primarily of protein. These proteins are crosslinked, which is believed to give the spore some of its resistance to chemical degradation. The outermost layer of the *B. anthracis* spore is another protein layer known as the exosporium. The exosporium layer is not consistent across the endospore forming species. Some *Bacillus* species do not have an exosporium layer at all. Although research has been done on the specific proteins that make up this layer, its exact function is unknown. However it is not believed to offer any specific protection to the spore against heat, UV, or chemical degradation [19, 21, 24].

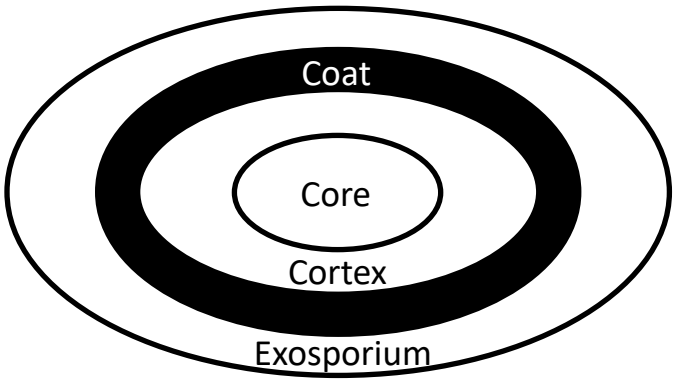

Figure 1.2. Schematic of *B. anthracis* endospore structure (not to scale).

1.3.2 *Bacillus anthracis* Health Hazards

When a *B. anthracis* spore enters a host body the spore reactivates to its vegetative state and multiplies in the body. These cells release a toxin which can lead to illness or death, which is known as an anthrax infection. There are three main methods of anthrax exposure: cutaneous, gastrointestinal, and inhalation.

Cutaneous anthrax occurs when spores enter the body through breaks or scratches in skin and is the most common method of infection accounting for nearly 95% of reported

cases. These infections typically occur in people working with animals who were infected while grazing and their products (wool, hides, or hair). There is an incubation period of 1-12 days which results in a lesion with a characteristic black center as shown in Figure 1.3. Additional fever and inflammation can occur. The mortality rate for untreated infections is between 5 and 20%. With proper treatment this rate decreases to <1%. A new subset of cutaneous anthrax infections have been identified in recent years known as injection anthrax infections. The form of infection has been reported in some intravenous drug users in Europe. The symptoms of this form of infection are similar to traditional cutaneous infections, but the infection occurs deeper under the skin which causes the infection to spread more rapidly through the body.

Figure 1.3. Example of cutaneous anthrax lesion (Image from Centers for Disease Control and Prevention Public Health Image Library [25]).

Gastrointestinal anthrax occurs when meat contaminated with the spores has been ingested. The symptoms from this exposure route cause flu like symptoms (fever, chills, headache, nausea, vomiting, and diarrhea), which makes it difficult to diagnose. Depending on where the spores first germinate, this infection will either be located in the

throat (oropharyngeal) or intestines, resulting in ulcers. The mortality rate for gastrointestinal anthrax is estimated to be between 25 and 60%.

Inhalation anthrax occurs when the spores are breathed in and deposited on the host's alveoli. The spores then migrate to the lymph nodes where they germinate and result in inflammation of the chest cavity. After approximately 4 days the host will develop flu like symptoms similar to gastrointestinal anthrax along with a nonproductive cough. This is followed by a drop in blood pressure and shortness of breath. This form of infection used to be common among millworkers being exposed to contaminated animal hides. Prior to 1976 these naturally occurring inhalation exposures had a mortality rate of 94%, however, during the 2001 Amerithrax attacks the mortality rate was 46%. This improvement has been attributed to earlier diagnosis and better treatment including the use of multi-drug antibiotic regimens. Increased immunization of livestock and improved working conditions have drastically reduced the number of inhalation anthrax cases worldwide, however the case of a bioweapon dissemination of *B. anthracis* inhalation anthrax is expected to be the most common route of infection.

1.3.3 Existing Methods to Determine Spore Viability

Determining a spore's viability is traditionally performed using one of few long-standing methods. The first, and most widely used method, is to culture the sample and wait to observe growth (or lack thereof) as shown in Figure 1.4, however this can take days to confirm lack of growth [14, 26]. Another set of methods uses PCR or quantitative PCR (qPCR) to amplify DNA fragments. Although this method does not always discriminate the DNA from non-viable cells from the DNA from viable cells, sample preparation

methods have been demonstrated which can prevent the DNA from non-viable cells from being replicated [27, 28]. To perform PCR the DNA needs to first be extracted from the sample with the PCR process itself taking minutes to hours to complete [27, 29]. A third option involves the use of fluorescent stains or assays which can be used with flow cytometry [30] or optical microscopy [31-35]. In order to screen a large number of spores the ideal method would require minimal sample preparation and rapid acquisition of data. Using a method based on bright-field microscopy provides an approach that can be used to quickly measure a large number of spores. Combining this method with an additional analytical technique such as Raman spectroscopy improves the confidence in the final determination of viability. Previously, Raman microscopy has demonstrated the ability to discriminate between bacterial species and strains using both normal Raman [36-38] and surface enhanced Raman spectroscopy (SERS) [39-41]. Additionally, Raman spectral differences have been documented between viable and non-viable *Bacillus* spores that were inactivated using wet-heat [42, 43], cold atmospheric plasma [44], and chemical (formalin) [40] methods. In this effort we examine spores inactivated using gamma irradiation. The combination of bright-field and Raman imaging techniques is well suited for spore screening because they are both are non-contact, non-destructive, and reagent-less.

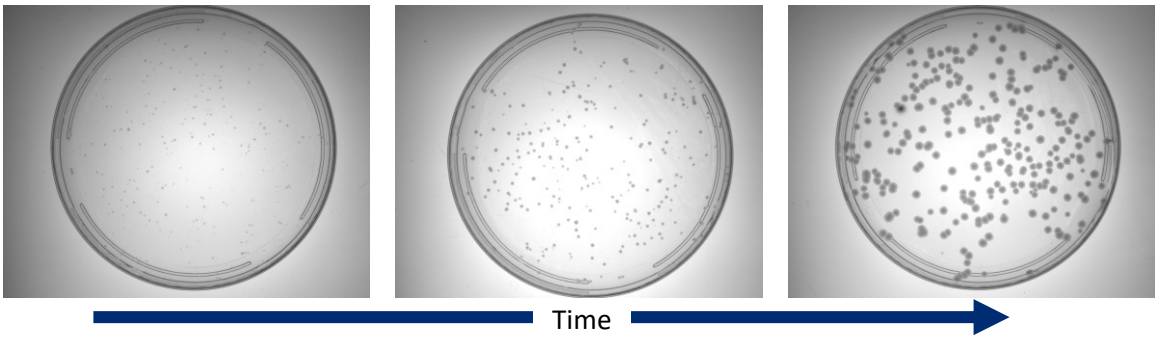

Figure 1.4. Example of spore growth monitored over time.

1.3.4 Spore Samples used for this Effort

The work presented in this thesis used four different *Bacillus* species. The majority of the work was performed on the same batch of *Bacillus anthracis* Sterne (34F2) spores which were obtained from the Naval Surface Warfare Center – Dahlgren Division Chemical Biological Radiological Defense Division. Sterne is an attenuated strain of *B. anthracis* that is missing the plasmid that normally protects the bacteria from the body's immune response [45]. This results in a spore that maintains much of the physical and chemical composition of a virulent *B. anthracis* strain (i.e. Ames) but is avirulent and has not resulted in a human anthrax infection [45]. Because of this, the Sterne strain is commonly used as a vaccine against [45] or surrogate for [9] the virulent strain.

Stock suspensions of 1-2 × 10^{10} cfu/ml viable and gamma deactivated spores were prepared in 18.3 MΩ water. The gamma deactivation was achieved by exposing the spores to a 40 kGray gamma radiation dosage. The viability of unexposed and deactivation of gamma radiation exposed spore samples was confirmed using traditional growth methods. The viable spores were tested for and demonstrated growth within two days on sheep blood agar plates. The gamma irradiated spore deactivation was confirmed by the absence of growth in tryptic soy broth over a 2 week incubation period.

The viable and gamma deactivated spores were cleaned by centrifuging the suspension at 10000 rpm for 5 minutes and discarding the supernatant liquid. The suspension was remade by adding the same volume aliquot of nanopure water that was removed as supernatant liquid. This process was repeated 3 times.

Section 3.6 includes data collected from *B. thuringiensis kurstaki* (American Type Culture Collection [ATCC] 33679), *B. megaterium* (ATCC 9885), and *B. atrophaeus*

(ATCC 9372). This section also includes measurements using a different preparation of *B. anthracis* Sterne from the one described above. For all four of these samples, a base Difco sporulation medium (DSM) consisting of the following composition was used: 8 g/L nutrient broth (NB, Difco), 2.15 g/L KH_2PO_4 (Sigma Aldrich), and 4.39 g/L K_2HPO_4 (Sigma Aldrich), which was sterilized at 121ºC for 30 min in an autoclave (Tomy ES-315). The sterilized base DSM was further supplemented with 40 mL of a 0.2 μm filtered pre-sterilized (Corning) sporulation salt stock solution (CCY). The CCY stock consisted of: 7.35 g/L $CaCl_2 \cdot 2H_2O$, 0.99 g/L $MnCl_2 \cdot 4H_2O$, 10.17 g/L $MgCl_2 \cdot 6H2O$, 0.0081 g/L $FeCl_3$, and 0.34 g/L $ZnCl_2$. All CCY stock components were purchased from Sigma Aldrich except $ZnCl_2$, which was from Fisher scientific.

A glycerol-frozen stock of each strain was streaked onto a NB agar plate and incubated at 37 ºC overnight (VWR 3025 B). A single colony of each strain was inoculated into 1 L of DSM medium in a 4 L flask and incubated at 34 ºC and 200 rpm. When the percentage of spores reached greater than 95% under a phase-contrast microscope (Olympus BX51) after 2 to 3 days, the spore suspension was centrifuged (Beckman Avanti J-25I) at 10000 rpm for 10 minutes and triple washed with pre-sterilized deionized water and concentrated to approximately 100 mL each.

The spores for Section 3.6 were deactivated using two different methods. The first was a heat deactivation in which a 0.5 mL aliquot of each washed and concentrated strain was placed in a 2 mL screw cap glass vial and sterilized in an autoclave (Tomy ES-315) at 121 ºC for 30 min. The second was with a 50 kGray dose of gamma irradiation (as opposed to the 40 kGray dosage used for the previous samples) using a Cobalt-60 Irradiator (Model 484R, JL Shepherd & Associates). After both of these deactivation methods, 0.1 mL of

each inactivated strain was inoculated into 250 mL of DSM in a 1L flask and incubated at 30 ºC and 225 rpm for 2 weeks. No re-germination/growth was evident in each of the heat and gamma radiation deactivated spores.

For all the samples analyzed in this thesis, inactivated spore suspensions were diluted to a concentration of 1-2 × 10^9 cfu/ml while suspensions of the viable spores ranged from 1-2 × 10^9 cfu/ml to 1-2 × 10^7 cfu/ml. These suspensions were then deposited onto an aluminum coated microscope slide (EMF, AL136). The water was allowed to dry resulting in a residue of *Bacillus anthracis* Sterne spores for imaging and Raman analyses.

1.4 Optical Microscopy

1.4.1 Principles of Microscopy

Microscopy is a common method used to view small items. Optical microscopy uses light to image the items. When light passes through a small aperture (such as a microscope objective) the resulting output is a diffraction pattern known as an airy disk which has its highest intensity in the center surrounded by concentric rings of constructive and destructive interference. The lateral resolution is the smallest distance that can be distinguished as unique in an optical system. The theoretical resolution limit, δ, is defined as the distance from the peak to the first minimum of the airy disk, which depends on the wavelength of light, λ, and the numerical aperture (NA) of the collection optics. This first minimum in the airy disk corresponds to the first zero of the first order Bessel function which occurs at 1.22. The NA is defined using the following equation:

$$NA = n \sin\theta \approx n\frac{D}{2f} \tag{1.1}$$

where n is the index of refraction of the transmission medium which is equal to 1 (air) for this effort, θ is the half angle of the cone of light that can be collected by the objective lens, f is the focal length of the lens and D is the diameter of the entrance pupil. This leads to the resolution limit (also known as the Rayleigh criterion) being defined using the following equation [46]:

$$\delta = 1.22\frac{f\lambda}{D} = 0.61\frac{\lambda}{\mathrm{NA}} \tag{1.2}$$

All microscope images for this effort were collected with a Witec (Ulm, Germany) Alpha 300R using a Zeiss EC Epiplan-Neofluar DIC 100x objective with a NA of 0.9. Using the center wavelength of white light at 550 nm leads to a lateral resolution limit of 0.37 μm for this system.

The depth of field (d_{tot}, also referred to as depth of focus) is the thickness of the focal plane which is properly imaged onto the detector and is determined using the equation [46]:

$$d_{tot} = \frac{\lambda n}{\mathrm{NA}^2} + \frac{n}{M\cdot\mathrm{NA}}e \tag{1.3}$$

The magnification, M, and NA are determined by the microscope objective and e is equal to the smallest distance capable of being resolved by the detector which was 6 μm for the Imaging Source (Charlotte, NC) 752×480 CMOS camera installed in the microscope system. This leads to a depth of field equal to 0.75 μm for this configuration.

1.4.2 Contrast Generation in Optical Microscopy

Contrast is required in order to adequately visualize the features of a sample. Many microscopy samples tend to be transparent with features only slightly different from their surroundings. To overcome these limitations a number of different illumination techniques

are used. A summary of four of the most common methods, bright-field illumination, dark-field illumination, phase contrast, and fluorescence are described below.

Bright-Field Illumination

The most common type of microscope illumination which generates contrast due to changes in sample absorption, the index of refraction, or color. Schematics showing the ray path through in a bright-field microscopy system are shown in Figure 1.5. The illumination source either passes through (transmission) or reflects off of (epi-illumination) a sample. The light is collected and focused onto the sample in the specimen plane and collected by the objective where it can either be imaged using a camera or viewed by eye. When no sample is present, the illumination light is still collected by the objective causing the image to appear bright, leading to its name.

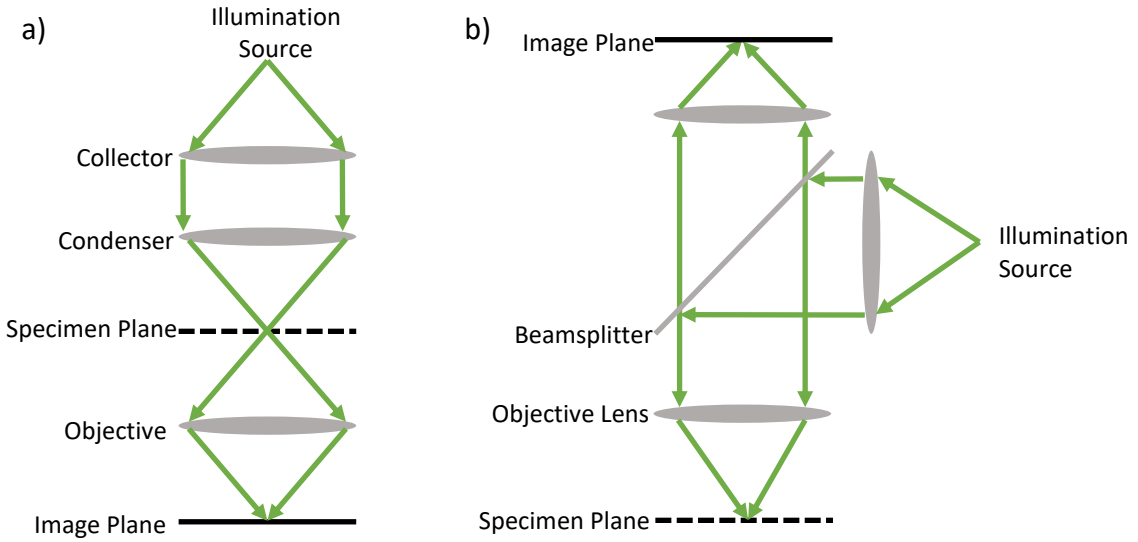

Figure 1.5. Ray path for bright-field microscopy system using a) transmission and b) reflection illumination.

Because of the bright background using this type of microscopy, it can be difficult to view transparent and colorless samples. In these cases, sample staining is often used to increase contrast. The spores in this effort were imaged exclusively using bright-field imaging in an epi-illumination configuration to generate pictures like the one shown in Figure 1.6. The scatter from the spore edge provided enough contrast that no staining was necessary for these samples [46].

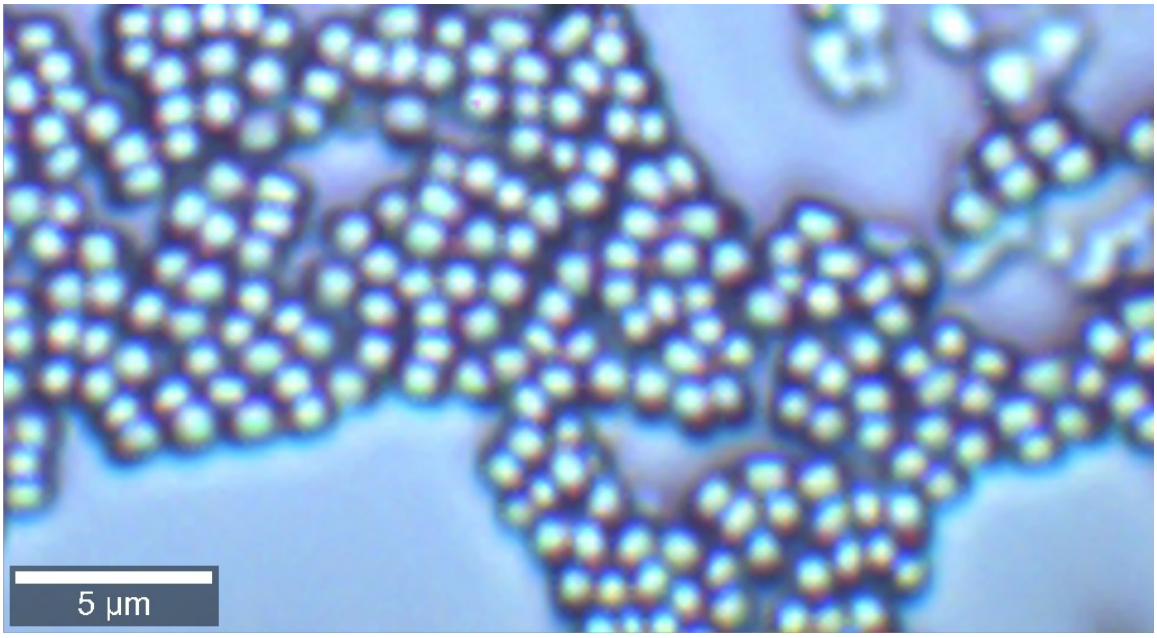

Figure 1.6. Example of bright-field microscopy image of *B. anthracis* Sterne spores at 100× magnification.

Dark-Field Illumination

In dark-field imaging, the illumination light is prevented from being imaged onto the detector when no sample is present. This is typically done by inserting an annular ring at the illumination source which blocks the light from being imaged as shown in Figure 1.7. When a sample is placed into the specimen plane, scattering (shown in orange) causes some of the light rays to be collected by the objective and get imaged onto the detector. This results in bright highlights in the image at regions of discontinuity within the sample [46].

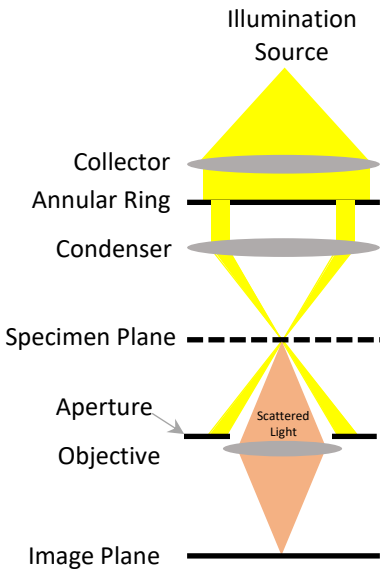

Figure 1.7. Ray path of a dark-field microscopy system.

Phase Contrast Microscopy

Phase contrast microscopy is used for imaging transparent samples by measuring the changes in refractive index or thickness of a sample. This is done by placing a structured aperture, typically an annular ring, at the illumination source as shown in Figure 1.8. A matching phase plate which has a difference in thickness to match the aperture is placed after the specimen plane. This plate causes a phase shift to occur between un-scattered light directly from the illumination source and the light that has been scattered from the sample. When the light is brought to the image plane, the difference in phase between results in interference which increases the image contrast [46].

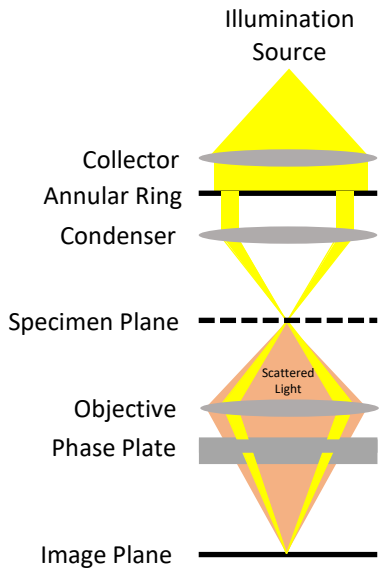

Figure 1.8. Ray path of phase contrast microscopy system.

Fluorescence

Fluorescence is a phenomenon where light is absorbed by a compound (known as a fluorophore) and then re-emitted at a longer wavelength. In fluorescence, the fluorophore absorbs an incident photon which excites an electron to an elevated energy state. As the electron relaxes back to its ground state photons are emitted which correspond to the radiative energy levels in the material.

Some samples naturally fluoresce (known as autofluorescence). For the samples that do not autofluoresce, fluorescent dyes (also known as fluorochromes) can be added. These dyes can be selected and tailored to target specific antibodies or biomarkers to increase the contrast of those features [46, 47].

Fluorescence microscopy can use a variety of different optical configurations to collect the light and improve contrast. Figure 1.9 shows a schematic of an epi-illuminated fluorescence microscopy system. The main difference between a fluorescence microscope

and a bright-field configuration is the addition of excitation and emission filters which can be changed to excite and measure the response of fluorophores with different absorption and emission characteristics. The overall resolution is determined by the diffraction limit of the fluorescence emission wavelength [48].

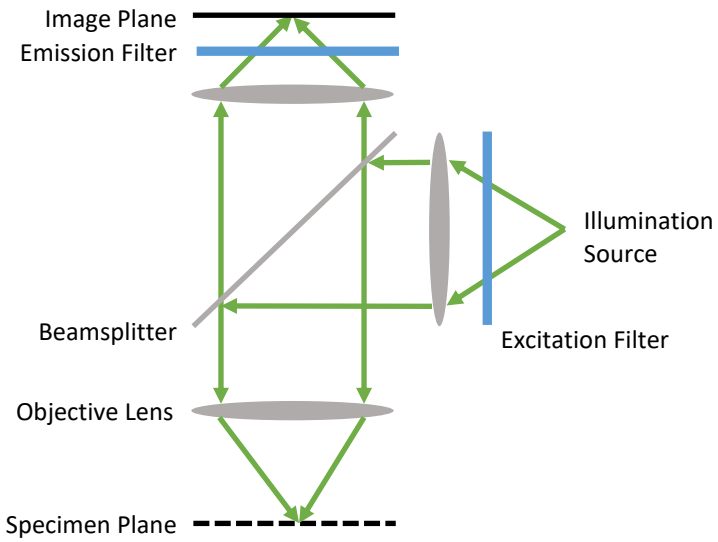

Figure 1.9. Ray path of epi-illuminated fluorescence microscopy system.

1.4.3 Non-Optical Microscopy Methods

There are two common non-optical microscopy methods that are commonly used to get higher resolution images of samples. Because these methods, scanning electron microscopy (SEM) and atomic force microscopy (AFM), are not optical they are able to resolve features below the diffraction limit of light [49, 50].

In SEM an electron source generates electrons which are then accelerated on the order of 0.1-30 keV. These electrons can be focused to a spot size of approximately 1-10 nm which determines the instrument resolution. This beam is raster scanned over a specimen with the scattered electrons being captured in a detector to generate an image [49].

In AFM a micro-machined cantilever probe is moved over a surface. A laser illuminates at the end of the probe where the light is reflected into a detector. The probe has a sharp tip that is scanned across the sample surface. Variations in the surface causes the cantilever to deflect which causes the laser position to change on the photodetector. These changes can be used to construct an atomic scale image of the surface [50].

1.4.4 Microscopy of Bacterial Spores

The majority of published work on the microscopic imaging of *Bacillus* spores used phase contrast and fluorescence microscopy. These techniques have been used to monitor *Bacillus* spores they undergo germination [51-58], sporulation [52], and inactivation [43, 44]. Bacillus germination has also been monitored using bright-field imaging [56] and differential interference contrast microscopy [58, 59].

Since *Bacillus* spores are similar in size to the diffraction limit of light, non-optical forms of microscopy have been used to gain further insight into their structure and biological processes [60]. Electron microscopy has been used to determine the structure of *Bacillus* cells [60, 61] and monitor the sporulation process [62]. AFM has been used to measure the surface morphology of *B. subtilis* [63] and monitor the chemical inactivation of *B. cereus* [64].

1.5 Raman Microscopy

1.5.1 Principles of Raman Spectroscopy

Raman spectroscopy is an inelastic scattering technique that can be used to identify the chemical bonds present in a sample. In elastic (Rayleigh) scattering, as shown on the left in Figure 1.10, an incident photon of energy $h\nu_o$ impinges onto a sample which is excited to a virtual energy level before decaying back to the initial ground state and emitting a photon of the same energy. In the case of the Stokes Raman scatter, the excited electron instead decays back to an energy level V_j above the ground state which causes the emission of a photon of lower energy $h(\nu_o-\nu_j)$ [65]. If the excitation photon energy is close to an electronic energy band then the Raman return can experience resonance enhancement resulting in signal strength increased by 1000 times or more [66]. An alternative form of Raman scattering is called anti-Stokes. In this case the electron begins at the excited energy level V_j when the incident photon excites it to the virtual energy level, however in this case, the electron relaxes back to the original ground state resulting in the emission of a blue-shifted photon of energy $h(\nu_o+\nu_j)$. For the remainder of this work, Raman spectra refers solely to Stokes scattered light. Infrared absorption spectroscopy is another form of vibrational spectroscopy, however the spectra generated using this technique are indicative of direct absorption of infrared photons.

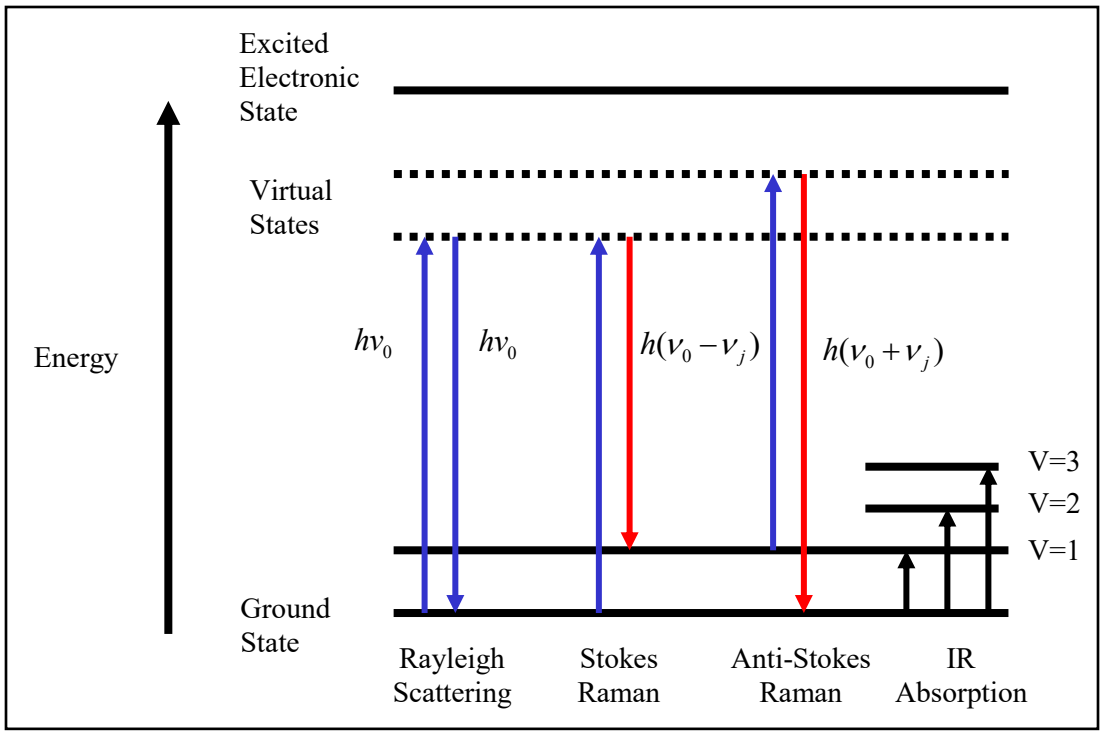

Figure 1.10. Energy diagram showing Rayleigh scatting, Stokes and anti-Stokes Raman scattering, and infrared absorption.

Because these energy levels correspond to chemical bonds within the molecule it is possible to disperse the Raman scattered light onto a spectrometer to get a spectrum that is unique for the measured chemical. The difference between the scattered wavelength, λ_j, and the excitation wavelength, λ_0, is reported as the Raman shift, $\tilde{\nu}$, (typically with the unit of cm^{-1}) using the following equation:

$$\tilde{\nu} = \left(\frac{1}{\lambda_0} - \frac{1}{\lambda_j}\right) \tag{1.3}$$

The Raman shift corresponds directly to the change in energy through the equation:

$$\Delta E = hc\tilde{\nu} \tag{1.4}$$

where h is Planck's constant and c is the speed of light [65].

The region from 500-1800 cm^{-1} is typically referred to as the fingerprint region of the spectrum. This is because organic molecules tend to have spectral features present in this

region that can be used for discrimination. Another important region of a Raman spectrum is the C-H stretch region which occurs close to 3000 cm^{-1} and is associated with carbon-hydrogen bonds. Due to the prevalence of C-H bonds in organic compounds and their large scattering probabilities, these peaks typically have higher intensities than peaks in the fingerprint region. However, they does not have a high specificity meaning that they are not typically useful for chemical identification. Attributing Raman peaks to specific chemical bonds can be challenging due to the complex nature of biological materials [67], however Table 1.1 lists band assignments for components present in general biological specimens [67, 68] combined with band assignments from *Bacillus* spores specifically [43].

Table 1.1. Raman band assignments for biological samples

Frequency (cm^{-1})	Assignment	Ref	Frequency (cm^{-1})	Assignment	Ref
2975	CH_3 stretch	[68]	1099	DNA, O-P-O	[43]
2935	CH_3 and CH_2 stretch	[68]	1085	C-O stretch	[68]
2870-2890	CH_2 stretch	[68]	1061	C-N and C-C stretch	[68]
1668	Amide I (nonregular)	[43]	1018	CaDP	[43]
1655	Amide I (α-helical)	[43]	1004	Phenylalanine	[43, 67, 68]
1602-1606	Phenylalanine	[67, 68]	897	COC stretch	[68]
1575	Guanine, adenine (ring stretching)	[68]	823	CaDP	[43]
1575	CaDP	[43]	783-792	Guanine, uracil, cytosine	[43, 67]
1450	CaDP, C-H_2 deformation	[43]	720-723	adenine	[43, 67, 68]
1440-1460	C-H_2 deformation	[68]	650-665	Guanine	[67, 68]
1402	CaDP	[43]	664	CaDP	[43]
1295	CH_2 deformation	[68]	641	Tyrosine (skeletal)	[67, 68]
1230-1295	Amide III	[68]	620-622	Phenylalanine (skeletal)	[67, 68]
1129	C-N and C-C stretch	[68]			

Raman scattering is a weak process with only 1 in 10^7 photons being Raman active, however the technique does have advantages that make it useful for studying materials. First, the vibrational spectrum generated has high selectivity and allows for spectral matching. There is minimal sample preparation required meaning that there are no

additional stains or dyes required for analysis. When analyzing samples on a substrate, the measured Raman return is not altered due to surface texture or reflectivity like infrared spectra are. Additionally, the technique has minimal interference from water [65].

In general terms, to collect Raman spectra a monochromatic source (e.g., a laser) is impinged onto the sample. Optics are then used to collect the scattered light. Since the Raman signal is significantly smaller than the Rayleigh scatter, an optical filter is then used to remove the elastically scattered light. The remaining light is separated, most commonly with a dispersive spectrometer, and recorded onto a camera or sensor.

1.5.2 Raman Chemical Imaging

Raman chemical imaging is a technique combining the Raman spectral information from a sample with spatial information to generate a 3-dimensional set of data containing spatial information in the x- and y-axes and spectral information along the z-axis. Figure 1.11 shows a schematic of a representative Raman hyperspectral cube (RHSC). In this figure, each square represents a Raman pixel (with the bright-field image shown for reference). The stack of pixels shown in red stores the spectrum shown below. Each x- and y-position has its own corresponding Raman spectrum which makes Raman imaging a good technique for studying the chemical composition of inhomogeneous samples.

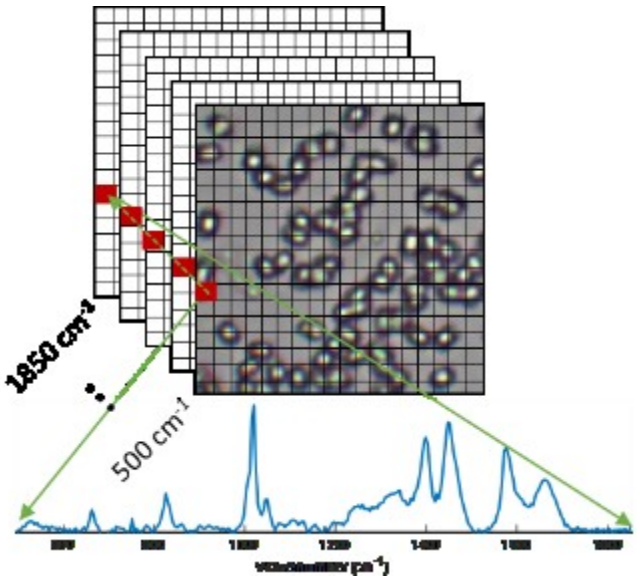

Figure 1.11. Schematic showing an example Raman hyperspectral cube (bright-field image shown on top for reference)

A variety of techniques can be used in order to collect this 3-dimensional data onto 1- or 2-dimensional sensors. Four of the most common methods are tunable filters, push broom scanning, mapped fiber bundles, and raster scanning [69-71].

To collect a hypercube using a tunable filter such as a liquid crystal tunable filter (LCTF) or multi-conjugate filter (MCF), the entire FOV is illuminated with the excitation source. The tunable filter is placed over a 2-dimensional camera with one frame being collected at each wavelength over the filter tuning range. These camera frames are then combined to generate the RHSC. This method can have higher spatial resolution, but is limited by the long integration times required to overcome the low throughput for the optical filters and time required to change collection wavelengths [71].

In push broom scanning, a linear region is illuminated with a laser. The scattering from this region is then sent to a 2-dimensional imaging spectrometer. The imaging spectrometer maintains the spatial dimension along the y-axis, but disperses the light along the x-axis, generating a spectrum for each point across the illuminated line. The linear

region is then shifted a known distance and the process is repeated. At the completion of all the scans, these spectra can be manipulated to create the RHSC of the entire scan area. The push broom method can result in different spatial resolutions along the x- and y-axes and can be slow depending on the scan rate used for the push broom [69].

Using a mapped fiber bundle is somewhat similar to the push broom method, except instead of freespace coupling a linear region into the spectrometer a linear fiber optic array is used at the spectrometer entrance. The other end of the fiber optic bundle is typically laid out in a grid pattern with individual fibers being mapped back to their location at the spectrometer end. Just as in the push broom method, the y-position is maintained in the spectrometer while the light is dispersed along the x-axis, however in this case because the y-position at the spectrometer is mapped to a known x- and y-position at the collection end, the full 3-dimensional RHSC can be reassembled after a single measurement. The advantage of this technique is that the full set of spatial and spectral information is generated in a single scan, however this comes at the expense of significantly reduced spatial resolution [70, 71].

Raster scanning involves taking a series of point measurements while moving a known distance in the x- and y-direction with a single spectrum being collected at each location. At the completion of the scan, all the spectra are combined to generate the RHSC. In general, the spatial resolution is limited by the step size of the stage or steering optics, however in the case of nano-precision microscopy stages the spatial resolution then becomes defined by the diffraction limit of the excitation beam. The time to collect an entire image is set by the image size, step size between each measurements, and scanning speed. Large scans with high spatial resolution can require long acquisition times [71].

1.5.3 Confocal Raman Microscopy

All Raman spectra in this paper were taken using a Witec Alpha 300R confocal Raman microscopy system using 532 nm laser excitation. The generated RHSC were all collected using a raster scan method. In confocal Raman microscopy, a pinhole is added in front of the detector which blocks all light from outside the center of the focal plane of the laser as shown in Figure 1.12. As shown in the schematic, rays from the focal plane (shown in green) pass through the pinhole and are collected by the detector while photons that are above (blue) or below (red) the focal plane are blocked [72].

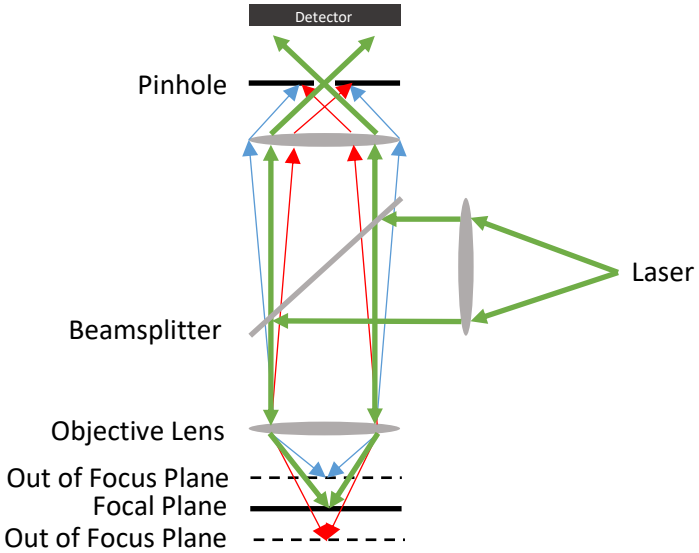

Figure 1.12. Schematic of a confocal collection system. Rays from the focal plane (green) are allowed to pass through the collection pinhole, however out of plane rays (blue and red) are blocked.

This technique improves both the axial and lateral resolution of the system and allows for depth profiling of a sample. This is done by reducing the point spread function (PSF) of the microscope system use a pinhole to block the off-axis light from entering the detector. In Section 1.4.1 it was explained that the resolution for a traditional microscope

(Equation 1.2) was related to the first minimum in an Airy disk. In confocal microscopy, the addition of the pinhole results in the creation of an additional Airy disk PSF. Since the Airy disk collected by the objective is projected onto pinhole, the overall PSF for the system is the product of the two PSFs [73]. This means that the best resolution achievable with confocal microscopy (to achieve the same separation defined by the Rayleigh criterion) results in an improvement by a factor up to $\sqrt{2}$ defined by [72, 73]:

$$\delta_{confocal} = 0.88\frac{f\lambda}{D} = 0.44\frac{\lambda}{\mathrm{NA}} \tag{1.5}$$

1.5.4 Raman Spectroscopy of Bacterial Spores

Most of the Raman analysis of *Bacillus* spores has been performed on the avirulent *B. anthracis* surrogates *B. cereus*, *B. subtilis*, *B. atrophaeus*, and/or *B. megaterium* although some measurements have been presented for the virulent *B. anthracis* Ames strain using normal Raman [36] and SERS [40, 74].

Earlier work collected Raman spectra from bulk samples measuring many spores at a time and collecting an average return signal. Woodruff, *et al*. published the first Raman spectra of a *Bacillus* spore in 1974 where spectra were collected from *B. megaterium* spores that had been collected onto a filter and measured on a rotating disc [75]. Improvements in Raman microscopy allowed for measurements to later be collected from individual spores [76, 77]. SERS and Tip-Enhanced Raman (TERS) have been used to improve the return signal strength from bacterial spores using gold [39, 78] and silver [40, 41] nanoparticles. Raman chemical imaging has been demonstrated to discriminate spores in a complex FOV containing multiple spores and/or background material [36-38].

Optical trapping is a technique where dielectric particles are captured at the focal point of a tightly focused laser. This occurs when the laser's scattering force balances the gradient force which causes the particle to be held in place. Optical trapping has been combined with Raman spectroscopy to trap and interrogate spores [42-44, 54, 55, 79, 80]. Since these measurements are taken in aqueous solutions, Raman optical trapping measurements can be used to monitor the changes in a spore over time. Spores have been monitored through germination [54, 55, 80] and inactivation [42-44] using this method.

CHAPTER 2

BRIGHT-FIELD IMAGING

2.1 Introduction

Bright-field imaging offers an attractive option for spore analysis because sample spores can be easily deposited onto microscope slides in large numbers (~millions) and the collection of images can be done quickly. This combination allows for rapid analysis of spores. Figure 2.1 shows an example bright-field image containing an entire 4 μL droplet on an aluminum microscope slide covering 3.7 x 3.7 mm. The image is stitched together from 196 separate images taken using a 20× objective to create a 14x14 montage image. Image collection took approximately 100 s. A comparable image covering the same region at 100× magnification could be completed in approximately 40 min.

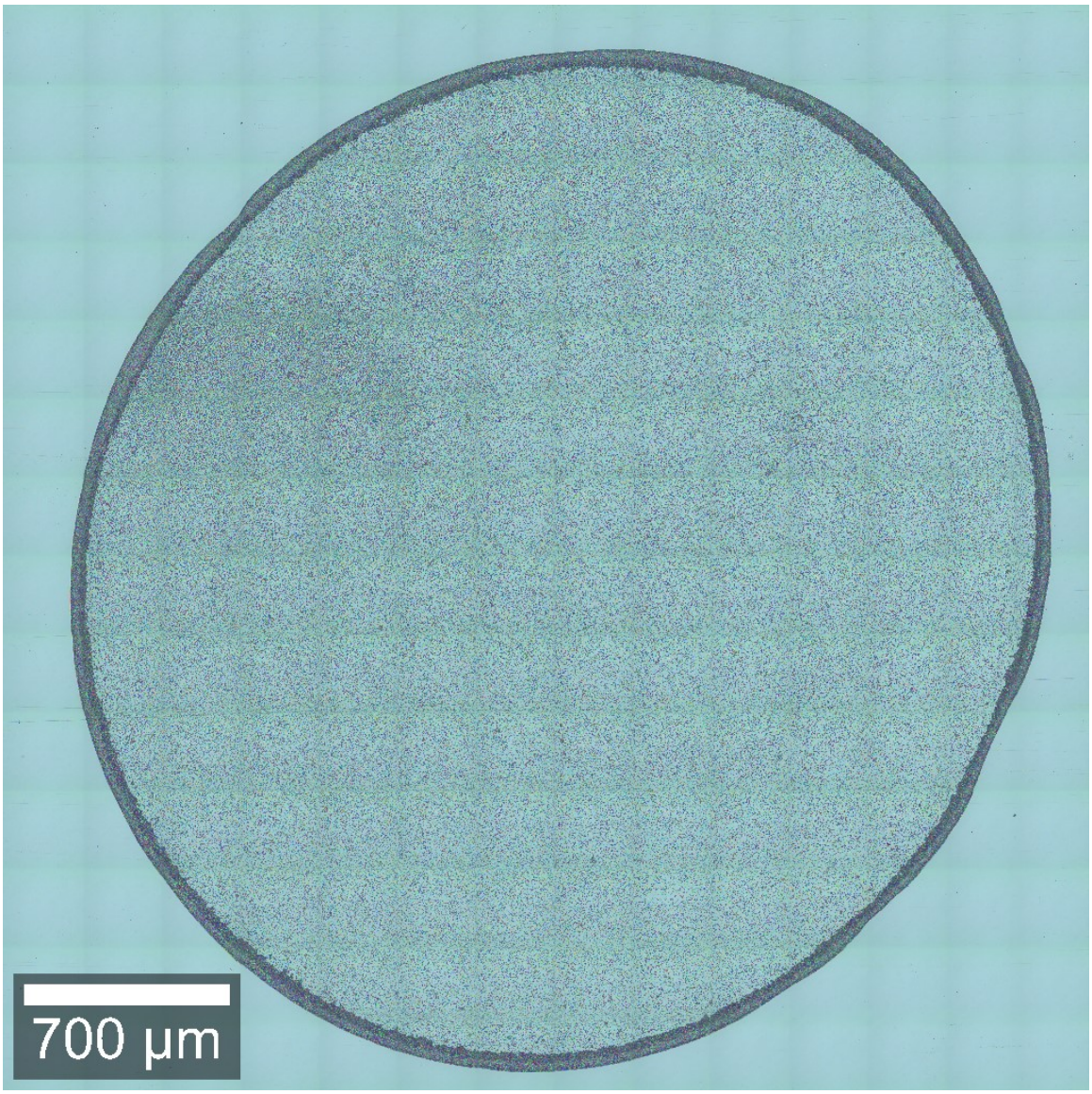

Figure 2.1. Stitched bright-field image covering entire 4 µL sample droplet.

Segmentation is an image analysis process where a group of pixels are combined to form regions based on a predefined criteria. For our application, we wish to rapidly and automatically obtain cytometric measurements that, in part, include shape and size parameters of spores from bright field images. This requires a robust and accurate segmentation method to locate and demarcate the individual spores. Specific software approaches to aid in the task of segmenting biological samples have been previously

explored [81, 82]. A variety of segmentation techniques have been applied on large cellular materials including white blood cells, which are in 12 to 17 μm size range [83-85], hematopoietic stem cells (~20-30 μm) [86], cancer cells [87], bone marrow, blood, and cervical nuclei (~6 μm) [88, 89], living Spodoptera frugiperda cells (~9-12 μm) [90], and fungal and bacterial spores (~2-60 μm depending on species) [91-97]. These applications typically rely on a relatively small set of segmentation techniques: thresholding, edge/feature detection, morphological filtering, region growing, and deformable model fitting [98, 99]. More advanced segmentation techniques such as neural networks require large amounts of training data to improve upon the accuracy [83] which can be achieved with traditional techniques.

In this effort, a combination of these traditional segmentation techniques were used to quickly and autonomously segment bright-field images of *Bacillus anthracis* Sterne spores. These spores are an attenuated strain of the bacterium that causes anthrax which is commonly used as a surrogate material for testing the performance of protection and detection equipment against the virulent corollary. *Bacillus anthracis* Sterne spores are small (~1 μm in diameter) compared to the cells described in the previous paragraph, which can make it difficult to detect using bright-field imaging since it is close to the diffraction limit of optical microscopy. Using the microscope described later with a 100× objective, the image of a single spore is typically 11-16 pixels in length. Additionally, the spore deposition on a substrate is random, and the spores may be distributed individually or in clusters of varying sizes, which further complicates the segmentation process. The segmentation procedure developed in this thesis and results are detailed below.

2.1.1 Bright-Field Imaging Instrumentation

All bright-field images were collected using a Witec (Ulm, Germany) Alpha 300R confocal microscope system shown in Figure 2.2 using a Zeiss EC Epiplan-Neofluar DIC 100x objective with a NA of 0.9. The images were captured using an Imaging Source (Charlotte, NC) 752×480 CMOS camera installed in the microscope system.

Figure 2.2. Witec Alpha 300R microscope

2.2 Watershed Segmentation

2.2.1 Algorithm Procedure

To rapidly and autonomously analyze large amounts of bright-field images, this work employed an algorithm based on the traditional watershed technique [100] along with optimized pre-processing sequence for this application. For this work, All calculations were performed using Matlab 2017b (MathWorks, Natick, MA) with the Image Processing toolbox. A flow chart of the processing steps are shown in Figure 2.3.

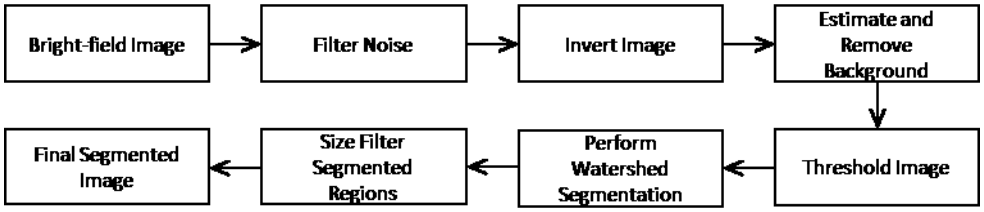

Figure 2.3. Flow chart showing image segmentation steps

The details of these steps are demonstrated on a bright-field image shown in Figure 2.4a. Prior to the application of the watershed algorithm, a four step pre-processing routine was performed. First, a spatial averaging filter was used to reduce noise (Figure 2.4b). The filter size could be changed, but for this work it was set to 3×3 pixels. Secondly, since the spore boundaries have a lower intensity value than the background and the watershed transform works by finding the high intensity gradients, the grayscale image was inverted (Figure 2.4c) to properly identify the spore edges. Thirdly, the image was then morphologically opened using a disk shaped structuring element (typically with an 8 pixel radius) to create a background image (Figure 2.4d). This background image was then subtracted from the inverted image to flat-field the image and account for non-uniform illumination (Figure 2.4e). Finally, an intensity threshold was applied to the image to remove any remaining background pixels which could result in over-segmentation of the image (Figure 2.4f). This threshold was selected to a value above the residual from known background regions. For all the work presented in this chapter, the threshold was set to 20 which resulted in all pixels with an intensity value less than 20 being set to zero. After these pre-processing steps were completed, the watershed transform was applied to segment the image (Figure 2.4g). The size of each segmented region was then calculated.

Regions that were too small or too large in comparison to a typical spore were removed from the final results. For these bright-field images, the desired region size range was typically greater than 60 pixels and less than 280 pixels which produces the final segmented image shown in Figure 2.4h. Using a Dell laptop computer with a dual core Intel i7 processor operating at 3.00 GHz with 8 GB of RAM and running 64-bit Windows 10, the entire analysis was completed in near-realtime, taking approximately 100 ms.

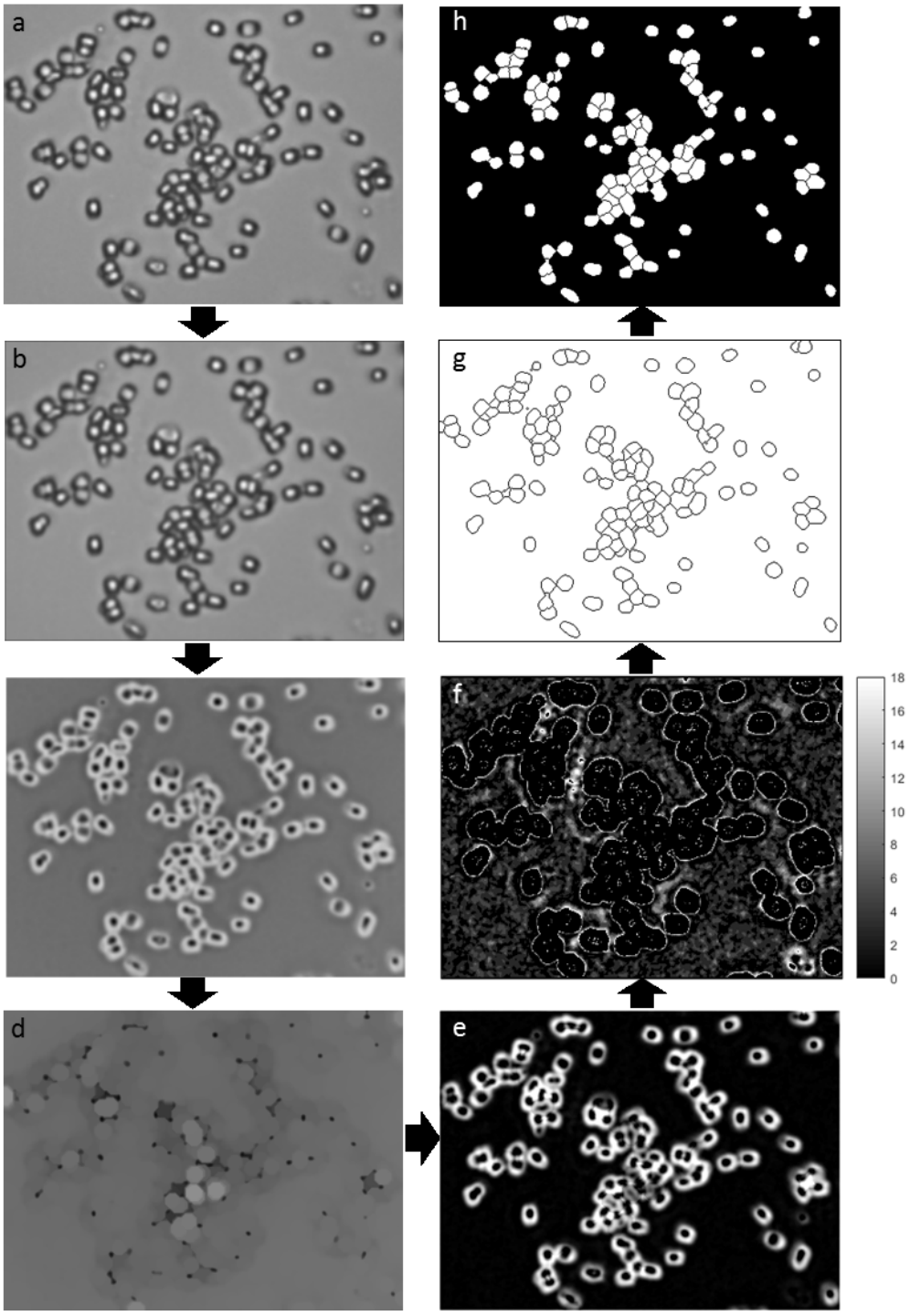

Figure 2.4. Images showing the how the original bright-field image (a) was analyzed to produce the final segmented output image (h). The bright-field image was first spatially averaged (b) and then inverted (c). A morphological image opening was performed on this inverted image to produce (d) which provided an estimate for the background illumination. Image (d) was then subtracted from image (c) to get the background corrected image (e). The image was then thresholded to remove any remaining background artifacts that could lead to over-segmentation. The light pixels in image (f) were set to zero prior to watershed segmentation (g). A size filter is then applied to the segmented image to remove regions that are too large (such as the background) or too small to represent a spore (h).

2.2.2 Segmentation Performance

To determine the effectiveness and robustness of the segmentation method, a scoring criteria was developed to quantify the algorithm performance as a test image was altered to provide different challenges to the process. The original test image was visually examined by multiple analysts to determine the number of spore-like objects present. Each segmented region was then compared to these results with each region receiving a score using the following criteria:

- True Positive for a single spore (TP) – Correct detection of a single spore-like object in a region
- True Positive for a spore cluster (TP*) – Correct detection of multiple spores-like object in a single region (expressed as the total number of true spores identified in that region)
- False Positive (FP) – Identified region does not correspond to a analyst counted spore-like object
- False Negative (FN) – Spore-like object identified in analyst count not segmented by algorithm

The test image, shown in Figure 2.4a, had 112 analyst counted spore-like objects. Segmenting the image (Figure 2.4h) resulted in 98 TP and 10 TP* which corresponds to 108 of the 112 total spore-like objects. The remaining 4 spore-like objects were scored as FN and the algorithm had an additional 13 FP. To challenge the algorithm, the test image

was varied using three different methods to determine the algorithm's robustness against each type of variation. Two of the methods altered the image's contrast-to-noise ratio (CNR) and the third scaled down the image resolution.

The CNR was determined with the histogram of the image which produced a bimodal response with a local maximum centered on the intensity of the spore edges and an absolute maximum centered on the intensity of the background as shown in Figure 2.5. The contrast value was defined as the difference between these two maxima and the noise was defined as the full width at half maximum value around the intensity of the background region. Using this criteria, the CNR of the original image is 6.7.

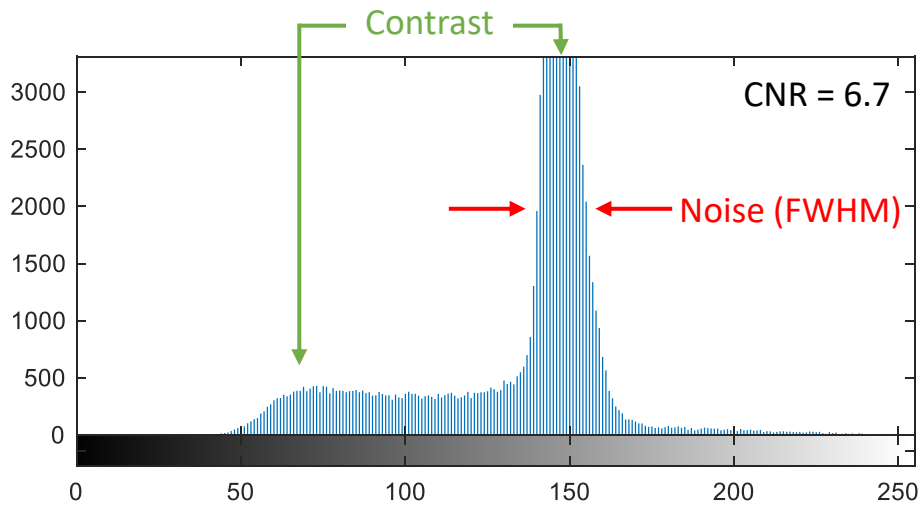

Figure 2.5. Grayscale histogram of test image showing bimodal distribution used for CNR calculation.

Two techniques were used to lower the CNR; the first lowered the contrast and the second increased the noise. In the first technique, which simulates samples with less than ideal illumination, an inflection intensity value between the background and spore edge

values, I, was identified. The image intensity values, x, were mapped to new values x^' using equation 1.

$$x' = \begin{cases} x + M & \text{for } x < I - M \\ I & \text{for } I - M \leq x \leq I + M \\ x - M & \text{for } x > I + M \end{cases} \quad (1)$$

A constant, M, was added to values below the inflection intensity and subtracted from values above the inflection intensity. By changing the value of M from 0 to 35 in increments of 5, the CNR was varied from the starting value of 6.7 down to 0.8. Figure 2.6a shows an example image created with this technique on the left. For this image, M was set to 35 which created an image with a CNR of 0.8. The segmentation results are shown in Figure 2.6b which correctly identified 90 single spore-like objects (TP) and 8 spore-like objects that were grouped into regions of multiple spores (TP*). This means that 14 spore-like objects were missed (FN) and added to that, there were 17 FPs. Figure 2.6c shows the performance over different CNR values with a minimal change of 2 overall positive detections (TP+TP*) for and 4 additional false results (FP+FN) for CNR values of less than 3.

The second method to vary the CNR value was to increase the image noise. To do this, a uniformly distributed set of random intensity values within the range of ± 50 was added to each pixel in the image. This method was also used to vary the image CNR from 6.7 down to 0.8 with results shown in the second row of Figure 2.6. An example image with random intensity value of ± 20 added to the image and a CNR of 2.0 is shown Figure 2.6d with segmented regions shown in Figure 2.6e. The plot in Figure 2.6f shows consistent performance of TP and TP* for all values of CNR, with a reduction of just 6

overall spore-like objects. The FP and FN values are consistent to a CNR down to about 2.5 increasing from 15 to 25 over this range before the noise leads to a large increase in over-segmentation. This over-segmentation continues to increase before spiking at a CNR of 1.2 at which point the region size filter begins removing the small over-segmented regions. Another factor to consider is the spatial averaging filter size. All of the analysis described in this work was performed with a 3×3 spatial averaging filter. A trade-off analysis was also performed by increasing the spatial averaging filter to 5×5. Increasing the size of the spatial averaging filter to 5x5 had similar total true positive (TP and TP*) detection results and was able to reduce the amount of over-segmentation in the case of higher noise level images. However, the 5×5 spatial averaging filter size reduced single spore detections (lower TP and higher TP*) for the low noise images.

The remaining challenge for the algorithm was to determine the effect that image resolution had on performance. The image was scaled down to 10% of the original 303x403 pixel size in 10% steps. To maintain the original aspect ratio, the 'imresize' function of Matlab was used with the default interpolation. The preprocessing steps involving size, specifically, the spatial averaging filter, the morphological structuring disk, and region size filtering, described in Section 3, were all scaled accordingly. The spatial filter was rounded using a floor function and the structuring element was rounded to the nearest integer. Figure 2.6g shows an example with the reduction to 30% of the original (91x121 pixels) with the segmented regions shown in Figure 2.6h. The plot in Figure 2.6i shows consistent results to approximately 50% size reduction in terms of TP (down 2 from original), TP* (no change from original), and FP+FN (up 3 from original). Starting around 40% size reduction, there is a drop in TP although the overall detections (TP+TP*) remain

consistent. This is because the algorithm starts to output more regions that encompass multiple spore-like objects at the expense of single spore region. At 10% the resolution has degraded to a point where only 12 spore-like objects were identified and 100 were missed by the algorithm.

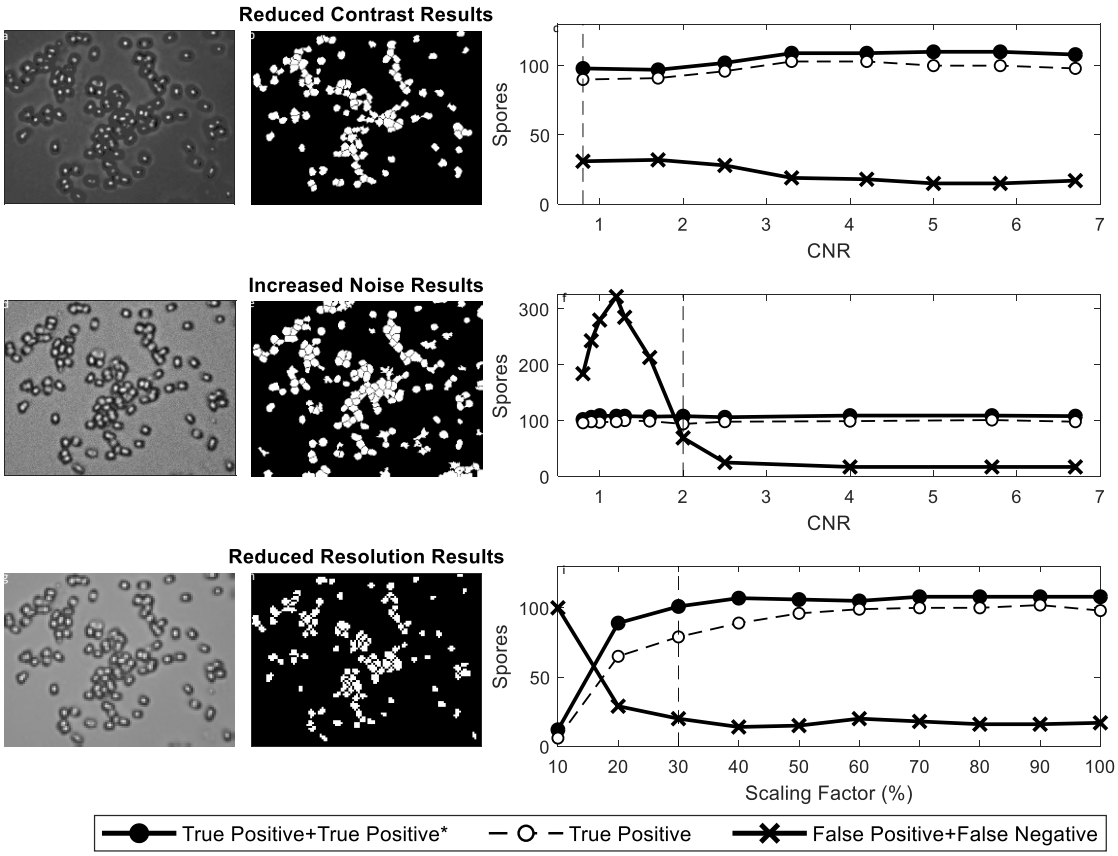

Figure 2.6. Segmentation results with varying parameters. An example image for each of the three techniques used to challenge the algorithm in the left column and the segmentation results in the center. A summary plot showing how changing each factor effects the results is shown in the right. The dashed line with open circles represents the true single spore detections (true positive). The solid line with closed circles adds the true multi-spore detections to the true positive values (true positive*). The solid line with X markers is a combination of the false negative and false positive results. The vertical dashed line shows which data point is shown in the left two columns.

The algorithm was applied to additional test images shown in Figure 2.7. These three images were collected from the same slide preparation that was used for Figure 2.7a, but represent examples showing a range of spore density and sparseness. Figure 2.7a is a 164x202 pixel image with analysts counting 52 spore-like objects, Figure 2.7b is a 234x326 pixel image with analysts counting 185 spore-like objects, and Figure 2.7c is a 248x310 pixel image with analysts counting 109 spore-like objects. Table 2.1 lists the algorithm results for these three images as well as the results from Figure 2.4a. Overall, of the 458 total spores in all the four images, 418 (91.2%) single spore-like objects were identified in single segmented regions (TP). An additional 28 spore-like objects were correctly identified in regions containing multiple spores (TP*). This leads to an overall segmentation of 97.4% of all the spore-like objects in the image. The method missed 12 spore-like objects leading to a FN rate of 2.6% and an over-segmentation of 49 regions (10.7%). Examining the images individually, Figure 2.7a and Figure 2.7c have less spore clustering than those in Figure 2.4a and Figure 2.7b, resulting in better segmentation. In Figure 2.7a, the smallest of all the test images, all 52 spore-like objects were identified with only 1 False Positive. Similarly in Figure 2.7c, 107 of the 109 spore-like objects were correctly identified (98.1%) with 6 False Positives. In Figure 2.7b, the most densely clustered test image, the algorithm correctly located 179 of 185 spore-like objects (96.7%) with 29 False Positives. It was noticed that in these higher density images that most over-segmentation occurred in the interstitial space between the spores which lead to the elevated FP rates. However, over all test images the positive detection rates remained high (>96%) regardless of spore density.

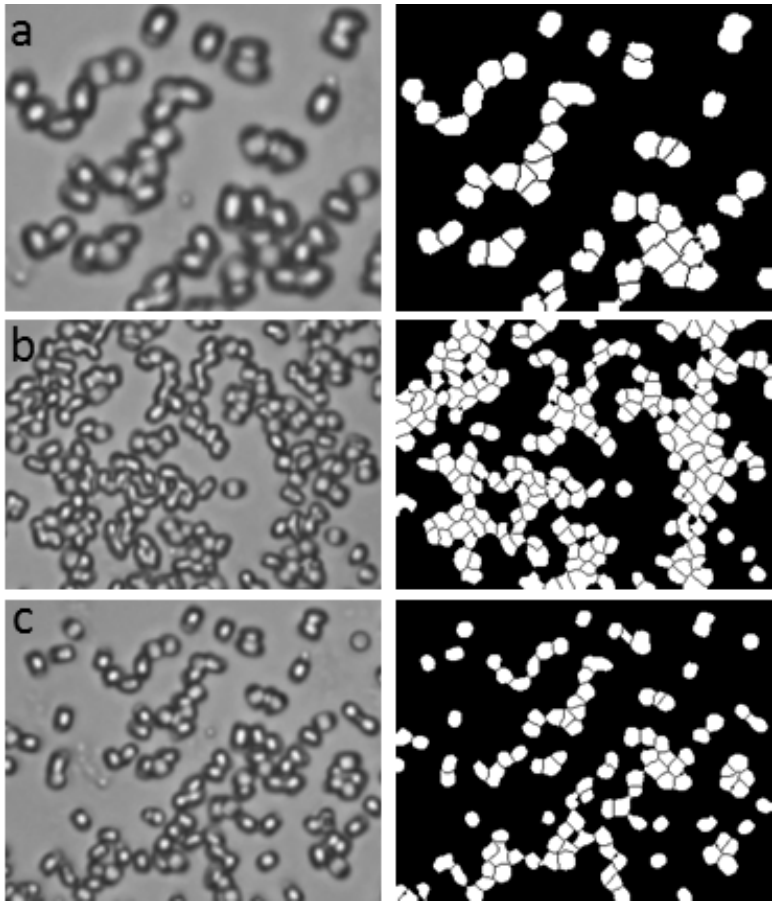

Figure 2.7. Segmentation results for additional bright-field images.

Table 2.1. Comparison of the manual spore count to algorithm results

	Fig. 2.4a	Fig. 2.7a	Fig. 2.7b	Fig. 2.7c	Total
Manual Count	112	52	185	109	458
True Positive	98	48	171	101	418
True Positive*	10	4	8	6	28
Total True Positive (TP+TP*)	108 (96.4%)	52 (100%)	179 (96.8%)	107 (98.2%)	446 (97.4%)
False Positive	13 (11.6%)	1 (1.9%)	29 (15.7%)	6 (5.5%)	49 (10.7%)
False Negative	4 (3.6%)	0 (0%)	6 (3.2%)	2 (1.8%)	12 (2.6%)

2.3 Viability Determination using Bright-Field Imaging

After properly segmenting the images, it is possible to extract cytometric information about the size and shape characteristics of the spores. This was performed using the 'regionprops' function in Matlab. For each segmented region we determined the area, eccentricity (the ratio of the elliptical foci of a region to its major axis length), perimeter, and major and minor axis lengths. This method was used on various bright-field images with larger fields of view to analyze a total of 4048 viable spores. It was determined that the spore samples had a major axis length of 1.43 ± 0.16 μm (standard deviation) and a minor axis length of 1.15 ± 0.16 μm. When compared to values reported by Carerra, et al. [101], the major axis length is in very close agreement with their length of 1.49 ± 0.17 μm. The measured minor axis length is slightly larger than the reported value of 0.85 ± 0.08 μm. The reported values by Carerra are based on a manual count of 100 spores from a transmission electron microscopy image and these images show a visually more elliptical shape than the spores reported in this effort likely due to much higher resolution achieved by TEM and/or the differences in the strains of spores. *B. anthracis* Sterne spores. These spores have a spheroid shape which allows their volume to be determined using the major and minor axis lengths and the equation $V = \pi LW\ 2/6$ for the major axis length, L, and minor axis length, W. Calculating the volume allows for comparison to spore measurements taken using Coulter counters which have a much higher throughput than image analysis techniques [102]. *B. anthracis* delta-Sterne is an attenuated version of *B. anthracis* Sterne with similar size characteristics [101]. Buhr, et al [102] reports a spherical diameter for *B. anthracis* delta-Sterne spores of 1.14 ± 0.18 μm based on over 800,000 spores using Coulter analysis. This value is in good agreement with the 1.23 ± 0.14 μm,

which we determined based on our measured major and minor axes lengths using optical microscopy and are shown in Figure 2.8.

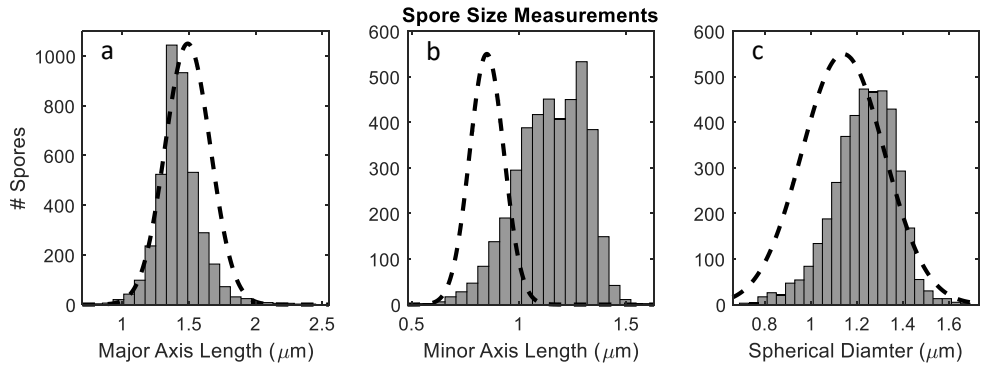

Figure 2.8. Size measurements determined using segmented images showing the spore major (a) and minor (b) axis lengths compared to results reported by Carerra [34] (dashed lines left and middle) based on a small number of analyst counted spores. Using these values to determine a spore volume ($V=\pi LW2/6$), the spherical diameter can be calculated (c) which shows good agreement to the values reported by Buhr [35] based on a large sample size of Coulter counted spores and is represented by the dashed line on right.

A similar series of images with larger fields of view were analyzed to determine the size and shape characteristics for 3627 gamma irradiated spores. Comparing these non-viable spores to the viable spores showed a similar length along the major axis, 1.43 ± 0.16 μm for the viable compared to 1.42 ± 0.26 μm for the gamma irradiated ones, however the minor axis length was smaller for the gamma irradiated samples with a length of 0.99 ± 0.13 μm (non-viable) compared to 1.15 ± 0.16 μm (viable). The ratio of the major axis to the minor axis (hereafter called length ratio) for individual spores has a median of 1.22. The length ratio cannot be less than one, which means that 50% of the viable spores have a ratio between 1 and 1.22. The length ratio for the gamma irradiated spores has a median value of 1.42 and a standard deviation of 0.24. These differences are also noticeable in the area, where the viable spores measure 1.25 ± 0.26 μm^2 and the non-viable spores measure 1.08 ± 0.31 μm^2. Figure 2.9 shows the comparison of these three parameters with the

viable spores shown in light gray and the gamma irradiated spores shown in dark gray. Since these distributions do not necessarily follow a normal distribution, a one-sided Mann-Whitney U-test was performed ($\alpha = 0.01$) to test whether the measurements are from independent populations. The test rejected the null hypothesis for all three ($p = 0$) and returned z-statistic values of 43.8, 37.4, and 30.9 for the minimum axis length, length ratio, and spore area, respectively. It is evident that there is overlap between the distribution of viable and non-viable spores which prohibits perfect classification. Figure 2.10 shows the receiver operating characteristics (ROC) curve based on the minimum axis length (solid line), the ratio of the maximum to minimum axis lengths (dashed line), and the area (dot-dashed line) to quantify the tradeoffs between the ability to correctly identify viable spores and the misclassification of gamma irradiated spores. The area under the curve (AUC) for each variable described above shows that the minimum axis length provides the best criterion to discriminate using univariate thresholding. The result maximizing the sum of the probability of true detection and one minus the probability of false detection (alternatively this can be viewed as maximizing the distance from random chance, shown by the dotted line) corresponds to a true identification rate of 67% with a misclassification rate of 18%, and is marked in Figure 2.10. If used as a screening method, the threshold could be adjusted to allow more or less false identifications depending on the speed required for any follow-on sampling. The discrimination performance should be tested with more advanced classification methods such as support vector machines, but this was not explored in this work.

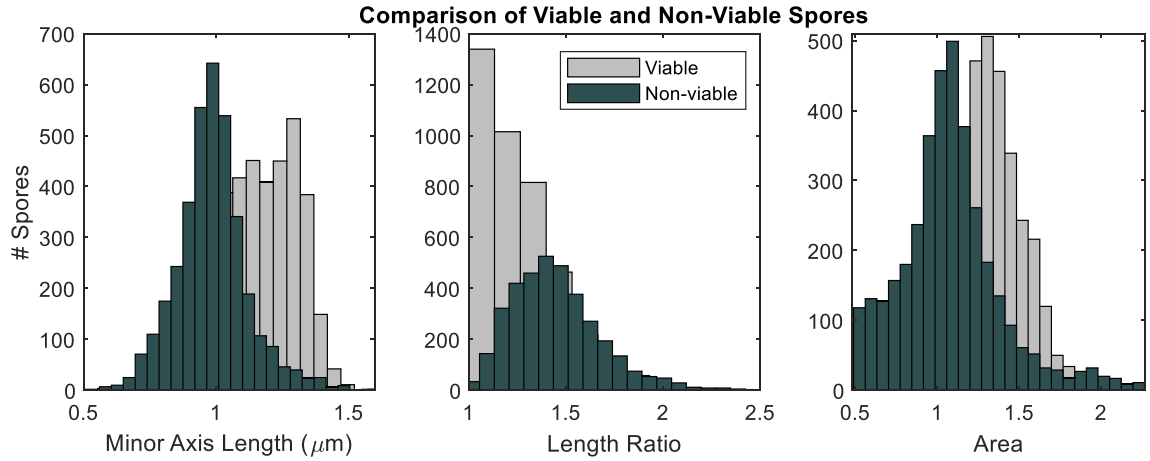

Figure 2.9. Comparison of the size characteristics for the viable (light gray) to non-viable (dark gray) spores showing the difference in minor axis length (left), the ratio of major axis to minor axis (center), and the spore area (right).

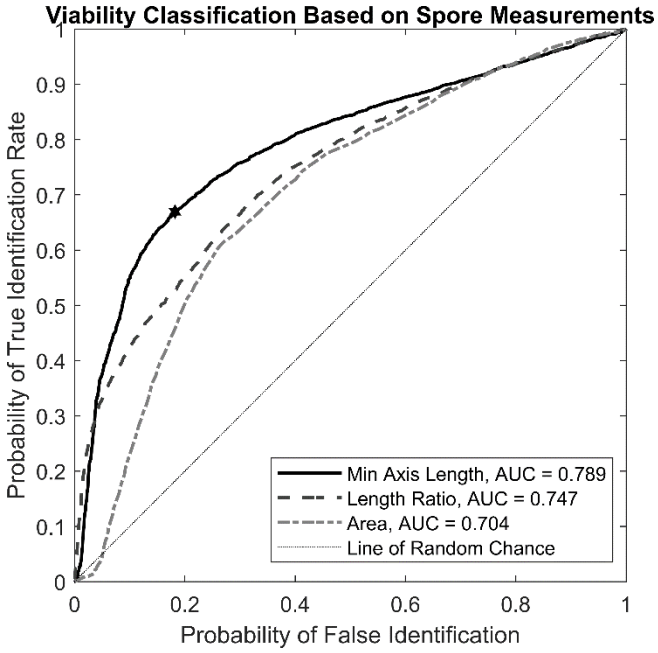

Figure 2.10. Receiver operating characteristics showing ability to classify viable spores based on the minimum axis length (solid), the ratio of minor axis length to major axis length (dashed), and area (dot-dashed). The dashed line on the diagonal shows the result for a random classifier and is for visualization purposes only. The point maximizing the distance from random is marked with a star and corresponds to a 67% true identification rate with an 18% misclassification rate.

CHAPTER 3

RAMAN SPECTRAL ANALYSIS OF BACTERIAL SPORES

3.1 Introduction

Raman microscopy provides a potential method to overcome the misclassification rate between viable and gamma-irradiated spores demonstrated using bright-field imaging alone in Chapter 2. As discussed in Section 1.5.3, Raman spectroscopy has previously shown the ability to differentiate viable from non-viable spores that were inactivated using wet-heat [42, 43], cold atmospheric plasma [44], and chemical (formalin) [40] methods. In this Chapter we first look at spectral differences in viable and gamma irradiated *B. anthracis* Sterne spores. Next, we discuss spore damage that could result from interrogation by the Raman laser and its impact on measured Raman signal. We then detail

a registration technique to align the high resolution bright-field image with the low resolution Raman image to extract single spore spectra from RHSCs. We then look at Raman spectra from different *Bacillus* strains and component biomarkers. Finally, we compare spectral changes for all these Bacillus strains between viable and inactivated spores using both gamma irradiation and autoclaving methods.

3.1.1 Raman Instrumentation

Raman spectra were collected using the same Witec Alpha 300R confocal microscope system used for the bright-field imaging. The sample was excited using the same 100× microscope objective with a 532 nm excitation laser. The light was collected by an optical fiber and dispersed in a Witec UHTS300S_VIS spectrometer. Both the laser and spectrometer are shown in Figure 3.1. The spectrometer used a 600 line/mm grating blazed at 500 nm which produced spectra with a 4 cm^{-1} resolution.

Figure 3.1. Image of Witec 532 nm excitation laser and UHTS300S_VIS spectrometer

3.2 Raman Analysis of *Bacillus* Biomarkers

In order to attribute specific spectral features within spore spectra, Raman spectra was collected from *Bacillus* biomarkers. As discussed in Section 1.3.1, *Bacillus* endospores are primarily made up of DNA, SASPs and other proteins, CaDP, peptidoglycan. Additional spectra were also collected for Lipteichoic acid and polyhydroxybutyric acid (PHBA) which are not typically found in spores, but are found in vegetative *Bacillus* cells [24, 103, 104]. These were included as biomarkers because remnants of these compounds could be present in the samples after sporulation.

To collect these samples, aluminum coated microscopy slides were prepared by depositing dry samples of various spore biomarkers to include CaDP, lipoteichoic acid and peptidoglycan from *Bacillus subtilis*, PHBA, and DNA from *E. coli*. Raman spectroscopy is not very specific in discriminating large proteins, thus ovalbumin from chicken egg white was added to the list of biomarkers as a surrogate for large proteins. The CaDP was synthesized using the method described by Strahs [105] and all other biomarkers were purchased commercially. Spectra for these biomarkers can be seen in Figure 3.2.

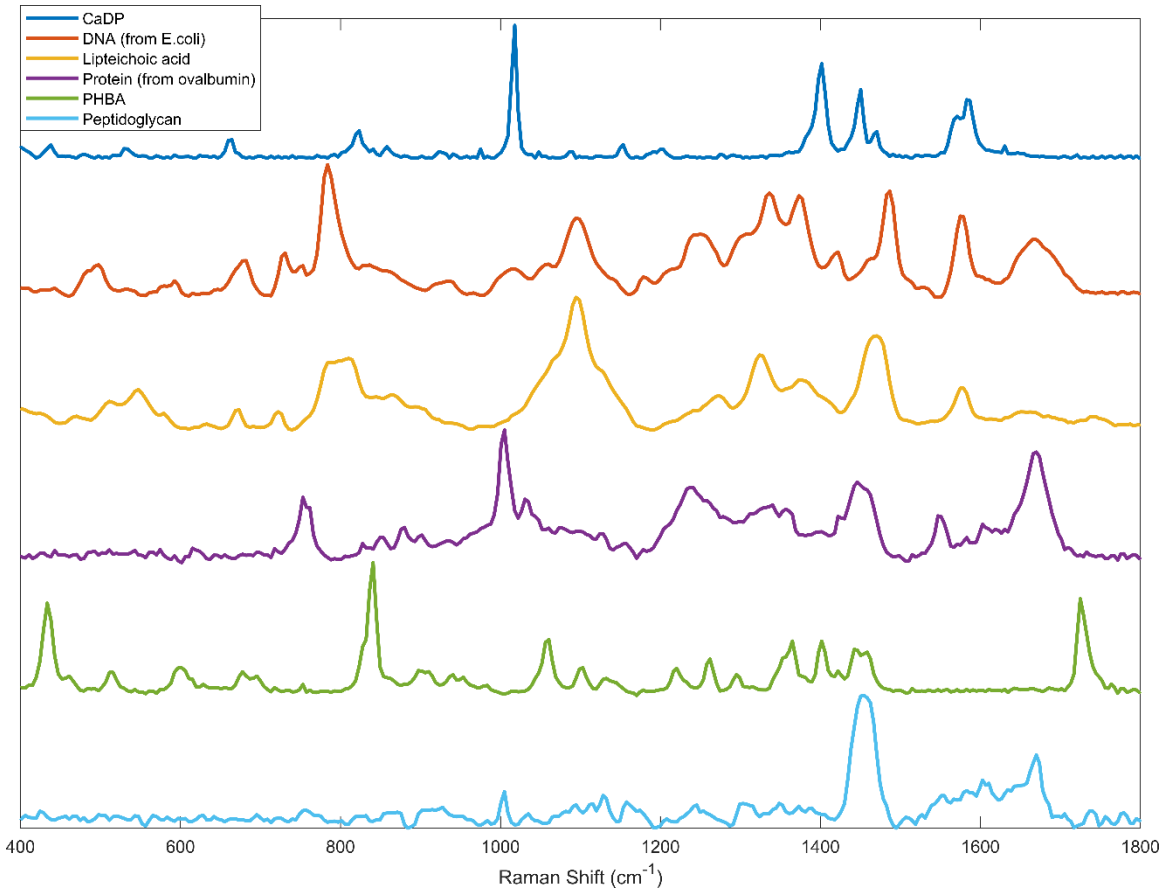

Figure 3.2. Raman spectra of several *Bacillus* biomarkers.

3.3 Average Raman Spectra from Viable and Gamma Irradiated *B. anthracis* delta Sterne Spores

To determine whether Raman spectroscopy is capable of differentiating viable and gamma irradiated spores, we needed to obtain representative Raman spectra for both classes. Two separate slides were prepared: the first was populated with only viable spores and the second with gamma irradiated spores. Multiple fields of view (FOVs) from the two microscopy slides were interrogated with Raman chemical imaging microscopy. The Raman microscope was used in "continuous mode" where each spectra was acquired with a 0.5 μm step size over samples of all viable and gamma irradiated spores to generate Raman hyperspectral cubes. Preprocessing of all RHSCs was performed using Witec Project 5.2 analysis software by removal of "cosmic rays" using a filter size of 2 and dynamic factor of 5 (description of these terms are proprietary of Witec). Additionally a baseline correction was performed using a rolling circle filter with a size of 100 spectral bins. Average spectra were created of each population by extracting spectra from these hyperspectral cubes. Both types of spores have strong Raman peaks associated with the C-H stretching vibrations around 2938 cm^{-1}, which was used as a trigger to include that spectrum in the generation of representative average spectra for each of the two classes. A total of 2200 spectra were extracted from 325 viable spores and 1100 spectra were used from 150 deactivated spores. The average of the extracted Raman spectra from viable and gamma radiation deactivated *B. anthracis* spores constituted the representative spectra for the two classes. Figure 3.3 shows the average spectra of the viable and gamma irradiated spores. The intensities of the spectra have been normalized to that of the C-H stretch (not

shown), and offset for clarity. The average Raman spectrum from the gamma radiation deactivated spores was subtracted from that of viable spores. The difference spectrum is shown with blue line in the Figure 3.3. Significant spectral differences were noticed at 664, 823, 1018, 1402, 1450, and 1575 cm^{-1}, which were linked to CaDP, a bio-molecule found in Gram positive spores that is reported to stabilize the DNA inside the spore [106]. CaDP was synthesized using the method described by Strahs [105], with the spectrum shown as the black line in Figure 3.3 for comparison.

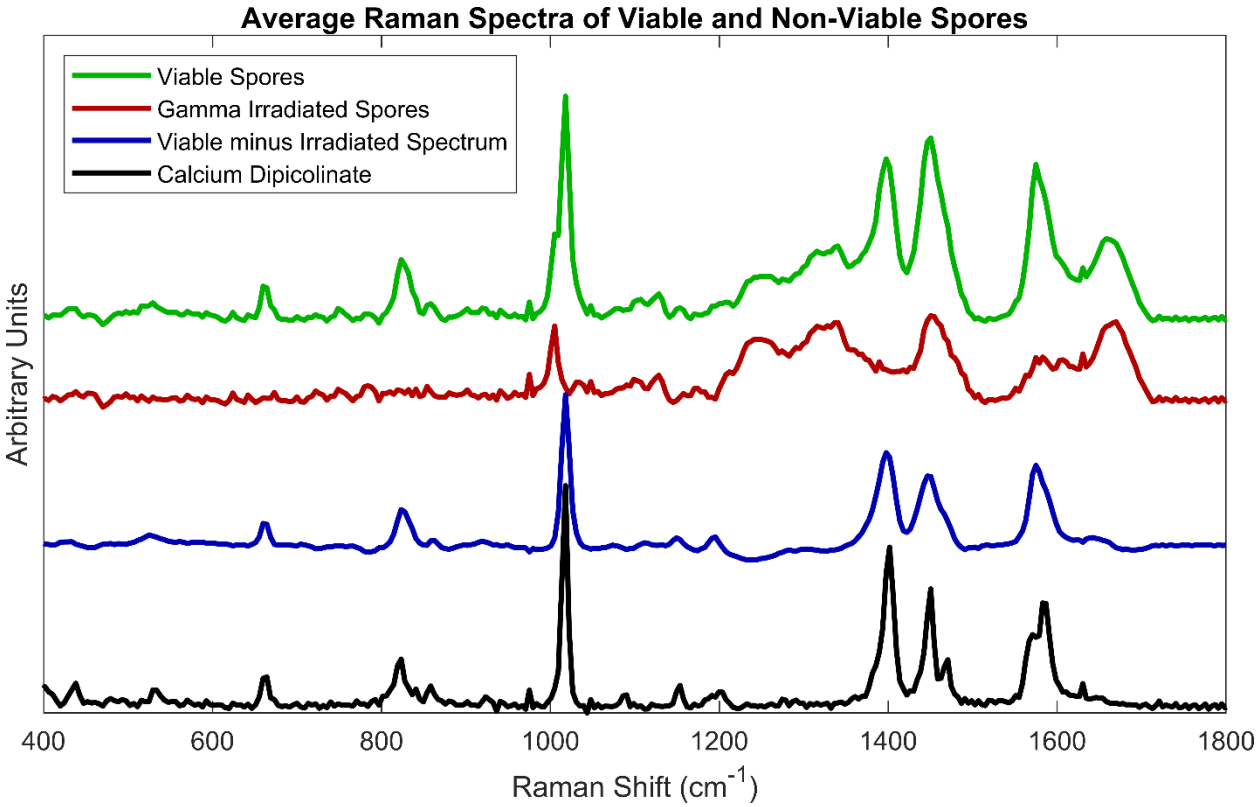

Figure 3.3. Average spectra collected from viable (green) and gamma irradiated *B. anthracis* Sterne spores (red). Using a least squares subtraction of the non-viable from the viable spectrum leaves the residual shown in blue which matches the CaDP shown in black. The spore spectra were normalized to the C-H peak intensity and 2938 cm^{-1}. Spectra have been offset for clarity.

3.3.1 Effect of Spore Edges on Raman Signatures

The spectra from Section 3.3 are averages taken over a large number of whole spores. It was observed when looking at individual spores that there are spectral variations depending on which portion of the spore the laser is centered at. To demonstrate this effect, a high density (oversampled) RHSC was generated of the three viable *B. anthracis* Sterne spores shown in Figure 3.4a.

A RHSC was generated over a 7×7 μm area comprised of 28×28 laser interrogations (0.25 μm steps between each measurements). From this it was observed that different regions of the spores had different ratios in some of their spectral components. These two components corresponded measurements centered in the core of the spore (shown in red in Figure 3.4b) and those taken at the edge (blue). The spectra for these two populations are shown in Figure 3.4c where the spectra have been normalized to the C-H stretch peak at 2938 cm^{-1} (not shown). The average viable spectrum from Section 3.2 is shown in green and offset for comparison. Overall, the same spectral peaks are present and the correlation coefficient for these two spectra from 600-1750 cm^{-1} is 0.975, however the intensity of the peaks at 1018, 1402, 1450, and 1575 cm^{-1} (denoted with *) are reduced. These spectral peaks are associated with CaDP which, as discussed in Section 1.3.1, is concentrated in the core of a spore. The intensity of the peaks located at 664, 823, and 1664 cm^{-1} are consistent for the two spectra. The change in the peak ratios from the core and edge has the potential to effect spectral library matching algorithms.

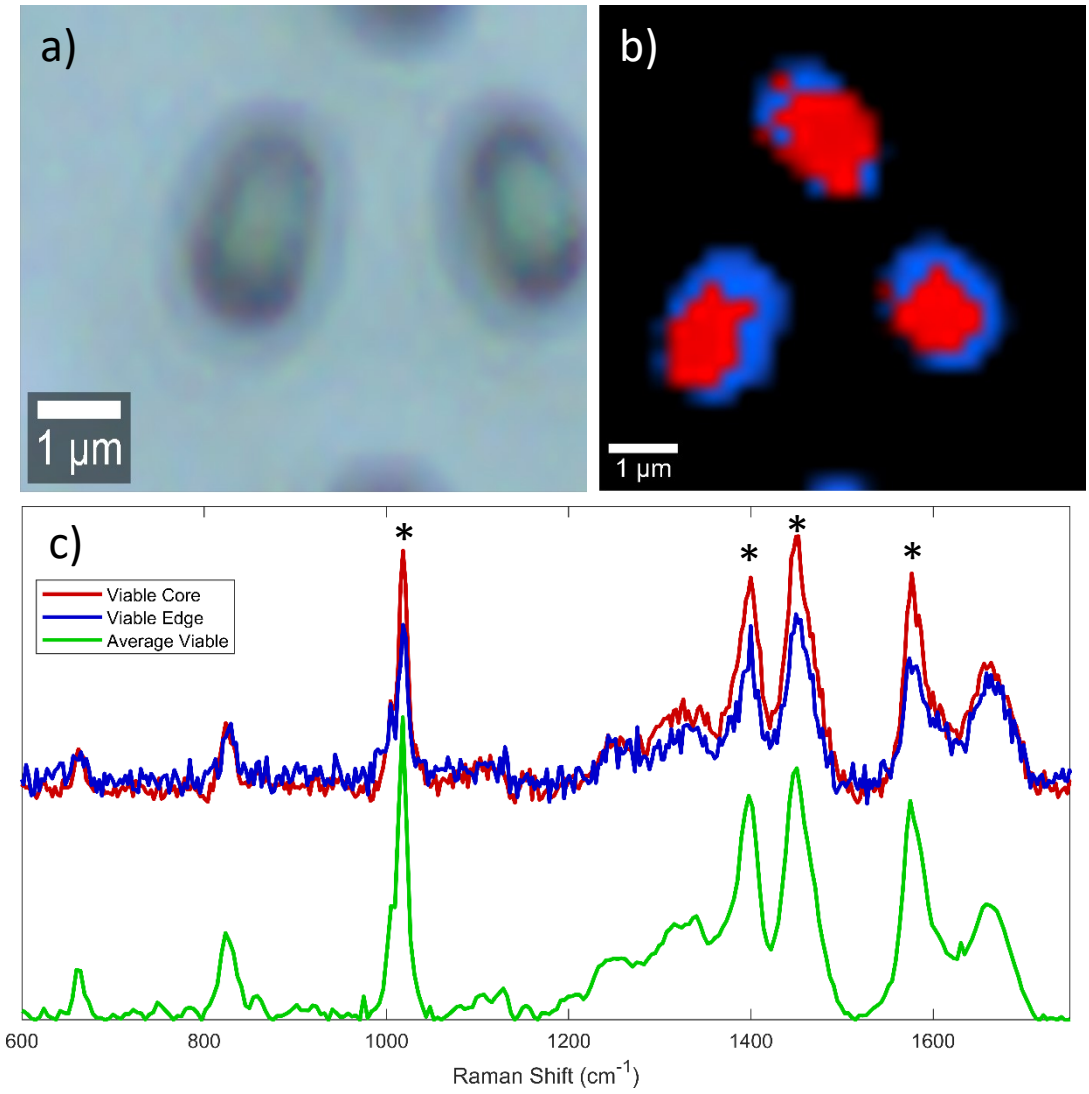

Figure 3.4. Three viable spores (a) were used to generate a high spatial resolution RHSC with 0.25 µm step size. b) shows the locations that correspond to two distinct spectral features appear in the core (red) and the edge (blue). These spectra are shown at the top of c). The average viable spectrum from Section 3.2 is shown in green for reference.

3.3.2 Laser Damage and Integration Time

The measured Raman signal strength can be controlled by two main instrument settings: laser power and integration time. To acquire a strong Raman signal one would ideally use the highest possible laser power (without damaging the sample) for the longest possible exposure time (to prevent detector saturation). The final application described in this thesis requires short detector integration times to allow for a high throughput. This section analyzes the trade space between these two factors to determine a laser intensity and integration time that yield an acceptable signal to noise ratio (SNR) in the shortest time while minimizing sample damage.

First, an estimate of the spore laser damage threshold was estimated. This was performed by interrogating a spore for 100 s using different laser intensities. A Raman spectrum was collected each second to monitor any changes within the spore. Spores were interrogated using 3 mW, 5 mW, 7 mW, 10 mW, and 20 mW laser intensities. A single spectrum from a viable spore collected using a 1 s integration time is shown on the left of Figure 3.5 for each of these laser intensities showing the increased Raman signal as the laser power rises. The SNR was calculated by taking the ratio of the CaDP peak at 1018 cm^{-1} to the standard deviation of the 1840-2700 cm^{-1} region of the spectra (which has no spectral features). The right side of Figure 3.5 shows the SNR calculated over 20 spectra for the 3 mW, 5 mW, and 7 mW with an average value of 5.4, 8.2, and 12.5, respectively. Laser damage (discussed further below) was observed in less than 20 s for the 10 mW and 20 mW measurements so only five and one data points are shown for these two powers, respectively. The average SNR for 10 mW spectra similar to the 7 mW measurement at

12.7. The SNR for the 20 mW spectrum was 16.3. Bright-field images, shown in Figure 3.6, were taken before and after laser exposure. These images show that visible damage occurs using a laser powers of 7 mW or higher over the 100 s time period.

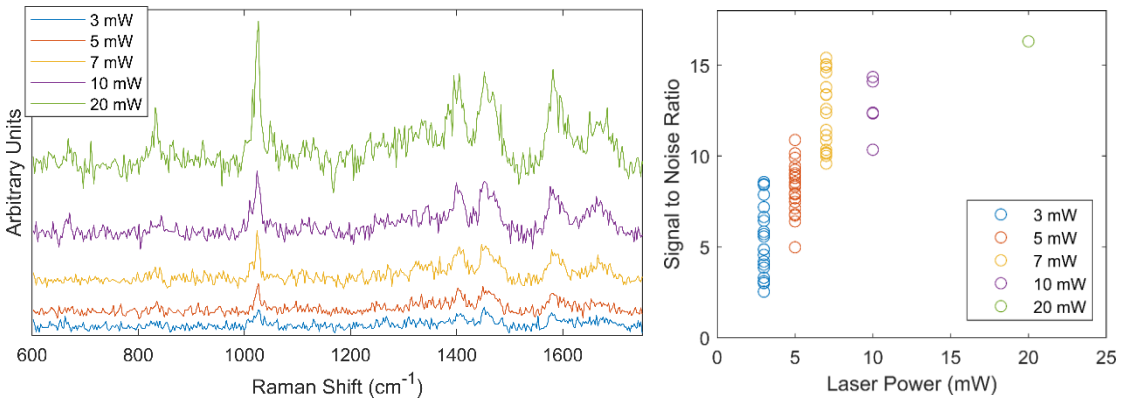

Figure 3.5. (Left) Raman spectra collected from viable spores using 1 s integration times with different laser powers. (Right) SNR of the 1018 cm^{-1} peak for different laser powers

When looking at the Raman spectra for these damaged spores, noticeable changes to the spectrum are observed. The left side of Figure 3.7 shows two spectra collected using 10 mW of laser power. The blue line is a 10× multiplication of the initial spectrum collected after 1 s. After the laser is on the spore for 10 s, the red spectrum was collected. This spectrum is dominated by two man peaks centered at 1355 and 1587 cm^{-1}. These peaks are associated with the D- and G-bands of amorphous carbon [107] and are the result of burning caused by the laser. The right side of Figure 3.7 shows the intensity of the 1587 cm^{-1} peak over time. The spectra from 3 mW and 5 mW laser excitation shows no significant changes in this peak over the 100 s observation period meaning that there is no noticeable sample degradation. This matches the observations in the bright-field images. The spectra from 7 mW, 10 mW, and 20 mW laser excitation show a dramatic increase in

the amorphous carbon peak which corresponds to the sample damage observed in the bright-field images. Sample degradation is observed at 20 mW after 1 s while the damage at 7 mW doesn't occur until after 45 s of interrogation.

For the remainder of this work (unless otherwise noted), a 7 mW laser intensity was used for measurements. This value was selected because the measured SNR going from 7 mW to 10 mW did not show significant improvement. Additionally, observable laser damage was not noted until after 45 s of exposure which is more than 10× longer than our typical long exposures. The exact nature of the sample damage caused by the Raman laser or its effect on viability is unknown, however we believe that this safety factor ensures that any changes caused by the Raman laser are minimal.

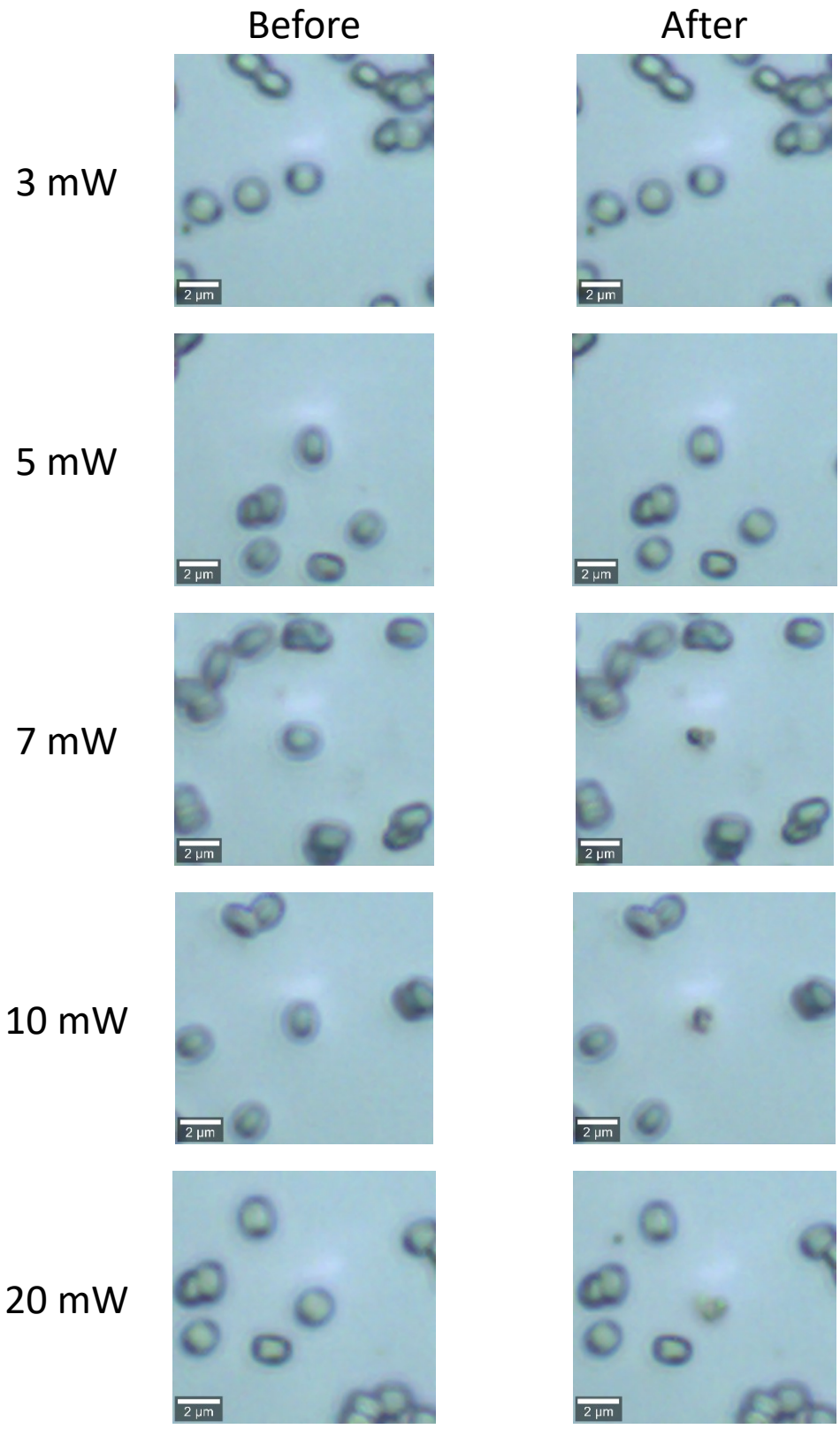

Figure 3.6. Bright-field images of spores before (left) and after (right) 100 seconds of laser interrogation at varying intensities.

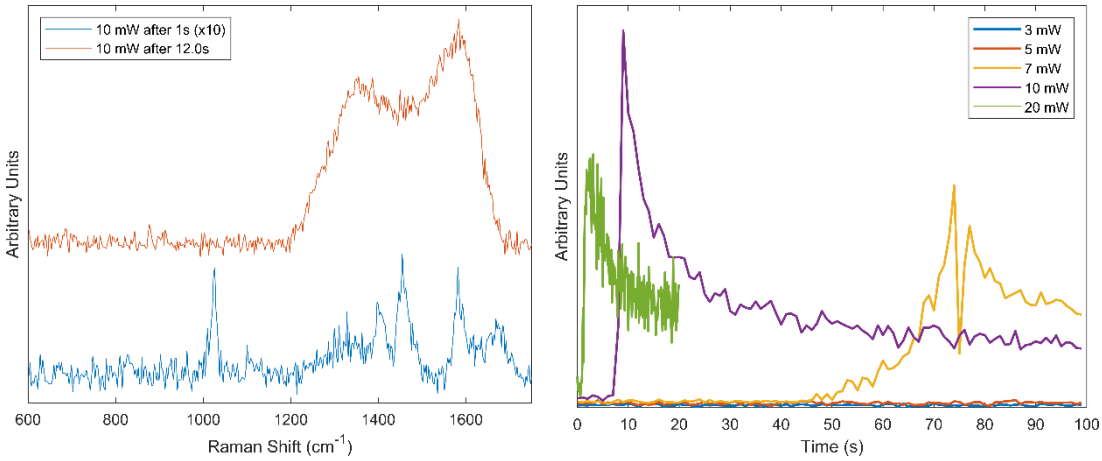

Figure 3.7. (Left) Raman spectrum of a spore with 10 mW laser intensity after 1 second (blue, multiplied by 10 for clarity) and after 10 seconds (red). (Right) Intensity of amorphous carbon peak (1587 cm^{-1}) over time for varying laser powers.

Using this 7 mW laser power we next wanted to determine the minimum interrogation time required to get a suitable signal. To do this, a 4×4 grid of spectra covering 2.5 × 2.5 μm around a viable spore were collected using the "continuous mode" on the Witec microscope. This process was repeated using different integration times ranging from 0.1 to 10 s. The SNR was calculated in the same manner above for both the CaDP peak (1018 cm^{-1}) and the C-H stretch peak (2938 cm^{-1}). The highest observed SNR for each set of 16 spectra are shown in blue in Figure 3.8. The SNR values plateau around 3 s. Although the peak intensity continues to increase linearly (as shown in red in Figure 3.8), the noise also increased for long integration times which prevented improvements to the overall SNR. To maintain high throughput, the shortest possible integration time is desirable. Based on these results, an integration time of 1.5 s was selected as a good combination of high SNR and relatively short time.

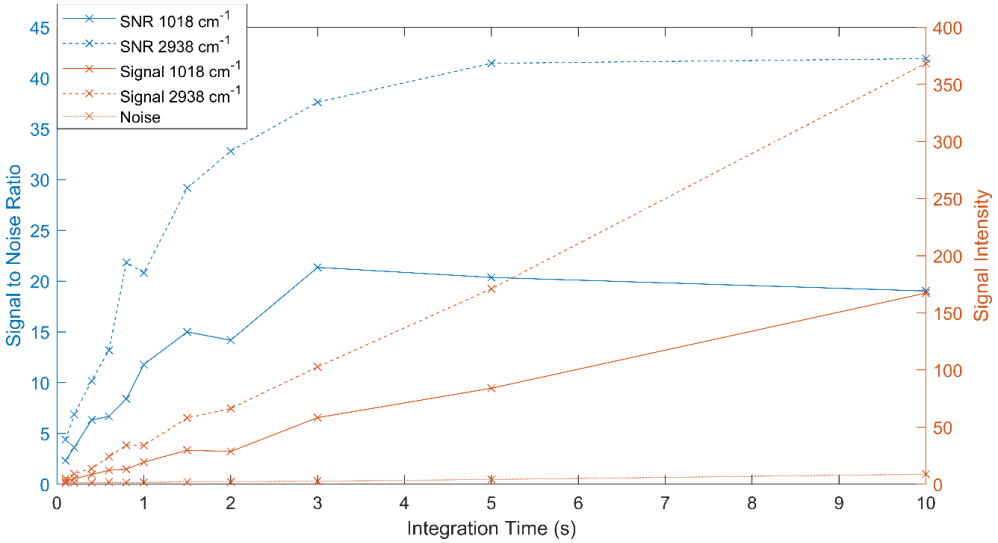

Figure 3.8. SNR for the CaDP peak (1018 cm^{-1}) and C-H stretch (2938 cm^{-1}) (left axis, blue) and the measured signal intensity and noise (right axis, red)

3.4 Registration of Bright-field Images to Raman Hyperspectral Images and Spectral Extraction

As described in Section 1.5.2, Raman chemical images are generated by raster scanning a laser over a sample to collect Raman spectra at each spatial coordinate. This generates a cube of data with spatial information stored along the x- and y-axes and spectral information saved in the z-axis. Since the spatial resolution of bright-field imaging and Raman chemical imaging are both determined by the diffraction limit of visible light, it is technically feasible for Raman chemical imaging to reach image resolutions comparable to those obtained in bright-field images, however because each pixel needs to be measured individually in an RHSC the process of doing so is not practicable due to the time required

to sample each pixel. This means that Raman chemical images typically have significantly lower spatial resolution compared to bright-field images.

The step size for our RHSCs was typically 0.5 μm in both spatial dimensions. Since *Bacillus* spores are ~1 μm in diameter that means that taking a hypercube over a larger region means that each spore could be interrogated multiple times. Similarly, the laser could also interrogate an area where multiple spores are present in the field of view. Because of these factors, it is possible to estimate the number of spores present using these low resolution bright-field images, however it is difficult to demarcate specific viable or non-viable spores in regions of higher spore density. Additionally, the Raman spectra collected over a single spore are not uniform and the fixed step size of the raster scan can lead to the interrogation of spore edges or multiple spores at a time which may not be representative of the spore as a whole. To build an average Raman spectra for a single and specific spore, a method was needed to map each point in the data cube to a pixel in the bright-field image.

Image registration is a process where two different images of the same scene are aligned to overlap one another. Because the bright-field microscopy image is significantly higher resolution than the Raman data cube, straightforward registration techniques were unable to be used. To overcome these challenges, we developed a method to combine all measured Raman spectra from a single spore to obtain an average Raman spectrum for that spore. An example bright-field image of *Bacillus atrophaeus* spores is shown in Figure 3.9a. First, the segment of the RHSC corresponding to the C-H stretch (2938 cm^{-1}, C-H image), shown in Figure 3.9b, was extracted and resized to match the pixel size of the bright-field image using a nearest neighbor interpolation. Figure 3.9c shows an example

of the misalignment present between the bright-field and Raman images prior to registration. A singly dispersed spore in circled on the right side of the image to highlight this misalignment. Next, a non-reflective similarity transform was applied using the Matlab functions 'fitgeotrans' and 'imwarp' to translate, rotate, and scale the bright-field image into alignment with the results shown in Figure 3.9d. Third, the segmentation method, described Section 2.2.1, was then used on the bright-field image as shown in Figure 3.9e to demarcate the spores. Finally, every pixel in each demarcated spore was then mapped back to a spectrum within the RHSC. Due to its higher spatial resolution, pixels in the bright-field image can map back to the same pixel within the RHSC which creates a weighted average spectrum being generated for each segmented region. In order to prevent background (non-spore) data from being included in the average, spectra without the C-H stretch spectral feature at 2938 cm^{-1} were excluded. If more than 25% of the pixels identified within any segmented region mapped to excluded spectra in the RHSC, then the region was considered blank and an average was not calculated. Using this method to threshold out regions without corresponding spectral features was done to overcome the over-segmentation issues explained in Section 2.2.2. The section circled in Figure 3.9f shows spores correctly identified in the segmentation, but not included in the average due to poor Raman signal. This data was collected from top to bottom and experienced a drift in focus as the scan progressed which caused more below threshold pixels to be located toward the bottom of the data cube. The example shown in Figure 3.9 identified and generated spectra for 115 spores. The goal of this method is to generate a large number of high quality weighted average spectra that correspond to single spores which will be discussed in the following sections.

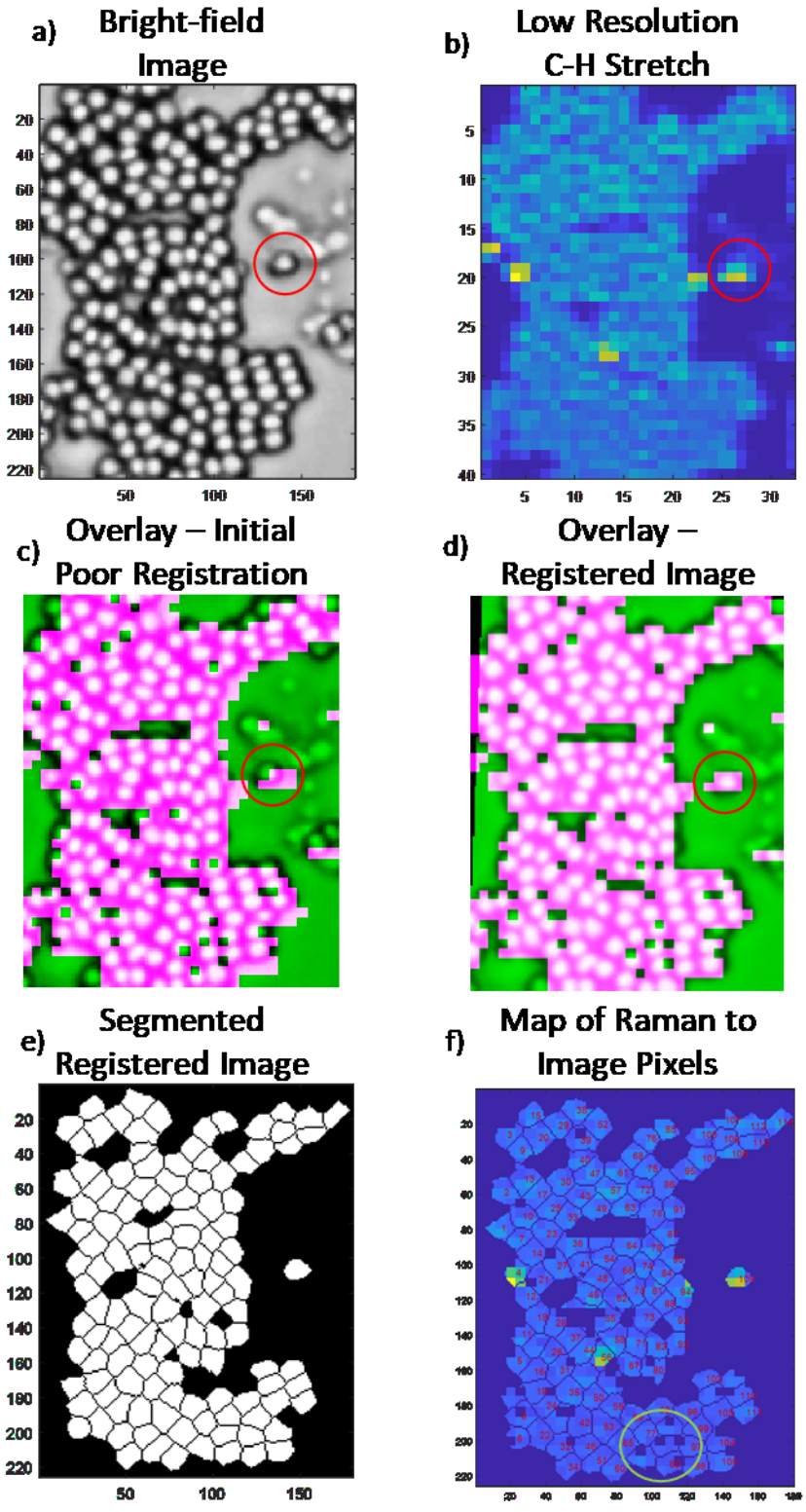

Figure 3.9. The process registering a bright-field image (a) and the C-H stretch segment of an RHSC (b) with initial poor alignment (c). After registration (d) the image is segmented (e) with each region being mapped back to a specific spectrum from the original data cube (f).

3.5 Extracted Single Spore Raman Spectra from Viable and Gamma Irradiated *B. anthracis* delta Sterne

This process was first applied to the viable and gamma irradiated spore samples used for the library development above. Figure 3.10a and Figure 3.10e show samples of the bright-field images of viable and gamma irradiated spores, respectively. These images were then registered to the C-H segment of the RHSCs (Figure 3.10b and Figure 3.10f). Figure 3.10c and Figure 3.10g show each pixel being mapped back to a spectrum from the RHSC which then create weighted average spectra shown in Figure 3.10d and Figure 3.10h. These averaged spectra create a better representation of the spore as a whole to give higher confidence when comparing to a library. The correlation coefficient was calculated for the extracted average spectra for all 325 viable and 150 gamma irradiated spores compared to the library spectra extracted in Section 3.3 for the fingerprint region from 600-1750 cm^{-1} (274 points). A correlation threshold of 0.8 was used to classify each spectrum as either viable or gamma irradiated. If a spore spectrum had a correlation above 0.8 for both the viable and non-viable classes then the higher of the two was chosen for classification (note: the viable and gamma irradiated library spectra had a correlation of 0.7 to each other over the 600-1750 cm^{-1} range). If the correlation was below 0.8 then the spectrum was classified as "other." The results of the library validation are shown in Table 3.1. Of the 325 viable spore spectra, seven did not correlate to either the viable or gamma irradiated library spectra. The 318 correctly classified spores had an average correlation score of 0.989 while the seven outliers averaged 0.519. These outlier spectra were determined to be from leftover growth media and/or remnants of vegetative cells that

remained after the sporulation process. None of the gamma irradiated spores were mis-classified as viable, but five of the extracted spectra were classified as "other." The 145 correctly classified spores had an average correlation score of 0.967 while the outliers averaged 0.553. These outlier spectra were noticeably different from both the viable and the irradiated spores and exhibited distinct peaks at 841 and 959 cm^{-1} (not shown). It was determined that these spectra matched that of PHBA, a biomolecule found in the *Bacillus anthracis* vegetative cells [46].

Table 3.1. Classification results for all viable and all gamma irradiated samples

		Classification Result		
	Total #	Viable	Gamma Irradiated	Other
Viable	325	318 (97.8%)	1 (0.3%)	6 (1.8%)
Gamma Irradiated	150	0 (0%)	145 (96.7%)	5 (3.3%)

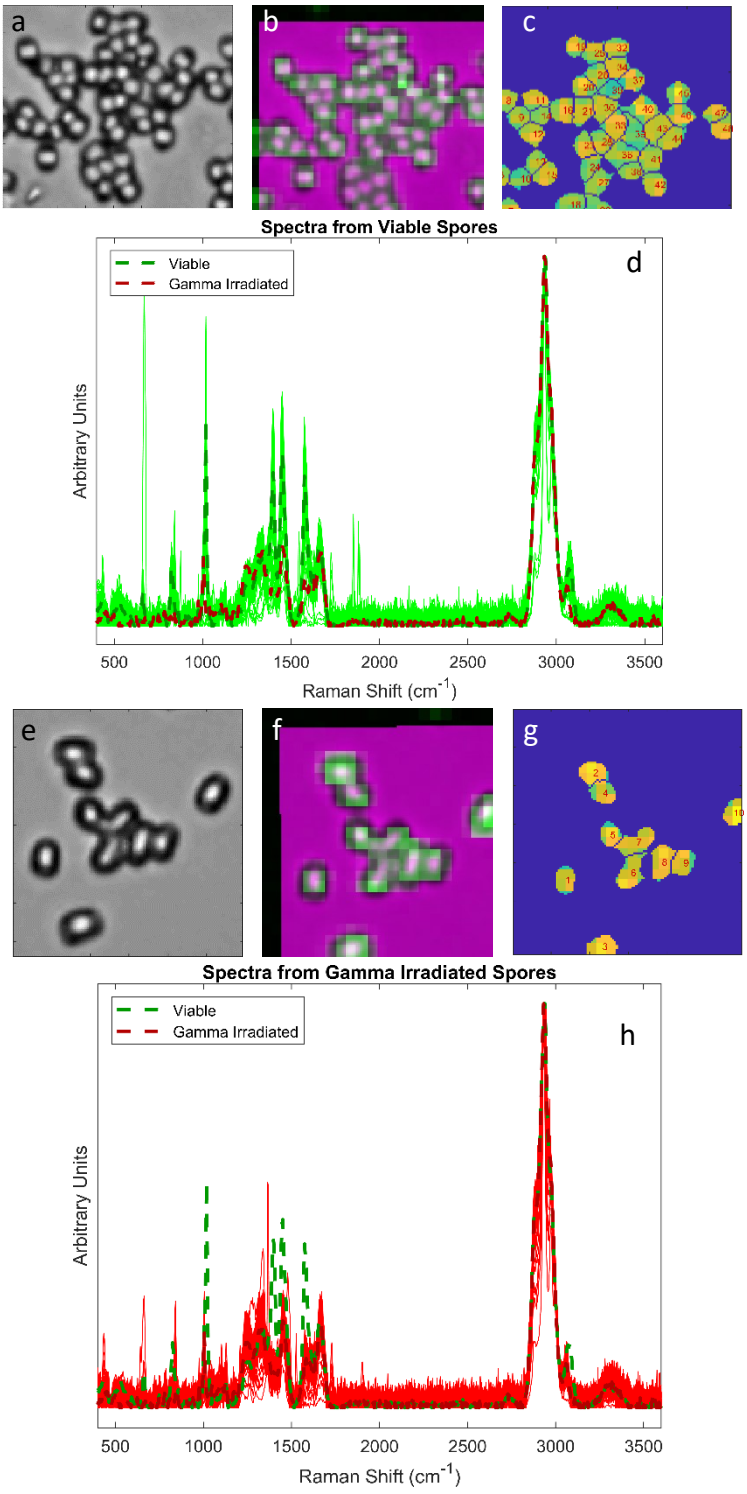

Figure 3.10. (a) Example a bright-field image of all viable spores, (b) that image registered to the C-H region of an RHSC, (c) a map of individual spectra associated with each spore, and (d) a comparison of all extracted viable spores to the viable and gamma irradiated spore library spectra. An example of gamma irradiated spores is shown in e-h.

3.6 Raman Analysis of Different *Bacillus* Species

Due to the potential toxicity of *Bacillus anthracis*, it is regulated at biosafety level 3 (BSL-3) which requires secured containment, certified biological safety cabinets, and the use of a powered air purifying respirator (PAPR) for handling. These burdens to shipment and laboratory personnel means that much of the research applied toward *B. anthracis* is performed on surrogate materials. These materials are often attenuated versions of *B. anthracis* such as the Sterne strain used for much of this thesis or other *Bacillus* strains such as *B. atrophaeus* (formerly known as *B. globigii* and *B. subtilis niger*), *B. thuringiensis*, or *B. megaterium* (this is not an exhaustive list of surrogate materials) [9]. The prevalence of these additional *Bacillus* strains in BW research makes it desirable to understand the spectral similarities and differences between the different strains. Additionally, studying the spectral changes caused using different deactivation methods can help us to understand the exact mechanism that causes a spore to become non-viable.

For this portion of the study, samples of these four spores were procured from the US Army Combat Capabilities Development Command Chemical Biological Center's BioTechnology Branch. The *B. anthracis* Sterne used in this section is from a different batch than the spores used in the remainder of the thesis. This was done to ensure that all four strains were prepared using the same methodology (detailed in Section 1.3.4) to minimize any spectral differences that may have been related to the method of preparation. The spore were measured in their original (viable) state, after exposure of a 2 mL liquid suspension of spores to 50 kGrays of gamma irradiation, and after autoclaving a 0.5 mL suspension of spores at 121 °C for 30 minutes. After both the gamma irradiation and autoclaving, 0.1 ml of each inactivated strain containing at least 5x 107 cfu/mL was

inoculated into 250 ml 0.8% nutrient broth supplemented with CCY salts and incubated at 30 °C and 225 rpm for 2 weeks to confirm lack of growth.

Bright-field images and RHSCs were taken from samples of viable, gamma irradiated, and autoclaved for all four strains. Each measured sample contained only a single type of spore. The bright-field image to RHSC registration technique described in Section 3.4 was used to extract weighted average spectra for each class. All the extracted spectra were averaged together to create a single library spectrum that corresponded to all the spores. The correlation coefficient was then measured for each of the individual extracted spectra compared to this library. Spectra with a correlation coefficient less than 0.95 were excluded from further analysis. This removed approximately 4.5% of the spectra which corresponded to non-spore items such as PHBA, growth media, and/or cellular debris. After this screening was complete, spectra from 8,940 spores remained for analysis. Table 3.2 lists the number of spectra extracted from each class of spore.

Table 3.2. Total number of spectra extracted for each class

	Number of Extracted Spectra		
	Viable	Gamma Irradiated	Autoclaved
B. anthracis Sterne	1179	599	2177
B. *atrophaeus*	541	402	413
B. thuringiensis	939	413	358
B. megaterium	339	541	1039

The spectra were analyzed using principal component analysis (PCA). PCA is a method of reducing the dimensionality of a set of data by solving for a set of eigenvectors which maximizes the variability in the data. This is done by first combining all the measured spectra into an $n \times m$ matrix, $\boldsymbol{X}$, which contains n spectra each containing m data points. The covariance matrix, $\boldsymbol{C}$, is first calculated using the following equation:

$$\boldsymbol{C} = \boldsymbol{X}^{\mathsf{T}}\boldsymbol{X} \tag{3.1}$$

where $\boldsymbol{X}^{\mathsf{T}}$ is the transpose of $\boldsymbol{X}$. This results in an $m \times m$ covariance matrix. Eigenvector decomposition is then performed on the covariance matrix such:

$$\boldsymbol{C} = \boldsymbol{W}\boldsymbol{\Lambda}\boldsymbol{W}^{-1} \tag{3.2}$$

The eigenvector decomposition of the covariance matrix results in the an $m \times m$ matrix of eigenvectors, $\boldsymbol{W}$, and an $m \times m$ diagonal matrix of eigenvalues, $\boldsymbol{\Lambda}$. These eigenvectors, referred to as principal components or PCs, are orthogonal and are arranged such that the first PC (PC 1) has the largest variance with each subsequent PC accounting for less variance. The PCA score (or loadings), $\boldsymbol{T}$, is calculated using the original data and the eigenvectors using the equation:

$$\boldsymbol{T} = \boldsymbol{X}\boldsymbol{W} \tag{3.3}$$

where the score is an $n \times m$ matrix that represents the original data $\boldsymbol{X}$ in PC space [108, 109]. The following sections will detail the PCA scores for these spores.

3.6.1 Viable Spores

All the spectra collected from viable spores are shown in Figure 3.11. The region from 1750-2800 cm^{-1} contains no spectral features for any of the spores so this portion of the spectra and was truncated prior to performing the calculations below and removed from

the plots for clarity. The individual spectra are shown in gray with the average spectrum shown on top. All peaks have been normalized to the C-H stretch at 2935 cm^{-1}. This shows the amount of variation within each set of spectra. The most intra-spore variation for all four strains occurs around the CaDP peaks at 823, 1018, 1402, 1450, and 1575 cm^{-1}. As discussed in Section 3.3.1, this is likely caused by edge effects when the laser interrogates portions of the spore with a lower concentration of CaDP as well as natural variations of CaDP level within the spores. Although these spectra are weighted averages intended to cover an entire spore, misalignment in the registration process and variations on the specific portion of the spore being interrogated for individual spectra like lead to these spectral variations. The *B. megaterium* and *B. thuringiensis* also have transient peaks at 1153 and 1515 cm^{-1}. These peaks are small or nonexistent in the average spectra, but individual average spore spectra within the class shown pronounced features at those locations. These two features appear in approximately 13% of the *B. megaterium* spectra and 16% of *B. thuringiensis* spectra. These spectral features do not correspond to any of the measured biomarkers and are likely remnants of the growth media.

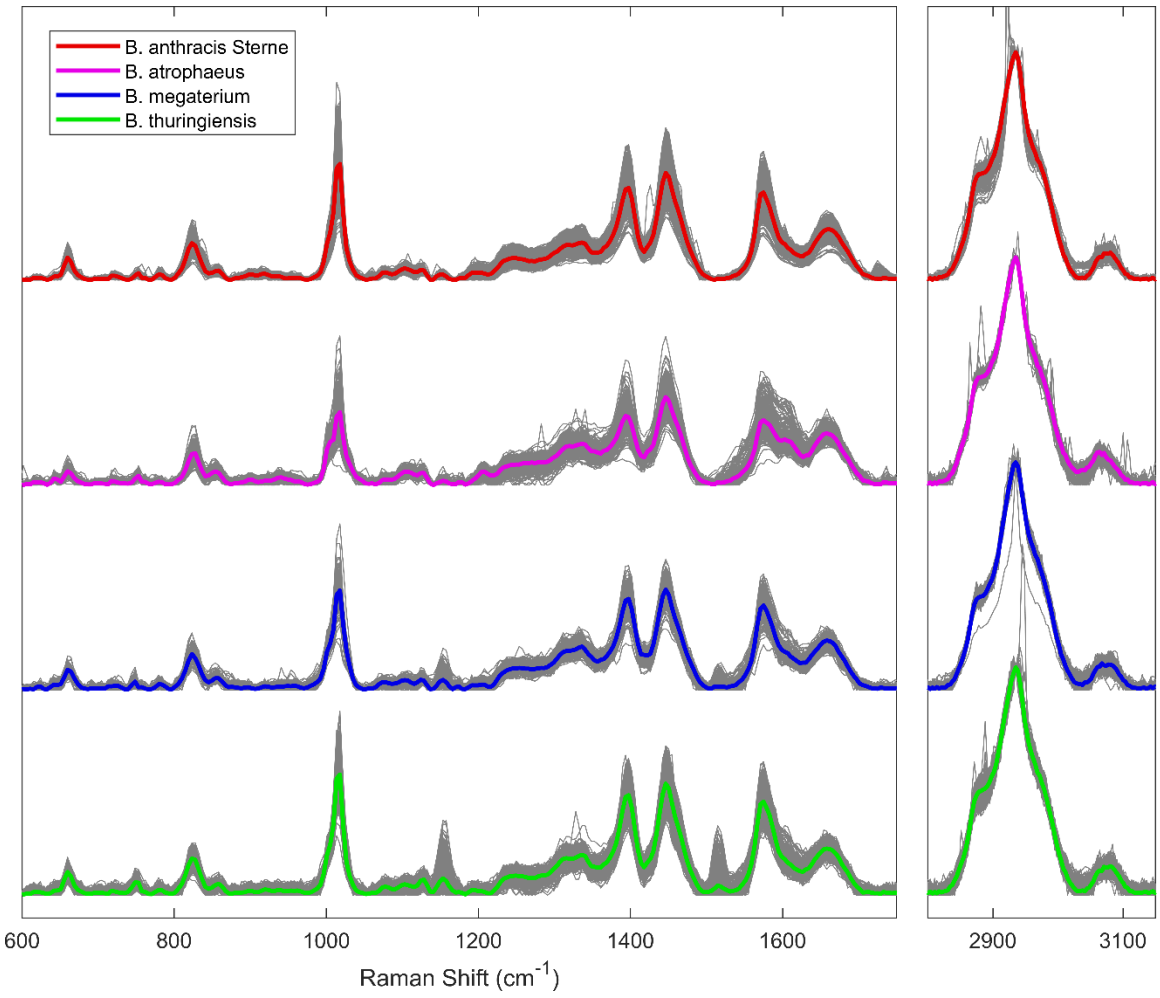

Figure 3.11. Raman spectra collected from the four *Bacillus* species. Individual spectra are shown in gray with the average spectrum on top.

The average spectra for the four strains have are very similar. The cross correlation coefficients were calculated for spectra combining the 600-1750 cm^{-1} and 2800-3150 cm^{-1} spectral ranges which were all >0.98 as shown in Table 3.3. PCA was used to look for variations within the spectrum that could be used to discriminate the four classes. Figure 3.12a shows a plot of the PCA scores for the first two PCs for all 2,998 viable spectra. PC1 can be used to effectively distinguish *B. anthracis* Sterne and *B. atrophaeus* from *B.* megaterium and *B. thuringiensis* while PC2 can be used to discriminate *B. anthracis* Sterne

from *B. atrophaeus*. Significant overlap exists between the populations of *B. megaterium* and *B. thuringiensis* along PC 1 and PC 2 however PC 11 and PC 18 (Figure 3.12b) show good separation.

Table 3.3. Cross correlation matrix for the average spectra of the four *Bacillus* strains.

	BAS	BAt	BM	BT
B. anthracis Sterne (BAS)	1.000	0.990	0.997	0.998
B. atrophaeus (BAt)	0.990	1.000	0.991	0.987
B. megaterium (BM)	0.997	0.991	1.000	0.997
B. thuringiensis (BT)	0.998	0.987	0.997	1.000

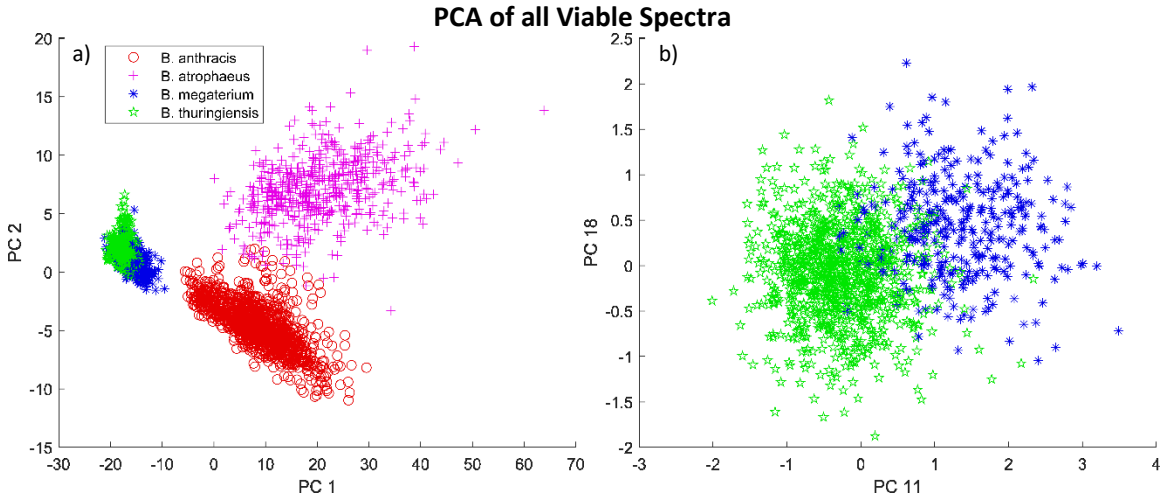

Figure 3.12. a) PCA scores for the first two PCs for *B. anthracis*, *B. atrophaeus*, *B. megaterium*, and *B. thuringiensis*. b) PCA scores for PC 11 and PC 18 for *B. megaterium* and *B. thuringiensis*.

The scree plot in the left of Figure 3.13 shows that 41 PCs are needed to account for 90% of the variance in the data (shown at the dashed line in the figure). PC 1, PC 2, PC 11, and PC 18 are shown in Figure 3.14 compared to the average spectra for all four spore classes. These four PCs, which showed the greatest ability to distinguish the spore strains, are not dominated by a single peak but instead have multiple positive and negative peaks corresponding to peaks and valleys in the original spectra. This means that the discrimination is being accomplished looking at the ratios of specific peaks as opposed to the presence or absence of a specific compound which makes sense given the spores being made from the same underlying chemicals.

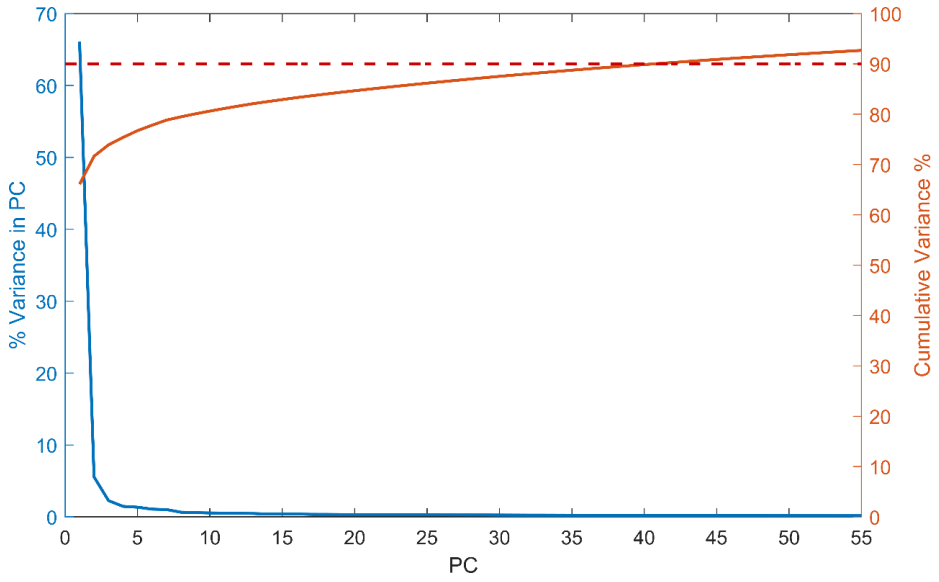

Figure 3.13. Scree plot showing the variance associated with each PC in blue (left axis) and the cumulative variance accounted for in the given PCs (right axis). The dashed red line shows where 90% of the total variance is accounted for.

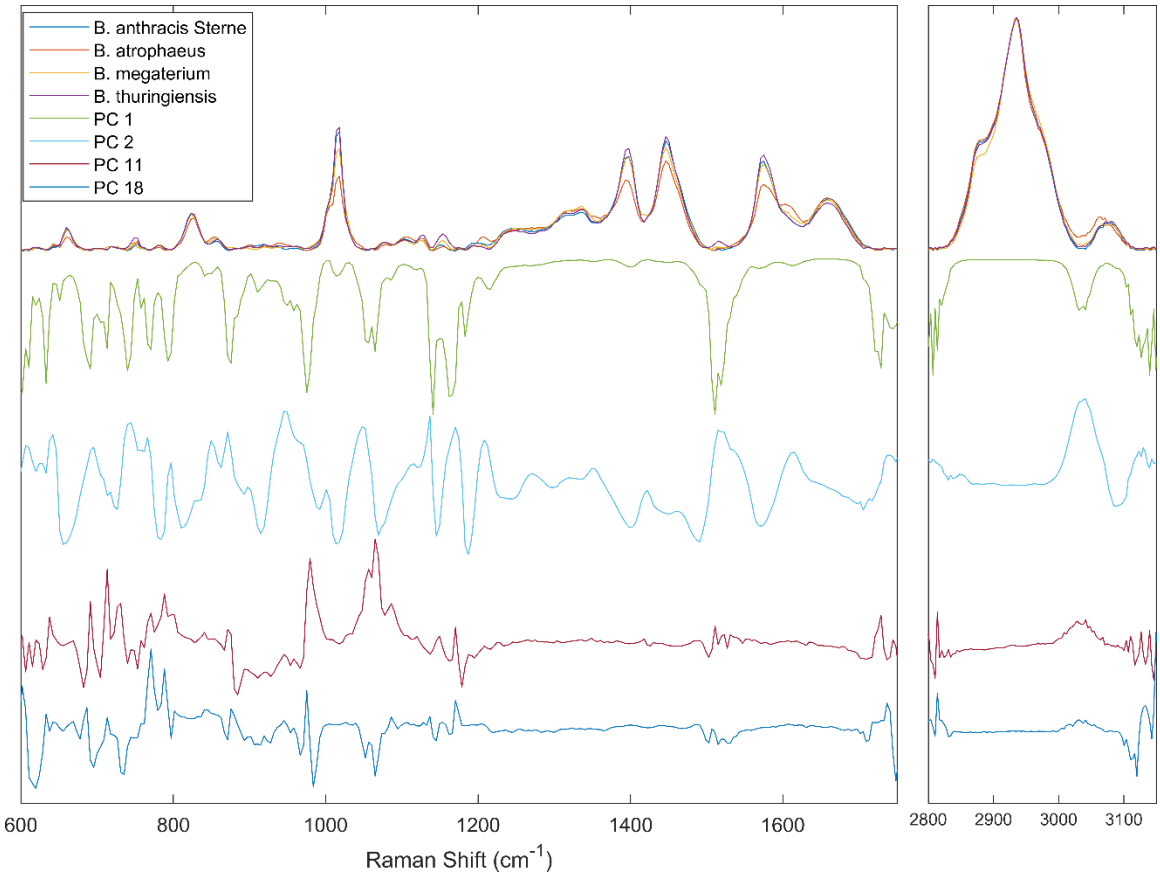

Figure 3.14. Average Raman spectra for all four classes compared to PC 1, PC 2, PC 11, and PC 18.

3.6.2 Deactivated Spores

Raman spectral differences between viable and gamma-irradiated *B. anthracis* Sterne spores were shown in Section 3.3. We will now look for differences between viable spores and spores that have been inactivated using gamma-irradiation and autoclaving for *B. anthracis* Sterne, *B. atrophaeus*. *B. megaterium*, and *B. thuringiensis*. Average spectra for each class are shown in Figure 3.15. These average spectra have been normalized to the C-H stretch at 2935 cm^{-1} (not shown) in order to emphasize the difference in peak intensities between the viable and inactivated spores. Similar to the result shown in Section 3.3, the biggest spectral difference observed between the viable and inactivated spores is

the reduction of the peaks associated with CaDP at 664, 823, 1018, 1402, 1450, and 1575 cm^{-1} which occurred in both the autoclaved and gamma irradiated samples of *B. atrophaeus*. *B. megaterium*, and *B. thuringiensis*.

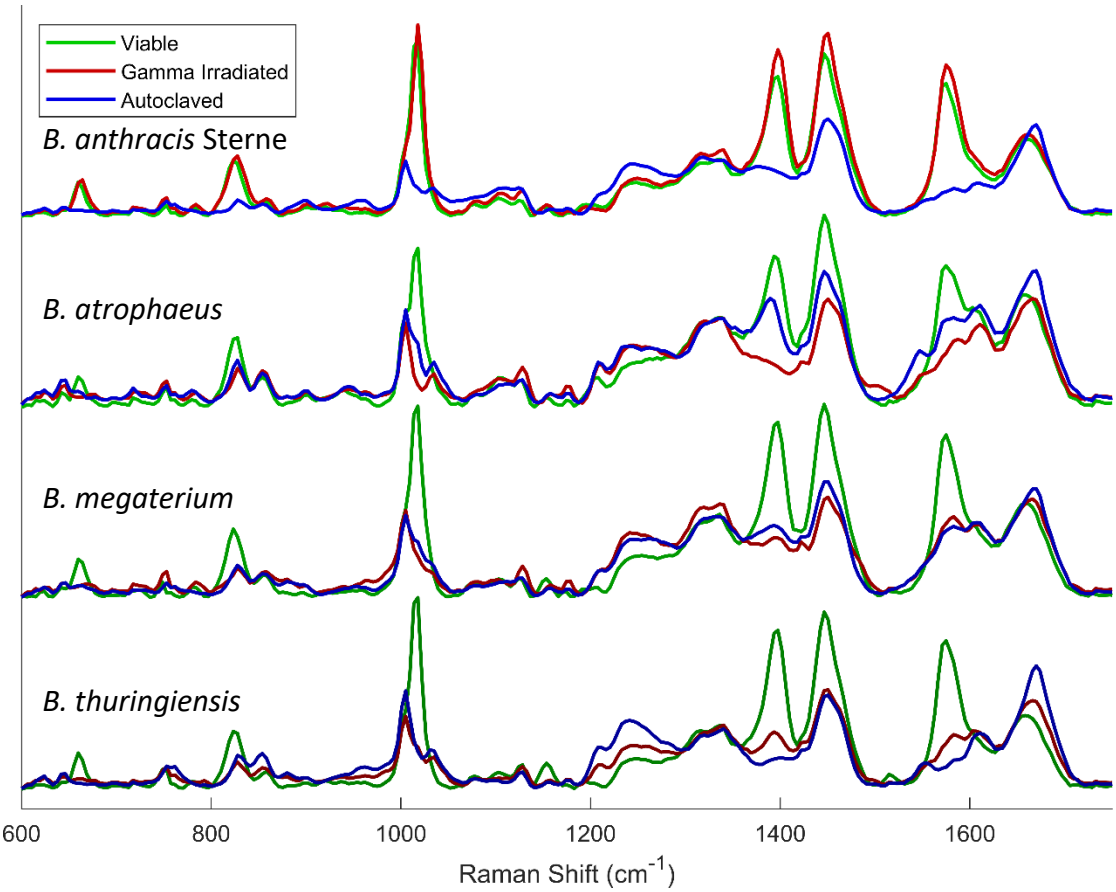

Figure 3.15. Average Raman spectra of *B. anthracis* Sterne, *B. atrophaeus*, *B. megaterium*, and *B. thuringiensis* spores that are viable (green), deactivated with gamma irradiation (red), and deactivated by autoclaving (blue).

This change was also observed in the autoclaved sample of *B. anthracis* Sterne, however it was not present in the gamma irradiated spores as it had been with the previous samples of *B. anthracis* Sterne used throughout the remainder of this thesis. This is attributed to different growth conditions between the two batches of spores. The exact cause and mechanism of this difference is beyond the scope of this effort, however it was

desirable to know whether these gamma irradiated spores could be differentiated from the viable. The correlation coefficient comparing the average spectra of *B. anthracis* Sterne viable and gamma irradiated spores is 0.98 over the 600-1750 cm^{-1} region, however when PCA was performed on all the *B. anthracis* Sterne spectra the viable spectra show distinct separation along PC1 as shown in Figure 3.16. Although the average spectra are very similar, the individual spectra from the gamma irradiated spores generally show more variation than the viable spores as shown in gray on the left side of Figure 3.16. These variations allow for distinct separation between the viable and non-viable spores using PCA.

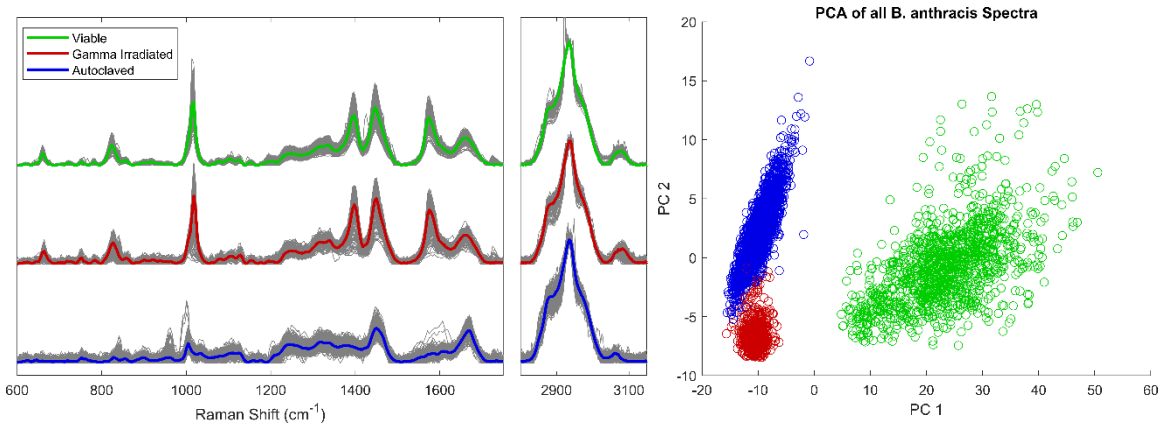

Figure 3.16. (Left) All Raman spectra of viable, gamma irradiated, and autoclaved *B. anthracis* Sterne spores in gray compared to the spectral average. (Right) Plot of the first two PCA coefficients for all *B. anthracis* Sterne spores.

PCA was performed on the other spores as well. The results for *B. atrophaeus and B. thuringiensis* are shown in Figure 3.17 and Figure 3.18, respectively. Both of these spores exhibited distinct separation between the viable and non-viable classes. In the case of *B. megaterium* (Figure 3.19), there is good separation between the classes, however some overlap exists between that could result in misclassification between the two. It was not

possible to achieve full separation using higher principal components. *B. megaterium* provides the opposite scenario from *B. anthracis* Sterne in that the average spectra for the classes show significant differences (correlation between viable and autoclaved in 0.80 and the correlation between viable and gamma irradiated is 0.71), however the variations in the individual spectra make separation of the viable and non-viable classes challenging.

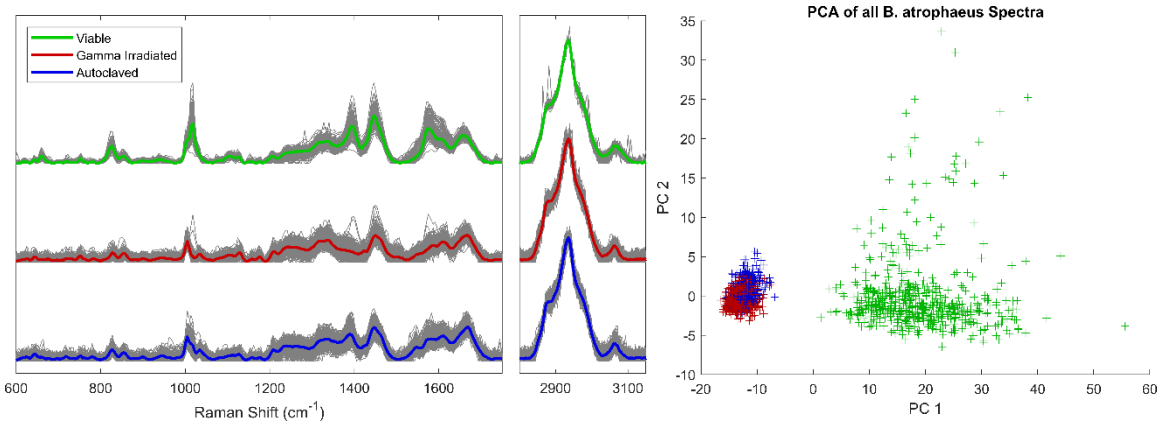

Figure 3.17. (Left) All Raman spectra of viable, gamma irradiated, and autoclaved *B. atrophaeus* spores in gray compared to the spectral average. (Right) Plot of the first two PCA coefficients for all *B. atrophaeus* spores.

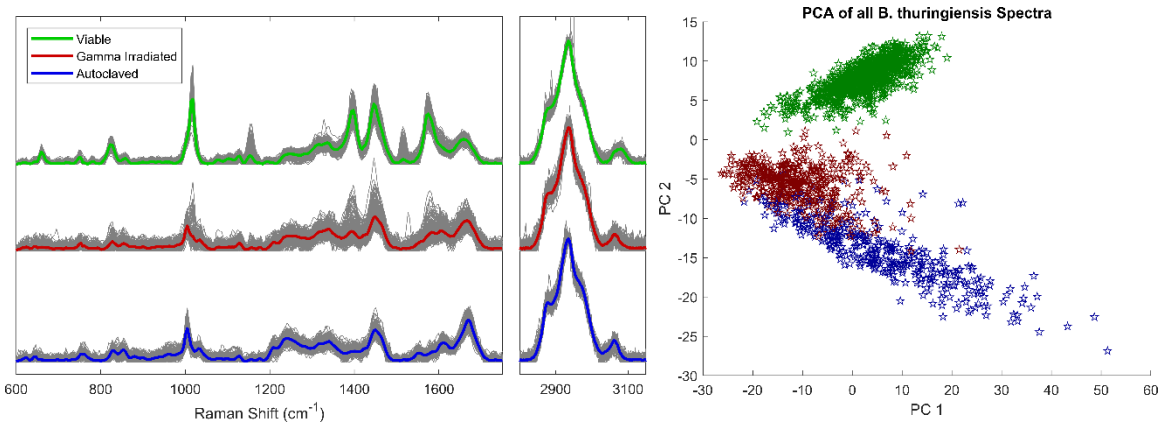

Figure 3.18. (Left) All Raman spectra of viable, gamma irradiated, and autoclaved *B. thuringiensis* in gray compared to the spectral average. (Right) Plot of the first two PCA coefficients for all *B. thuringiensis spores*.

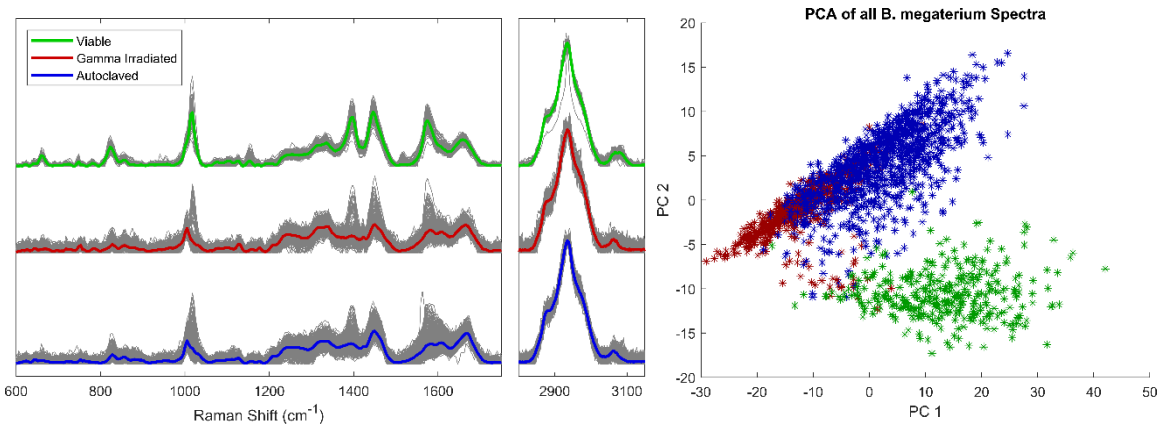

Figure 3.19. (Left) All Raman spectra of viable, gamma irradiated, and autoclaved *B. megaterium* in gray compared to the spectral average. (Right) Plot of the first two PCA coefficients for *B. megaterium* spores.

In general, Raman spectroscopy has shown the ability differentiate viable and non-viable spores. Although the different spectral changes were observed between the batch of *B. anthracis* Sterne spores from this section and those used throughout the remainder of the thesis, the ability to differentiate the classes within the same batch was demonstrated. Chapter 4 will describe a process to find analyze spores and after deactivation. In this process potentially viable spores are targeted and then have their viability confirmed with Raman using library matching. This analysis shows that the library used may need to be taken from the same batch of spores as the analysis to confirm viability.

CHAPTER 4

TARGETING OF SPORES FOR RAMAN ANALYSIS

4.1 Introduction

Chapter 3 showed spectral differences between viable and non-viable spores that were inactivated using gamma irradiation and autoclaving. In this chapter the ability to identify viable spores within a mixture of viable and gamma irradiated spores will be studied and demonstrated. Originally this will be done on full RHSCs using the procedure shown in Figure 4.1a. This process is effective, however collecting a full hypercube over a deposition of spores can be time consuming and result in extraneous sampling of regions where no spores were present. In order to cut down on the overall scan time it is desirable to target individual spores for Raman analysis to determine their viability with minimal

background scanning. To do this, the bright-field imaging segmentation procedure detailed in Chapter 2 was integrated into the Raman analysis procedure as shown in Figure 4.b.

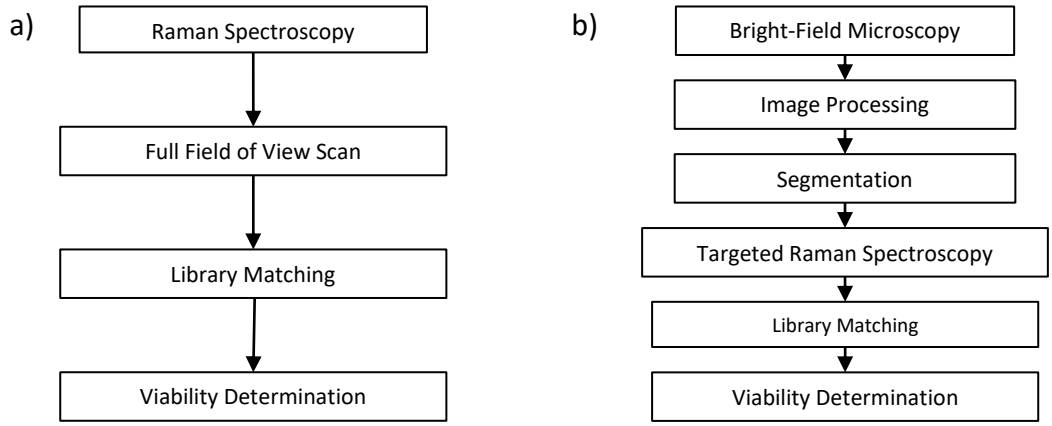

Figure 4.1. Flow chart showing the two data collection procedures used in this chapter a) full RHSC collection and b) targeted Raman analysis.

A scan efficiency term is defined and targeted and RHSC scans are performed on the same FOV for two different samples. The first is sparsely populated with spores while the second is densely populated. The results and overall collection efficiency are compared to show two extreme scanning scenarios and the benefits and limitations associated with each.

4.2 Identification of viable and non-viable spores in a mixed field of view using RHSC

To demonstrate the ability to differentiate viable from non-viable spores in a mixed FOV using an RHSC, a 50:50 mixture of viable and gamma irradiated *B. anthracis* Sterne spores was examined. Figure 4.2a shows the bright-field image (549×760 pixels) of the mixture. A 43×59 pixel RHSC was generated over this FOV using 532 nm laser excitation

at 4 mW and a 2 s integration time per pixel. Each spectrum was classified as viable or gamma irradiated using the correlation coefficient calculated from 600-1750 cm^{-1} compared to library elements of viable and gamma irradiated spores and PHBA as described in Section 3.5. Figure 4.2b shows all pixels with a correlation coefficient above 0.8 to the viable library spectrum as green and above 0.8 to the gamma irradiated library spectrum as red. PHBA was also present in the sample and pixels that matched its spectrum with a correlation above 0.8 are marked in blue. The results from the RHSC have been scaled up and overlaid on the bright-field image for context. As discussed in Section 3.4, this method can be used to estimate the numbers of viable and non-viable spores, however the spectra can be noisy and it can be difficult to identify where one spore ends and another begins.

Segmenting the image (Figure 4.2c) and mapping the spectra back to pixels in the bright-field image was used to generate weighted average spectra with higher SNR (compared to the RHSC) for each segmented region that could be tied to a specific spore (as described in Section 3.3). Figure 4.2d shows spore level identifications determined by calculating the correlation coefficient for the weighted average against the library elements and using the same correlation threshold of 0.8 and colors as described above. Using this method provides higher fidelity and increases confidence in the results. Objects from the bright-field image without color correspond to regions that either did not match the size parameters for segmentation, did not have enough spectra with the C-H stretch spectral feature at 2938 cm^{-1} to generate an average spectrum, or the average spectrum that was generated for the region did not correlate to viable or gamma irradiated spores or PHBA.

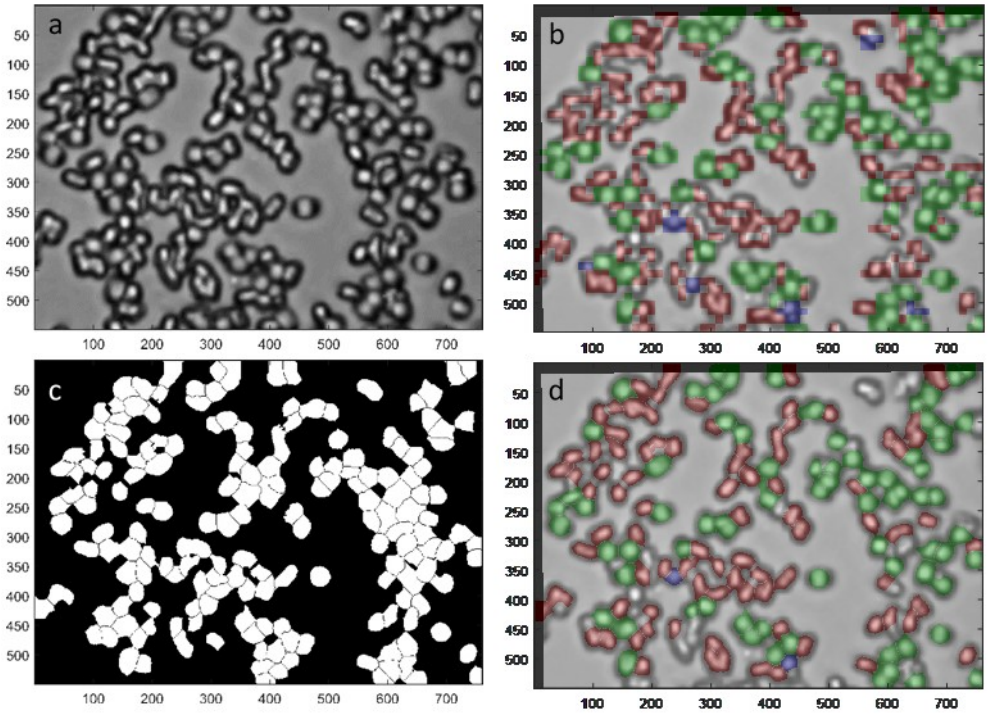

Figure 4.2. (a) Bright-field image of a mixture of viable and gamma irradiated spores. (b) Map of spectral correlation scores with pixels >0.8 marked green for viable and red for gamma irradiated. (c) Segmented bright-field image. (d) Map of spore level spectral correlation scores >0.8 marked green for viable and red for gamma irradiated.

This method shows the ability of Raman microscopy to differentiate viable and gamma irradiated spores. However, acquiring RHSCs that cover the entire FOV results in a large amount of spectral data obtained from empty areas on the slide and is time consuming. For example, of the 2537 total spectra collected in this RHSC, 1552 (61%) did not exhibit a C-H feature. This means that there was no spore present for interrogation resulting in collection of extraneous data.

4.3 Targeted Raman Analysis

4.3.1 Targeting using bright-field images

To reduce the amount of extraneous data collection (no spores in the FOV) and the overall time when collecting full RHSCs, it was desired to develop a process to target spore-like objects and perform Raman collection only at those locations. The segmentation procedure described and characterized in Section 2.2 showed good performance identifying spore-like objects in bright-field images and was robust against changes in contrast and resolution and was thus selected to determine the spore locations.

To perform the targeting, the bright-field image was first collected on the Raman microscope. Figure 4.3 shows a 92 × 53 μm FOV containing a 50:50 mixture of viable and gamma irradiate *B. anthracis* Sterne spores. The same watershed segmentation technique described detailed in Section 2.2.2 was applied to this image using a 3×3 spatial filter and 17 pixel disk shaped structuring element. After the background was removed, pixels with an intensity of 15 or lower was set to zero to prevent over-segmentation. The watershed technique was then applied and regions between 11 and 500 pixels were kept for Raman targeting. The centroid of each region was determined using the 'regionprops' function in Matlab. Figure 4.4 shows an expanded view from the area marked with the red box in Figure 4.3 showing the segmented region and targeted spores.

Using the microscope software it was possible to determine the overall size of the image in both microns and pixels and the position of the image center using the microscope's coordinate system. Using these values, the centroid location for each identified region was converted from the pixel value determined in Matlab to a distance in microns which would be used to direct the Raman microscope to a specific point.

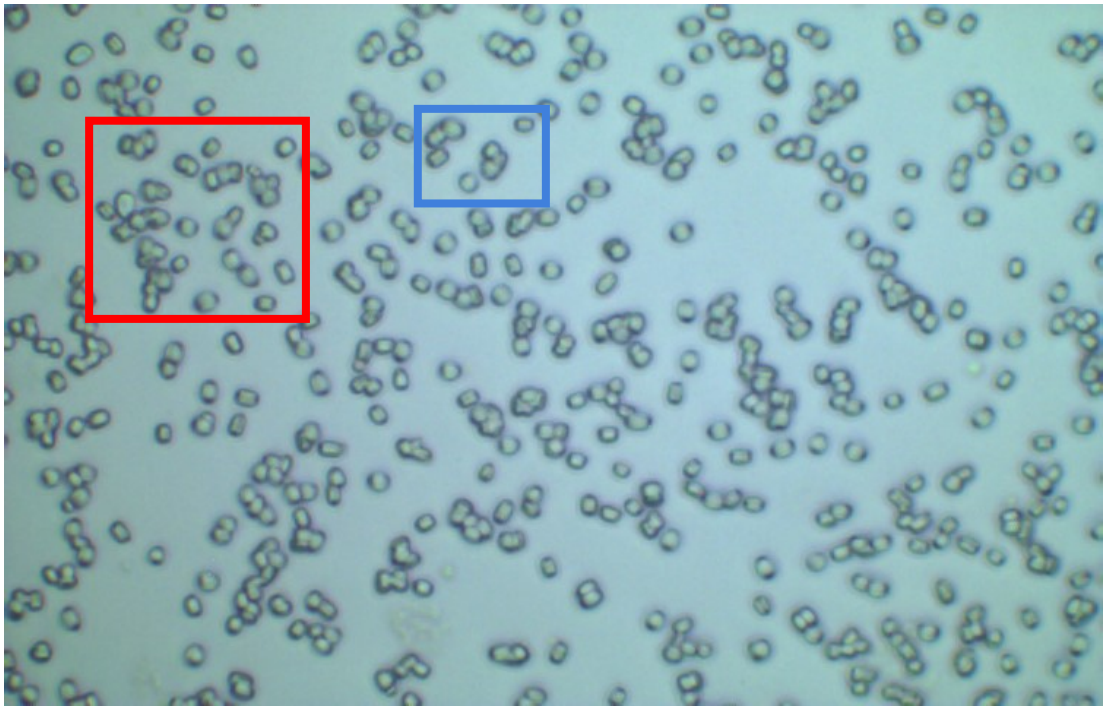

Figure 4.3. Bright-field image of a 50:50 mixture of viable and gamma irradiated *B. anthracis* Sterne spores. The regions in the red and blue boxes are expanded in Figure 4.4 and Figure 4.6, respectively.

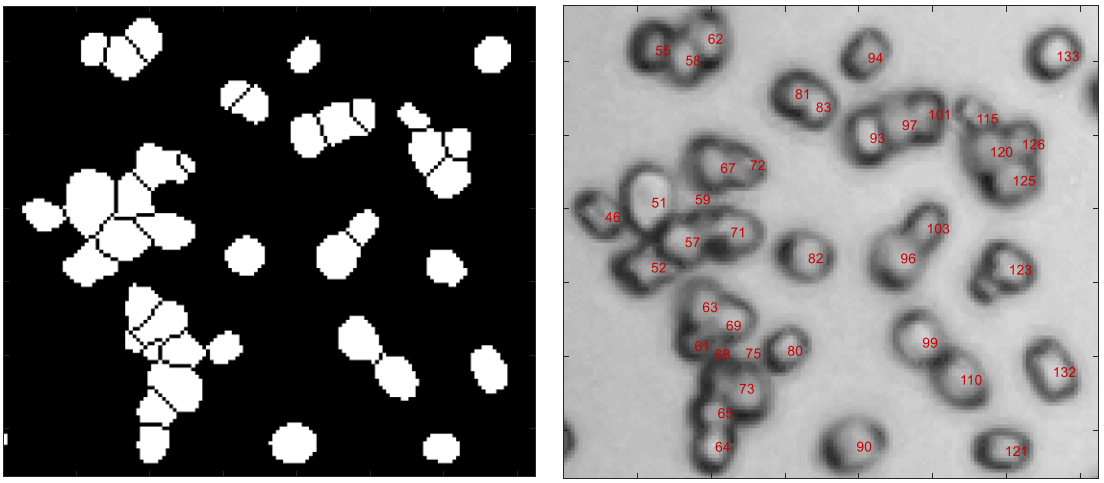

Figure 4.4. Detailed section of Figure 4.3 showing segmented regions and targeted spores

By default, the 'regionprops' function in Matlab orders objects from top to bottom along a single column, shifts one column and repeats. When this information is input into the microscope, this created a sub-optimal travel path as shown in Figure 4.5a. This default

path for Figure 4.3 was 8759.2 µm. To reduce the time to move between targets and the amount of stress and wear placed on the positioning stage, a routine was written to minimize the travel path. The total travel range was divided into equally sized regions typically on the order of 20 regions tall and 5 regions wide as defined by the user. Starting at the left side of the bottom left region, all points were ordered going left to right. Then all the points in the region above were ordered going right to left. This snake pattern continues up the first column before moving to go down the second column. The general pattern is shown as the red line in Figure 4.5b while the specific path required for the targeted spores is shown in blue. The dashed black lines show the boundaries for the regions. After ordering all the points, the total travel distance was calculated. The number of rows and columns was automatically varied around the original settings and the combination that produced the minimum travel distance was used to program the microscope target list. For this image, the minimum travel distance was 1591.8 µm and occurred when the image was divided into 15 rows with 5 columns.

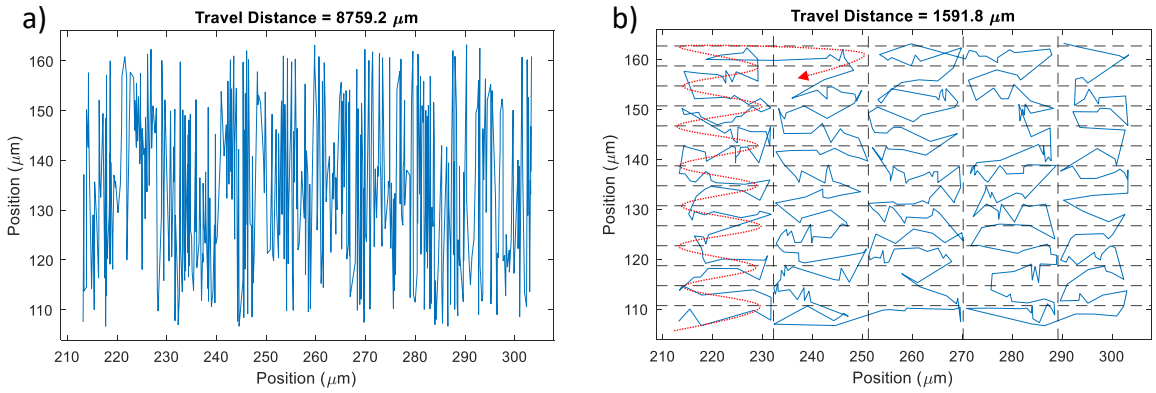

Figure 4.5. Example microscope travel paths showing a) the default Matlab ordering and b) minimized path created by separating into 15×5 regions (dashed black lines). The general pattern is shown as the dashed red line with the specific path taken to interrogate the targeted spores is shown in blue.

It should be noted that the 11 to 500 pixel allowable size range is significantly different than the 60 to 280 pixel range used Section 2.2. The reason for this is twofold. First, an upgrade in the microscope control software allowed for the raw image files to be exported whereas the older images showed in Section 2.2 were interpolated. These interpolated images did not affect the overall shape of the regions, but changed the size the area that each pixel covered. The average spore in this image covers 81 pixels while the older images have an average spore size of 152 pixels despite being collected from the same microscope slide using the same instrument. The second reason for this change is more relevant to the application: to use this method to screen for potential hazards. Failing to correctly characterize a viable spore could result in negative health outcomes. The allowable size range was expanded to reduce the risk of failing to properly demarcate potential spores resulting in a false negative result.

One effect of decreasing the allowable region size is that there exists the possibility that two small regions could be located next to each other that fall within the diffraction limit of the Raman interrogation laser. This could lead to extraneous data collection of what is effectively the same location. To prevent this from occurring, a check was added to determine if the centroids from any two regions were less than 0.65 μm from each other. If regions were found that met this criterion, a morphological opening was applied to remove the watershed line from between the regions. An example from Figure 4.3 (marked in the blue box) is shown in Figure 4.6. The left shows a detailed view of the original bright-field image. The spore in the center was originally segmented as two regions whose centroids were spaced 0.62 μm apart. After the morphological opening was applied (right)

the two regions became one. The centroid for this newly combined region was then calculated and used for analysis.

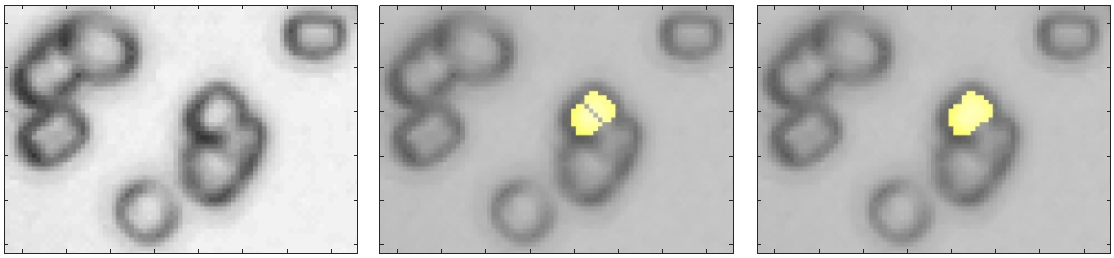

Figure 4.6. Detailed view of Figure 4.3 showing the bright-field image (left) in which a spore was segmented in to regions that were separated by 0.62 um (middle), but recombined into a single target (right) prior to laser interrogation.

4.3.2 Collection of targeted Raman spectra

A total of 513 regions were identified in Figure 4.3. Ideally, the microscope would be able to direct the laser directly to the region centroid and perform a single scan to collect a Raman signature, however limitation in stage reproducibility prevent this level of precision positioning. The microscope uses two stages. The first is a stepper stage that covers a 25 × 25 mm scanning range. The stepper stage has 100 nm resolution with a 0.5-1 μm repetition accuracy. The second is a high precision piezo stage with a 100 × 100 μm scanning range with a resolution of 1 nm and ±5 nm repeatability. The piezo stage has the reproducibility required to effectively target individual spores, however it has a slow travel speed and limited travel range. In order to position with the speed and total range required to target the spores both stages are used, however, reproducibility error and hysteresis in the stepper stage causes the positioning to drift over use. Since the laser focal size, stage error, and spores are all approximately 1 μm, this drift in positioning can cause the microscope to miss the targeted spores over time.

To overcome the limitations of stage positioning, a sampling of points around the region centroid were measured. For the example from Figure 4.3 a 4×4 grid covering 2.5 × 2.5 μm around the target centroid was measured resulting in a total of 16 spectra being generated for each identified region.

The standard Witec Control software can measure a series of spectra at a list of coordinates, but it cannot measure Raman maps at these points. Additionally, the process of measuring a single point cannot be done when the auto-focusing is in operation. The Zeiss EC Epiplan-Neofluar DIC 100× objective used for these measure7ments has a NA of 0.9 has a depth of field < 1 μm which made the auto-focusing function necessary for long scans because variations in laboratory conditions can cause the focus to drift over time and reduce the Raman signal when it was not used. Therefore a program was written in Labview (National Instruments, Austin, TX) to interface with the native Witec Control software which added the functionality of autofocus and Raman mapping at each target location.

4.3.3 Spectral Classification of Targeted Raman Scan

The correlation coefficient was calculated on each of the 16 spectra collected for a region to classify the spores present in the FOV. Each spectrum was compared to the library spectra of viable *B. anthracis* Sterne spores, gamma irradiated *B. anthracis* Sterne spores, and PHBA. The correlation was calculated for the spectral fingerprint region of 600-1750 cm^{-1}. The correlation coefficients were then used to separate the spectra into three categories.

The first set of spectra had correlation coefficients of 0.8 or higher (hereafter referred to as the high threshold). An example of this is shown in Figure 4.7. The four spectra at the bottom of the figure each have a correlation coefficient >0.8 and any one of those spectra being present at a target location would result in the region being classified as a detection. For reference, the average of those four spectra are shown in the middle (blue) with the viable spore library spectrum at the top (green).

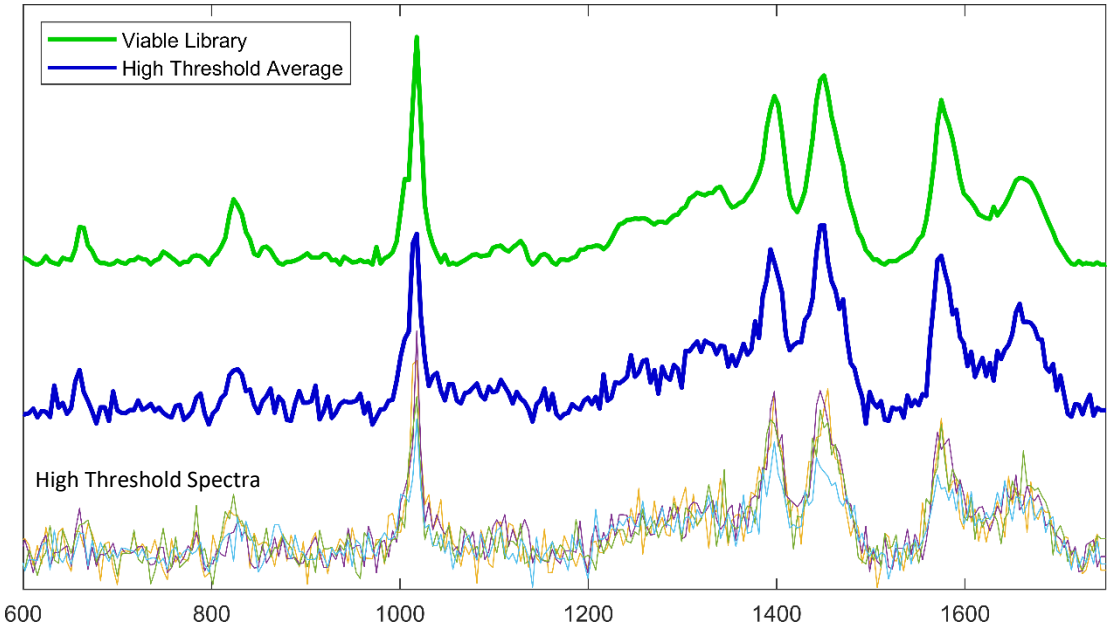

Figure 4.7. Example of a high threshold alarm. Four of the 16 spectra collected at this location (shown in bottom of the figure) had correlation values of 0.8 or higher. The average of these high threshold spectra (middle) had a correlation of 0.96 when compared to the library for viable *B. anthracis* spores (top).

The second set of spectra had correlation coefficients of 0.6 or higher (low threshold). An example of this is shown in Figure 4.8. The eight spectra shown at the bottom did not match as closely to the library, but show some spectral similarity. An average spectrum of all the low threshold spectra was created (middle, blue) and the correlation coefficient was calculated again. If the low threshold average spectrum had a correlation coefficient

greater than the high threshold the region was also classified as a detection. In this example, the average of the eight low threshold spectra had a correlation coefficient of 0.87 to the gamma irradiated library spectrum shown at the top. If the average of all the spectra above low threshold is less than the high threshold then the region was classified as no target being present.

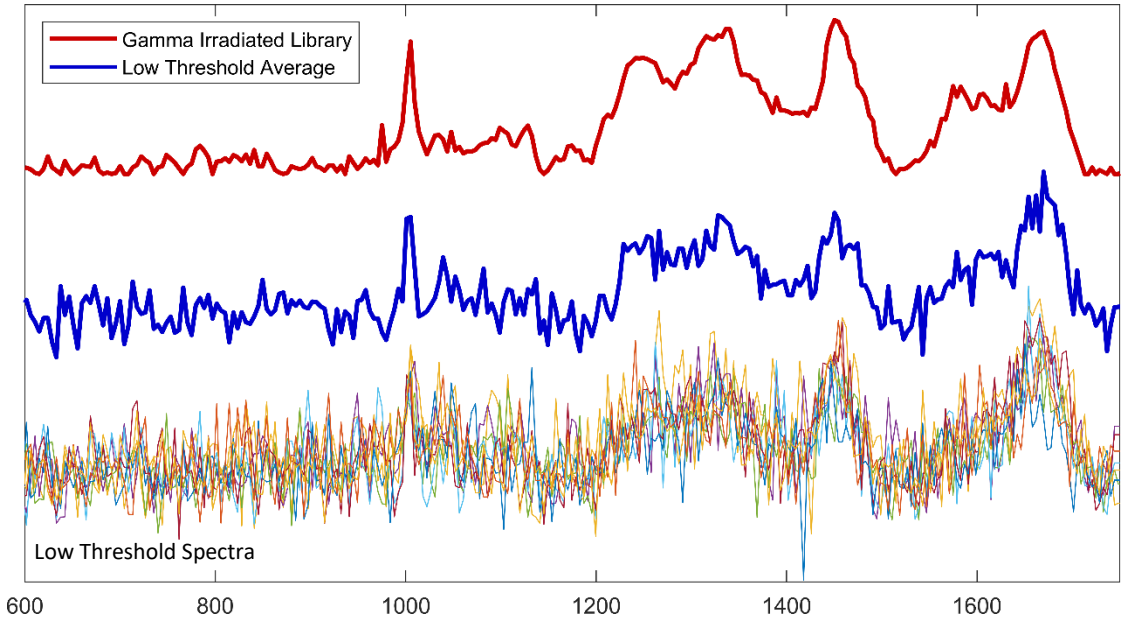

Figure 4.8. Example of a low threshold alarm. Eight of the 16 spectra collected at this location (shown in bottom of the figure) had correlation values between 0.6 and 0.8. The average of these low threshold spectra (middle) had a correlation of 0.87 when compared to the library for gamma irradiated *B. anthracis* spores (top).

The third set of spectra had a correlation coefficient below the low threshold. If all of the spectra fall below the low threshold then no further analysis is performed and the region is classified as a non-detection.

The results from these two classification methods were combined and if either method found a detection then the region was identified as that material. Since measurements were taken over a 2.5 × 2.5 µm region and the spores are typically ~1 µm in size there is the potential that some Raman spectra may have been collected from materials adjacent to the

targeted spore. This means that the set of 16 collected spectra from a region could be classified as multiple materials. These results can be displayed in different manners depending on the application. For this thesis, priority was given to spores (both viable and gamma irradiated) over PHBA in regions with multiple classification results. If spectra corresponding to both viable and gamma irradiated spores were in a single region then whichever class had more low threshold (which also include high threshold) spectra were displayed in the results figures. This was done to allow for better comparison to the RHSC results in which each spectra could only be classified as a single compound. For the end state application of finding a small number of viable spores within a large field of gamma irradiated spores, output results would give priority to viable spores to reduce the likelihood of a viable spore passing screening undetected.

4.3.4 Results and Comparison of Targeted Raman Scan

The results from this targeted method were compared to the two RHSC methods discussed in Section 4.2 for the same FOV shown in in Figure 4.3. For both of these methods, the same 114×186 pixel RHSC was used. A 1.5 s integration time with a 7 mW 532 nm laser was used for each point in the RHSC and for each of the 16 spectra collected at each location for the targeted scan. The targeting process identified 513 spore-like objects for analysis. Table 4.1 compares the collection times for the two acquisition methods. The collection time for the targeted scan was determined by multiplying the total number of spectra by the integration time and adding in 1 s to account for the time required to move the objective to the next spore for interrogation. The RHSC collection over this

FOV took approximately 9 hours and was about 2.5× longer than the targeted scan which was about 3.5 hours.

Table 4.1. Comparison of collection time of RHSC to targeted scan

	Total Spectra	Integration Time (s)	Collection Time (s)	Collection Time (H:MM)
RHSC	21,204	1.5	31,806	8:50
Targeted	8,208	1.5	12,825	3:34

Prior to analysis, cosmic rays and background baseline were removed from all spectra. In the first RHSC method, the correlation coefficient was calculated for each spectrum from within the cube against the library elements for viable and gamma irradiated *B. anthracis* Sterne spores and PHBA for the fingerprint region from 600-1750 cm^{-1}. The SNR for these individual spectra was low, so a correlation threshold of 0.35 was used for classification. This correlation value is lower than is typically used for library matching, however for this application where there is a limited number of library elements to be identified on a controlled and spectrally flat background substrate such that this type of low correlation classification protocol proved effective for low SNR spectra collected in RHSCs. Every spectrum with a correlation coefficient of 0.35 to one of the library elements was color coded either green for viable, red for gamma irradiated, or blue for PHBA. If a spectrum had a correlation of 0.35 or higher to more than one library element, then the higher of the correlation was used for the classification shown in Figure 4.9a. The registered bright-field and RHSC method results in the averaging of multiple spectra which improved the SNR and allows a correlation threshold of 0.7 to be used for classification with the results shown in Figure 4.9b. Finally, the targeted results used the classification method described in Section 4.3.3 with a High threshold of 0.8 and a low threshold of 0.6. The classification results from the targeted scan is shown in Figure 4.9c.

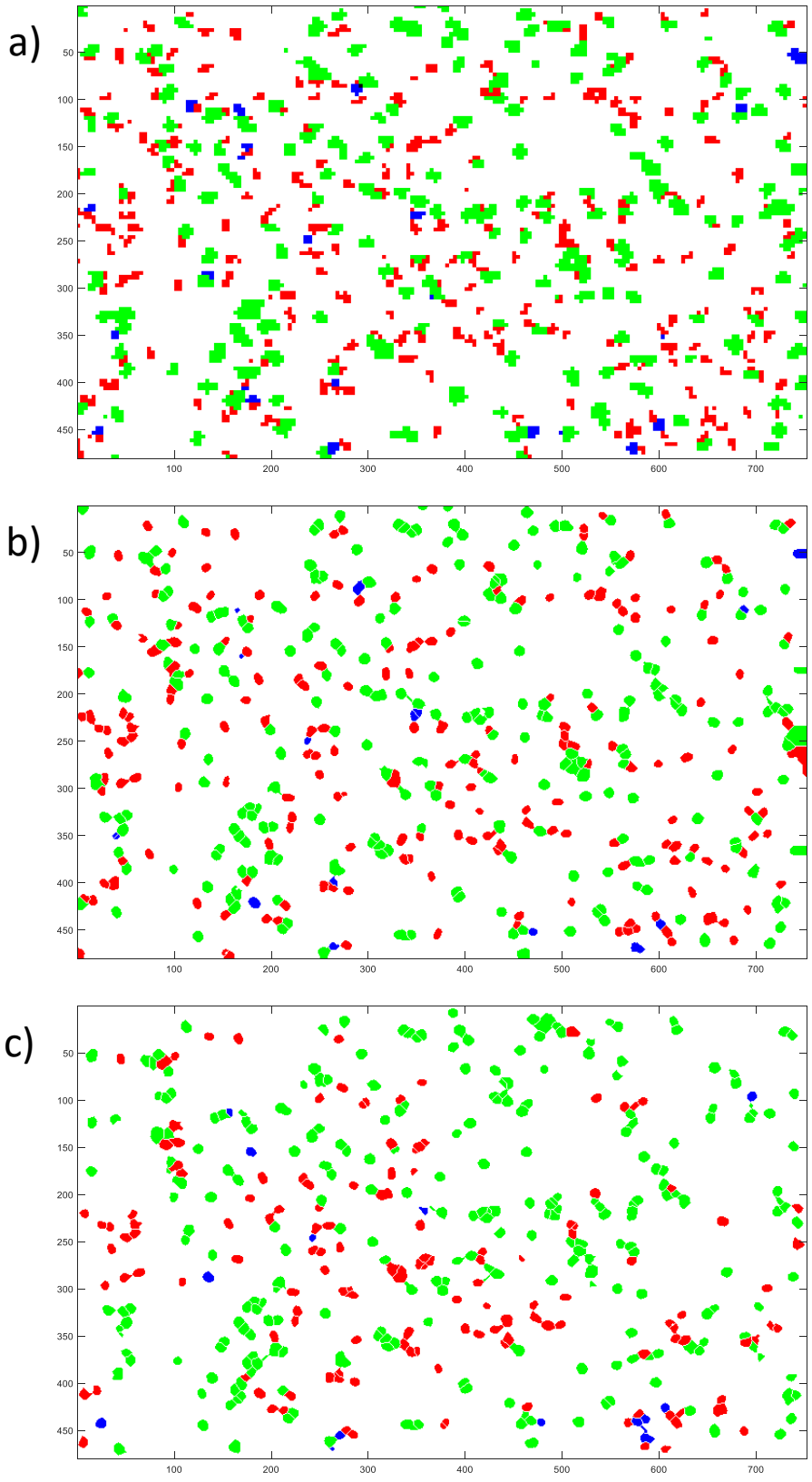

Figure 4.9. Classification results for the same FOV analyzed using a) an RHSC, b) a segmented bright-field image and registered RHSC, and c) targeted Raman analysis.

It is difficult to do a direct comparison between the three techniques due to shifting of the bright-field image that occurred when registering it to the RHSC. This results in misalignment between the original bright-field image used for targeting and the final result both RHSC methods because each covered slightly different FOVs. Additionally, slight changes caused by the interpolation of the registered bright-field cause slightly different results using the segmentation algorithm. However, the three methods produce overall similar results. Table 4.2 compares the results observed from the three methods. The segmentation algorithm identified approximately 500 spore-like objects in both the original and registered bright-field image. The number of viable and gamma irradiated spores using the RHSC analysis was estimated by determining the average pixel size for these spores and dividing that number into the total number of spectra classified as viable or gamma irradiated. The number of PHBA regions were counted manually. The classification counts for the registered RHSC and targeted results were determined directly from the algorithm and are similar to each other overall, however the targeted scan has a slight bias toward classifying a spore as viable.

Table 4.2. Comparison of detection results using three analysis methods

	Total Regions	**# Viable**	**# Gamma**	**# PHBA**	**Blank Spectra**	**Efficiency (Scans/Spore)**
RHSC	N/A	201*	175*	22	17,763 83.8%	N/A
Registered RHSC	497	239	197	16	17,763 83.8%	42.6 (2.3%)
Targeted	513	260	141	15	6,661 81.2%	16 (6.25%)

In the RHSC, 17,763 of the spectra had no C-H stretch feature and 6,661 of the targeted spectra fell below the low threshold for analysis meaning that approximately 80% of the spectra collected for both methods were extraneous. For the RHSC, the amount of this extraneous sampling depends on how densely the spores are placed onto the substrate. For the targeted scan it depends on the acquisition parameters taken at each spore target location. To understand this, a spectral efficiency term was developed. This number is calculated by dividing the total number of spectra collected by the number of spore-like objects identified in the FOV. For this term a lower number is more efficient with an ideal value equaling 1, meaning that each spore can be classified using a single Raman spectrum. Alternatively, the inverse of this value can be viewed as a percentage with 1 being equal to 100% efficiency. As described above, the limitations in stage positioning for the current instrumentation requires an area map to be collected at each target. For the 4×4 settings used for this analysis the efficiency is fixed at 16 or 6.25%. To identify the 497 target regions in this image using the RHSC took 21,204 total spectra resulting in an efficiency of 42.6 or 2.35%. Section 4.4 will explore this issue further by analyzing images with denser and sparser clusters of spores.

4.4 Targeting in Sparse and Dense Regions

As shown above, direct targeting of spores for Raman analysis has the potential to significantly decrease scan time compared to a full RHSC. When preparing samples it is useful to deposit the spores such that the there is a large number within an FOV but not so many that the spores cluster and aggregate. If the spores aggregate then it is possible that some spores will not be able to be analyzed because they are obscured by other spores.

The images analyzed so far were prepared to have a balance between having a larger number of spores to analyze while preventing the spores from aggregating. In this section we will examine scenarios on the two extremes. The first will have a sparse deposition and the second will have a dense deposition.

4.4.1 Sparse Deposition

A sparse deposition has relatively small number of spores dispersed over an area. A sample containing a 50:50 mixture of viable and gamma-irradiated *B. anthracis* Sterne spores was diluted to reduce the spore concentration before being deposited onto an aluminum microscope slide. Figure 4.10 shows an example of a sparse FOV. This bright-field image contains 244 spores in a 209 × 209 μm area. A 418 × 418 pixel RHSC was taken over this area taking 0.5 μm steps. A targeted analysis, following the procedure from Section 4.3, was also performed. Both analyses used a 7 mw 532 nm laser with a 1.5 s integration time. Each spectrum in the RHSC and targeted analysis were processed to remove cosmic rays and background features.

The correlation coefficient was calculated for each spectrum in the RHSC compared to the library spectra for viable and non-viable *B. anthracis* Sterne spores and PHBA. Figure 4.11 shows a color coded classification showing the viable pixels in green, gamma irradiated pixels in red, and PHBA pixels in blue. The RHSC was rescaled to match the size of the bright-field image using a nearest neighbor interpolation. The brightfield image was then registered to the RHSC and the two were overlaid for context to serve as a ground truth. Figure 4.12 shows the classification results using the targeted scan method. The

spectra were classified using the method described in Section 4.3.3 using a high threshold of 0.7 and a low threshold of 0.5.

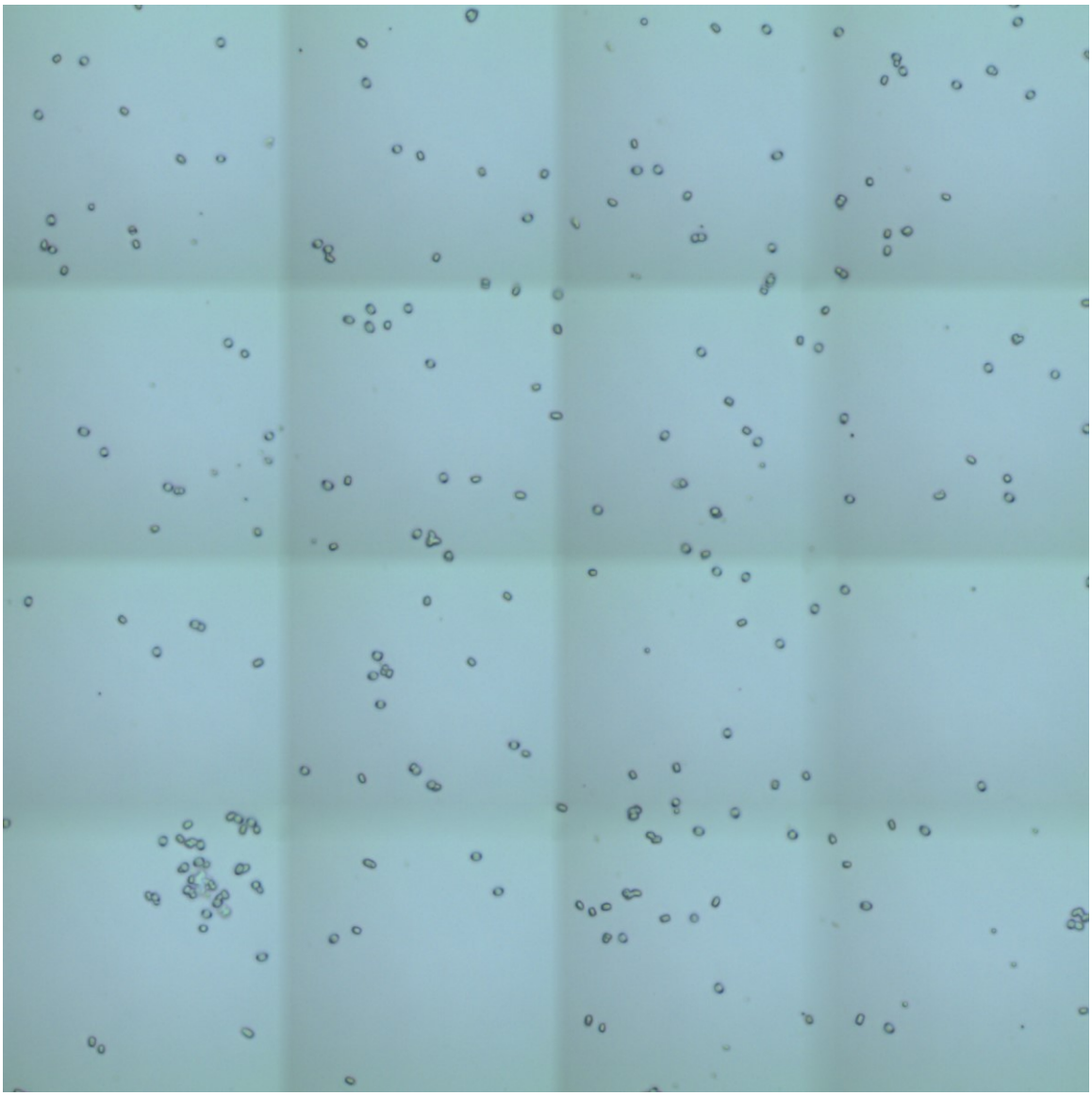

Figure 4.10. Bright-field image of sparsely dispersed sample.

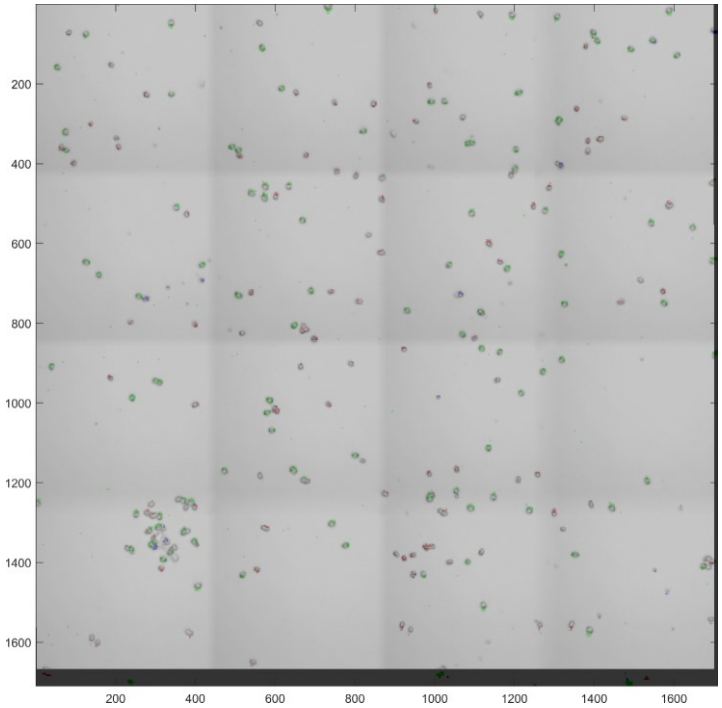

Figure 4.11. Spectral classification of sparse RHSC showing viable (green) and gamma irradiated (red) spores and PHBA (blue).

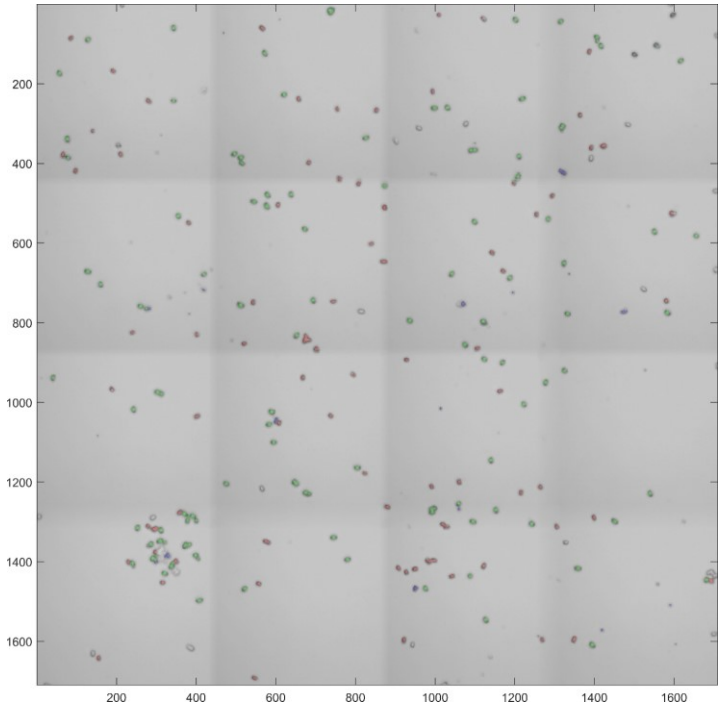

Figure 4.12. Spectral classification of sparse targeted analysis showing viable (green) and gamma irradiated (red) spores and PHBA (blue).

The results obtained collecting a RHSC and the targeted procedure are similar, however the time to collect the required spectra are extremely different. Table 4.3 compares the collection time for the two methods. The RHSC took 174,724 spectra to cover the full FOV. With a 1.5 s integration time this required nearly 73 hours. The targeted scan was able to complete its analysis in less than 2 hours. The low number of spores in the FOV resulted in an efficiency value of 713.2 for the RHSC meaning that it took that many spectra on average to account for each spore-like object identified within the FOV. As described previously, collecting a 4 × 4 at each target location fixes the efficiency of this method at 16. This example highlights that the benefits of this technique are improved when analyzing sparse samples. The targeted scan of the "moderate density" FOV showed in Figure 4.9 gave approximately a 2.7× improvement in efficiency and collection time. The improvement demonstrated on this sparse sample is approximately 44.6×.

Table 4.3. Comparison between the RHSC and targeted scan for the sparse example

	Total Spectra	Spores	Collection Time (s)	Collection Time (HH:MM)	Efficiency
RHSC	174,724	245	262,086	72:48	713.2 (0.14%)
Targeted	3,904	244	6,100	01:42	16 (6.25%)

The spore density is determined on how the sample is prepared. Sparse samples allow for less ambiguous identification due to the lack of neighboring spores which could contribute to the Raman signal if the collection objective is not centered directly on the spore. Sparse samples also allow for easier segmentation. Additionally, Raman

spectroscopy has been demonstrated for the detection of biological aerosols that are continuously collected from the air, concentrated, and deposited onto a surface for interrogation with Raman microscopy [110]. In this type of application, the amount of collected aerosol spore-like objects is typically low and incorporating this type of sparse targeting could potentially be used to improve performance.

4.4.2 Dense Deposition

A dense deposition has a relatively large number of spores dispersed over an area. A sample containing 2% viable *B. anthracis* Sterne spores with and 98% gamma irradiated spores was prepared. The sample was deposited onto an aluminum microscope slide and analyzed near the droplet edge after drying. When a liquid drop dries on a solid surface, capillary flow brings liquid from the center toward the outer edge where it evaporates causing an increased concentration of any suspended particles near the edge. This is known at the "coffee ring effect" [111]. Figure 4.13 shows an example of a densely dispersed FOV containing 1419 spore-like objects in a 92 x 58 μm area. A RHSC cube was collected over this area as well as a targeted analysis following the procedure from Section 4.3. Each spectrum in the RHSC and targeted analysis were processed to remove cosmic rays and background features.

The correlation coefficient was calculated for each spectrum in the RHSC compared to the library spectra for viable and non-viable *B. anthracis* Sterne spores and PHBA. Figure 4.14 shows a color coded classification showing the viable pixels in green, gamma irradiated pixels in red, and PHBA pixels in blue. The RHSC was rescaled to match the size of the bright-field image using a nearest neighbor interpolation. The brightfield image

was then registered to the RHSC and the two were overlaid for context to serve as a ground truth. Figure 4.15 shows the classification results using the targeted scan method. The spectra were classified using the method described in Section 4.3.3 using a high threshold of 0.8 and a low threshold of 0.6. The 2.5 × 2.5 μm scan area are each target area resulted in the interrogation of multiple spores at each target location. If different classes were identified within the same target location, then the location was classified corresponding to the class that had the highest amount of the 16 spectra associated with it. This is not the method that would be used in the final application of locating a single viable spore mixed with a large number of deactivated spores, however it was selected for this example to provide a better visual comparison to the RHSC results.

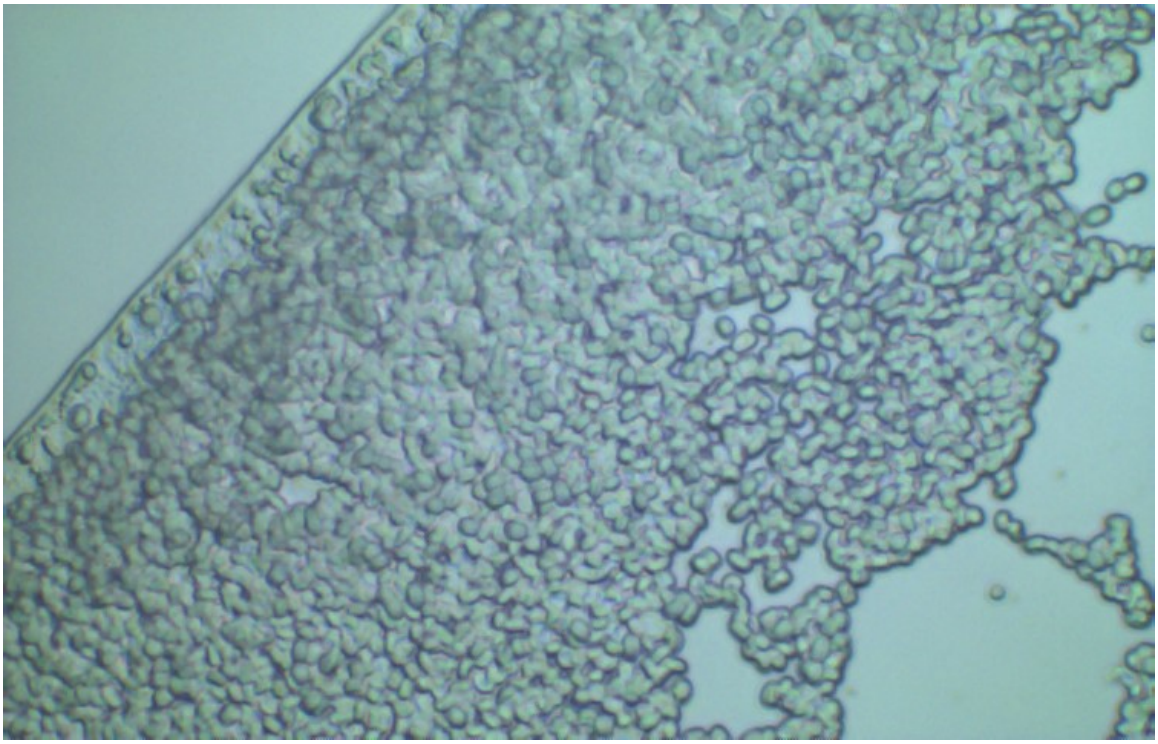

Figure 4.13. Bright-field image of densely dispersed sample

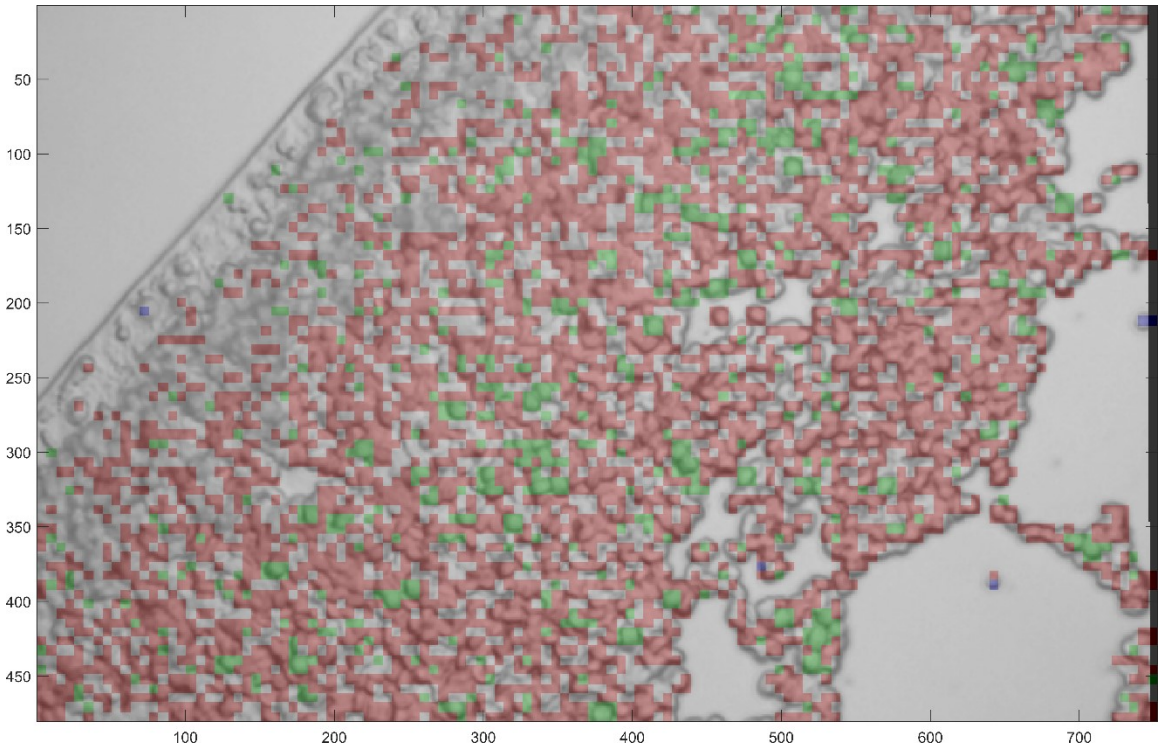

Figure 4.14. Spectral classification of dense RHSC showing viable (green) and gamma irradiated (red) spores and PHBA (blue).

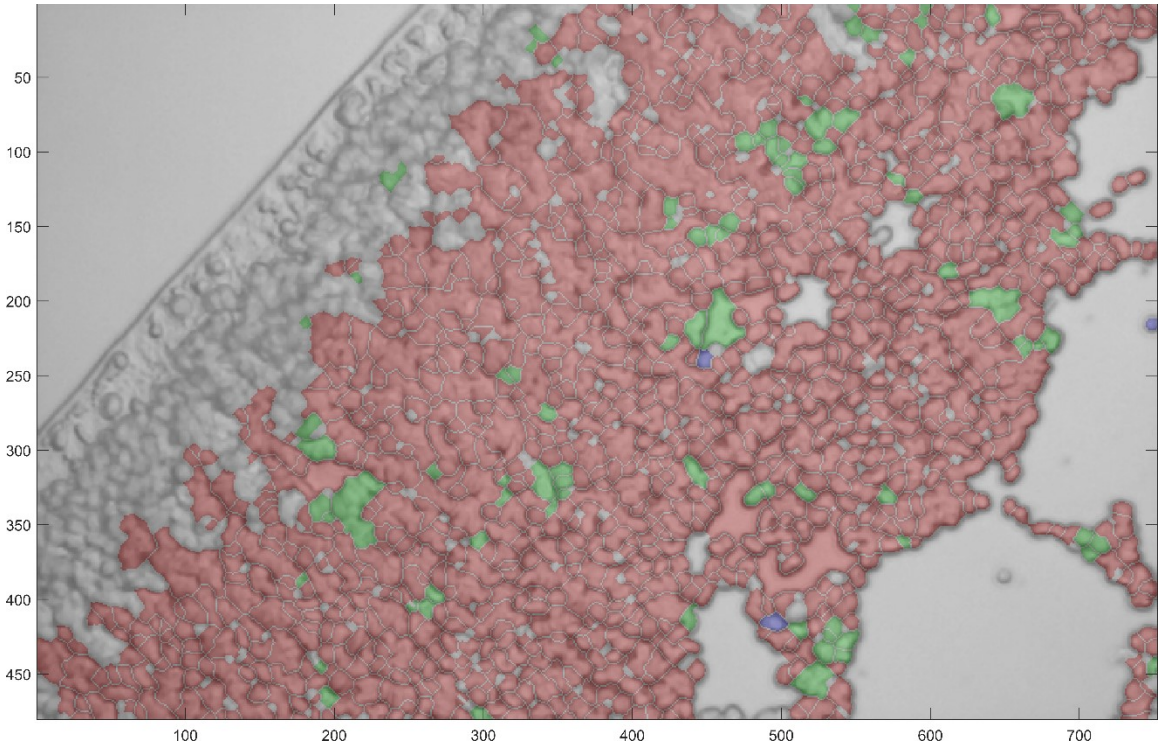

Figure 4.15. Spectral classification of dense targeted analysis showing viable (green) and gamma irradiated (red) spores and PHBA (blue).

The results obtained from the two methods do not match as well for the dense sample as the previous examples. This is due to two main limitations of the targeting method. First, as discussed previously, the linear stages within the microscope system introduce a positioning error as they move from point to point. This is overcome in the less dense samples by collecting a 4 × 4 Raman map covering 2.5 × 2.5 μm around the target location. This area is typically large enough to ensure that the targeted spore is positioned into the scanning area and because the sample is less densely populated it possible to ensure that the target spore is responsible for the majority of spectra collected in the Raman map. This Raman map covers 6.25 μm^2 and an elliptical *Bacillus* spore with axis lengths of 1.43 and 1.15 μm (from Section 2.3) covers approximately 1.29 μm^2. In a dense sample the Raman map around the spore will include spectra from the target spore, but also a large percentage of the spectra will come from spores surrounding the target making it difficult to properly classify the target.

Second, the targeting method relies on the initial segmentation to properly identify spore-like objects. As discussed in Section 2.2.2, higher density images leads to over-segmentation in the interstitial regions between the spores which reduces the overall advantage of the technique. Table 4.4 compares the targeted method to an RHSC taking 0.5 μm steps over the FOV. The times for both methods are based on a 1.5 s integration time. The targeted scan has an additional 1 s added to account for travel time between each target location. The large number of closely packed targets identified in the bright-field image (1,419) resulted in an oversampling of the densest portion of the image with over 2,000 more spectra being collected using the targeted scan compared to simply collecting the RHSC. The collection time for the RHSC is also almost 1.5 hours shorter than the

targeted method. After the bright-field image was registered to the RHSC, the segmentation algorithm identified 123 fewer spore-like targets due to the slightly shifted FOV and the interpolation within the image leading to the calculation of slightly different watershed lines. With this reduced number of spores in the FOV, the efficiency for the RHSC method is 15.8, making it slightly more efficient than the targeting method.

Table 4.4. Comparison between the RHSC and targeted scan for the dense example

	Total Spectra	Spores	Collection Time (s)	Collection Time (HH:MM)	Efficiency
RHSC	20,520	1,296	30,780	08:33	15.8 (6.32%)
Targeted	22,704	1,419	35,475	09:51	16 (6.25%)

This examination of a dense sample highlights the limitations of this technique. To get the advantages of the targeted method spores should sparse enough to allow for proper segmentation and allow for Raman interrogation with minimal interference from neighboring spores. The advantages of the technique increase with more sparse samples, however in should be noted that if samples become too sparse then overall distance traveled by the microscope stages increases which will increase the positioning error.

CHAPTER 5

OPTIMIZED SMART TARGETING OF VIABLE SPORES

5.1 Introduction

The process of using the segmented bright-field image to locate individual spores for Raman interrogation discussed Section 4.3 can significantly reduce the overall scan time compared to a full RHSC, however to sample 1,000,000 spores in this manner to confirm a 10^{-6} sterility assurance level would still require approximately 290 days of constant scanning using a 1.5 s integration time with a 4 × 4 Raman map at each target. To further improve the scan time, it is possible to use the cytometric information described in Chapter 2 to preferentially target spores which have viable characteristics (i.e., longer minor axis lengths). This bright-field classification step is added to the targeted data collection

procedure as shown in Figure 5.1. This type of smart targeting has shown usefulness in forensic applications and leads to a reduction in the time required to analyze the sample by predetermining the location of the spores and interrogating only those locations [112, 113].

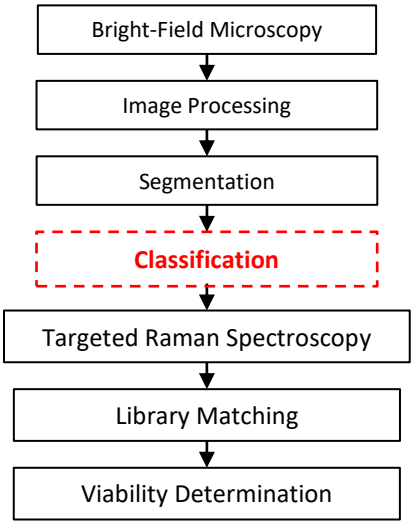

Figure 5.1. Flow chart showing the smart targeting procedure

The size and shape information discussed in Section 2.3 showed a limited ability to discriminate viable from gamma irradiated spores on its own, but the data can be used to preferentially target spores that have a higher likelihood of being viable. The following sections detail a practical demonstration of this smart-targeting technique on a 220 x 220 μm field of view containing approximately 7000 spores from a 1:1000 mixture of viable to gamma irradiated spores, compares the results to an RHSC used as ground truth, and discusses benefits and areas for improvement.

5.2 Sample Information

The bright-field image shown in Figure 5.2 is stitched together from 16 images taken at 100x magnification to cover a FOV of 220 x 220 μm. The image contains approximately 7000 *B. anthracis* Sterne spores at mixture ratio of 1:1000 viable to gamma irradiated spores.

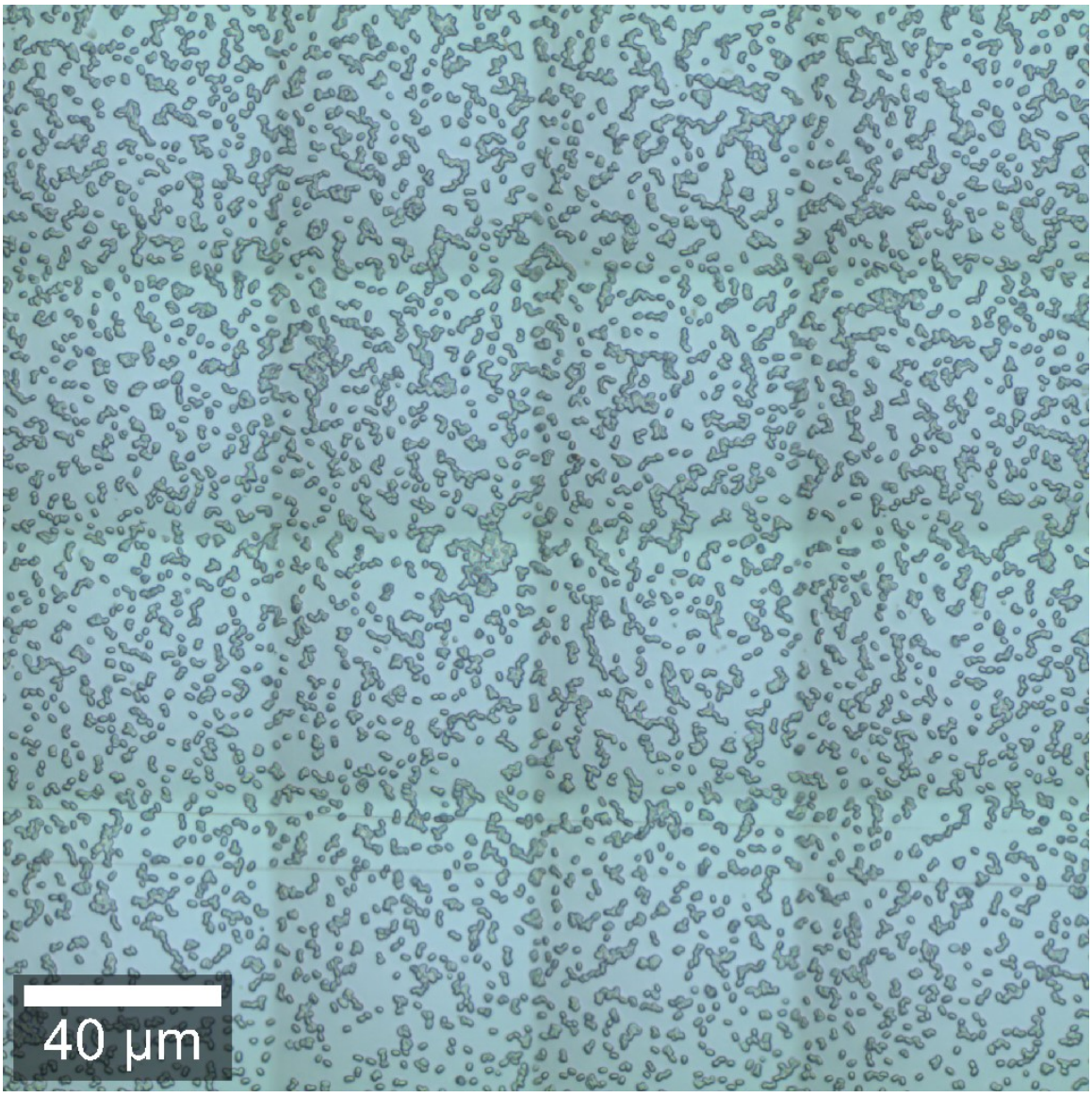

Figure 5.2. Bright-field image showing 220 x 220 um region containing a 1:1000 mixture of viable to gamma irradiated *B. anthracis* Sterne spores.

5.3 Raman Hyperspectral Ground Truth

A RHSC was collected over the region to serve as ground truth to evaluate the performance of the smart-targeting procedure. An area of 205 x 205 μm was measured in 0.5 μm steps to generate a 410 x 410 pixel RHSC. The laser power was set to 7 mW. An integration time of 0.25 s was used in order to keep the overall scan time reasonable. To cover the entire FOV using this integration time took approximately 24 hours. As discussed in Section 3.3.2, the Raman signal recorded using integration times this short are weak. This made library matching using the correlation coefficient (as shown in previous RHSC analyses throughout this thesis) impractical, however single and multi-peak analyses of the spectra allowed for the generation of useful ground truth data.

When analyzing the RHSC of this region, four main spectral constituents were identified (not including background): gamma irradiated spores, viable spores, PHBA, and an unknown compound which was likely cellular debris remaining from sporulation or growth media. Figure 5.3 shows average spectra extracted from the RHSC for these materials. Using the average spectra for these constituents, it was possible to identify specific peaks that could be used to classify individual lower SNR spectra within the RHSC.

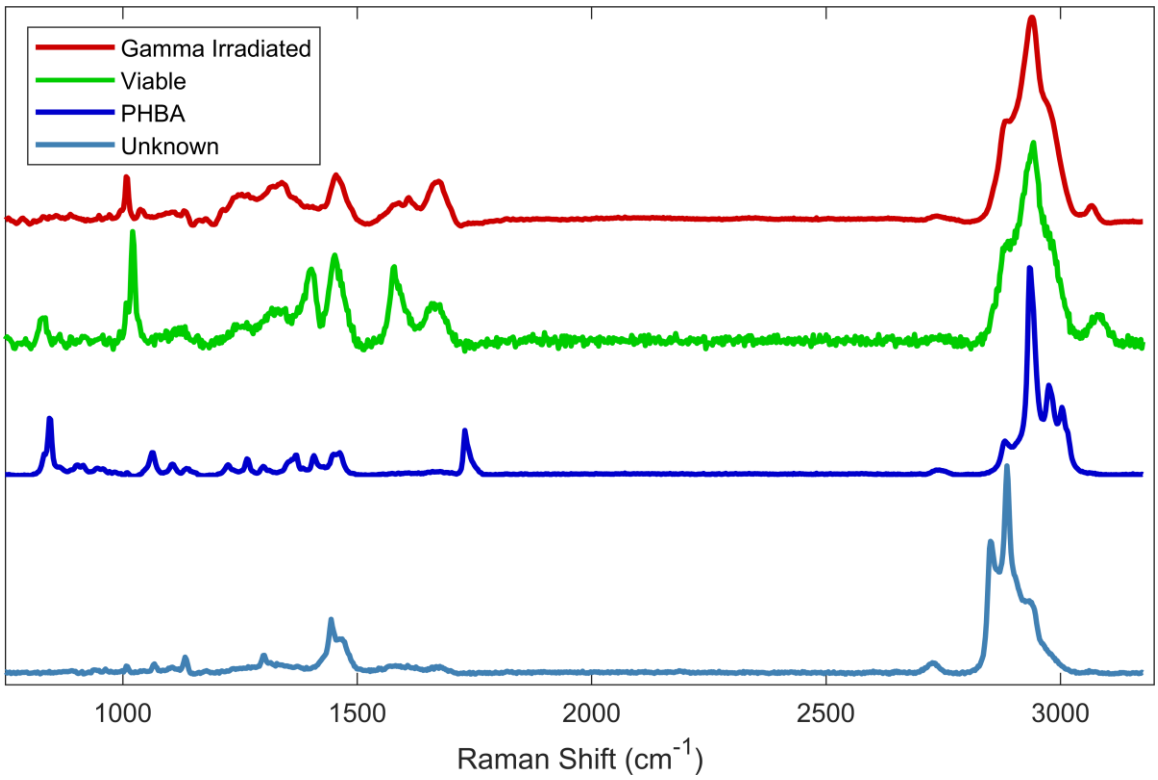

Figure 5.3. Different spectral constituents identified from the ground truth RHSC.

To classify the viable spores, PHBA, and unknown debris, the intensity of single peaks were divided by the maximum signal intensity measured in the blank spectral region from 2165-2401 cm^{-1}. For viable spores, the comparison used the CaDP peak at 1021 cm^{-1}. For PHBA, the 1730 cm^{-1} peak was used. The 1444 and 2886 cm^{-1} peaks of the unknown cellular debris were used for its classification. Additionally, the maximum intensity from 2929-2951 cm^{-1} corresponding to the C-H stretch was ratioed to the blank spectral region.

After these values were calculated, the following process was used for classification:

1. If the CaDP ratio was > 2 and the C-H ratio > 3 then the pixel was classified as viable
2. If the PHBA ratio was > 2 and the C-H ratio > 3 then the pixel was classified as PHBA

3. If the 1444 cm^{-1} debris peak ratio was > 2 and the 2886 cm^{-1} peak was > 20 then the pixel was classified as debris
4. The peaks in the spectral fingerprint region (600-1800 cm^{-1}) for the gamma irradiated spores were weak which made classifying off a single peak challenging so pixels were classified as gamma irradiated if the C-H stretch ratio was > 3 but did not fall into any of the previous three classes.

Figure 5.4 shows the classification results for the RHSC. Table 5.1 summarizes the classification results. Of the 168,000 spectra collected in the RHSC, nearly 80% were classified as background meaning there was no C-H stretch present in the spectra. The majority of the remaining 20% were classified as gamma irradiated spores. The remainder is made up of viable spores (0.02%), PHBA (0.37%), and cellular debris (0.10%). Only 35 spectra were classified as viable compared to the 33,472 classified as gamma irradiated. Figure 5.5 shows the location of the viable classified pixels since finding these spores are the main objective of the smart targeting procedure. The 35 spectra clustered into 12 regions ranging from 1 to 5 pixels in size. Average spectra from each of these 12 clusters are shown in gray in Figure 5.6 and compared to the green library spectrum for viable spores in the fingerprint region from 600-1800 cm^{-1}). All of the spectra show a significant CaDP peak at 1021 cm^{-1} giving confidence that these 12 clusters were correctly identified as viable.

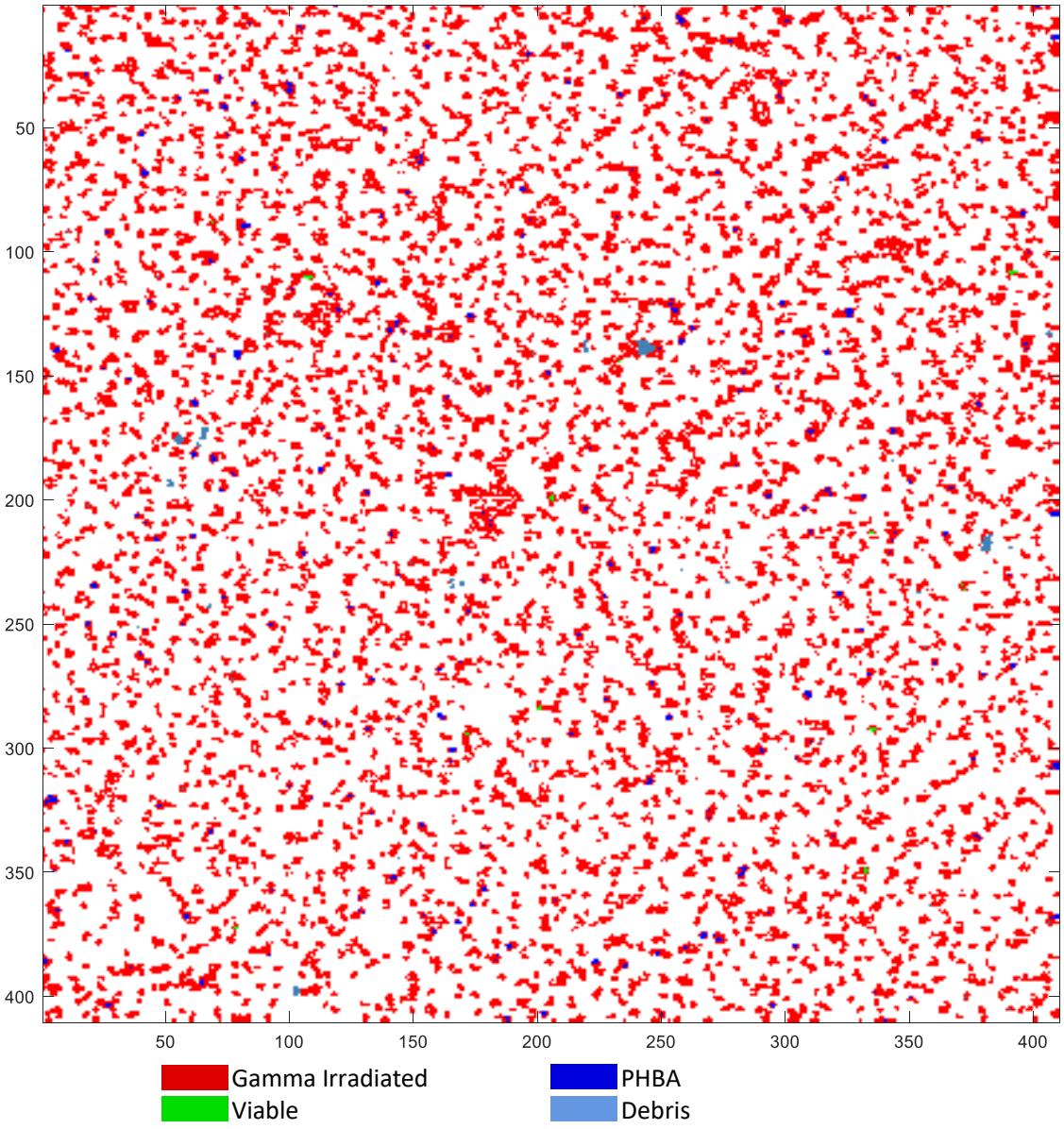

Figure 5.4. Classification results for ground truth RHSC.

Table 5.1. Classification summary for ground truth RHSC

Class	Number of Spectra	% of FOV
Background	133790	79.59%
Gamma	33472	19.91%
Viable	35	0.02%
PHBA	629	0.37%
Debris	174	0.10%

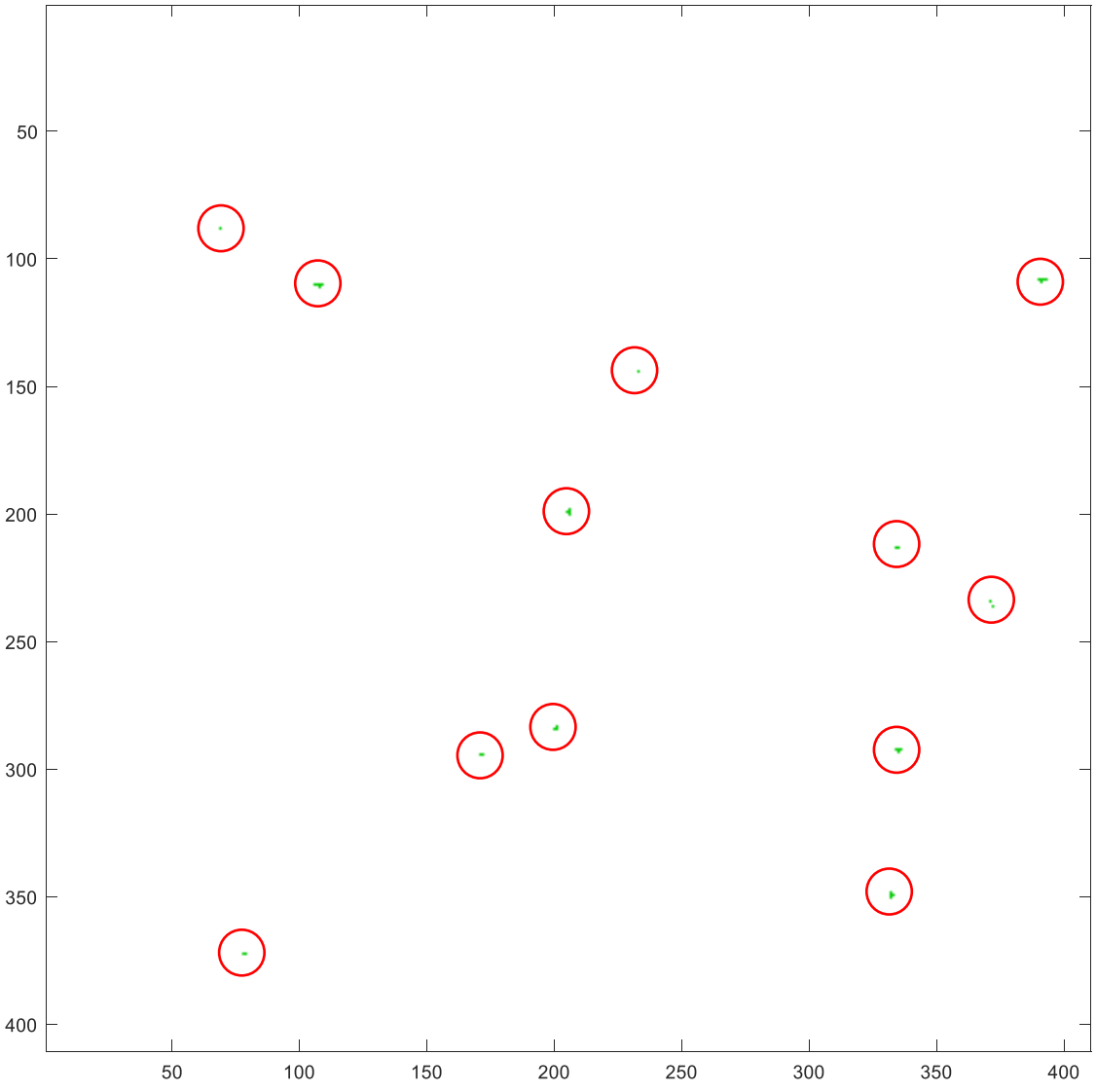

Figure 5.5. Location of viable spores from ground truth RHSC (shown as green pixels which have been circled for clarity)

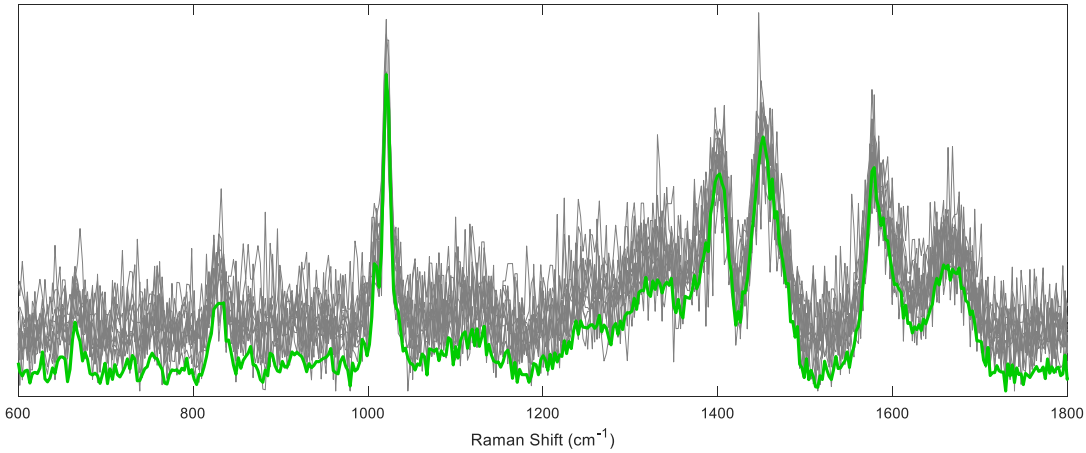

Figure 5.6. Averaged Raman spectra from each of the 12 clusters classified as viable spores (gray) compared against the viable spore library spectrum (green).

5.4 Smart Targeting Criteria

Section 2.3 showed that a certain level of discrimination between viable and gamma irradiated spores could be obtained with the size and shape characteristics determined using the bright-field image of a spore. In general, it was shown that the viable spores had a larger minor axis length and larger area than the gamma irradiated spores. Using the histograms shown in Figure 2.9, thresholds were created to set five priority levels based on the following criteria:

- Priority 1 (most likely to be a viable spore): Minor axis length greater than 0.88 μm and less than 1.46 μm AND area greater than 1.06 μm^2
- Priority 2: Minor axis length less than 0.88 μm AND area greater than 1.06 μm^2
- Priority 3: Minor axis length greater than 0.88 μm and less than 1.46 μm AND area less than 1.06 μm^2
- Priority 4: Minor axis length less than 0.88 μm AND area less than 1.06 μm^2

- Priority 5 (least likely to be a viable spore): Minor axis length greater than 1.46 μm

The bright-field image shown in Figure 5.2 was segmented using a 15 pixel disk shaped structuring element, a 3 × 3 spatial filter, and an intensity threshold of 15. Regions were required to have an area from 22 to 2500 pixels. Any regions whose centroids were closer than 0.65 μm apart were combined into a single target. This resulted in 6788 spore-like targets identified in the FOV. Table 5.2 shows how many regions were classified into the five priority levels. Approximately 25% of the spores returned as Priority 1 for further analysis.

Table 5.2. Number of spore-like regions in each priority level

	Identified Regions	Percentage of Total
Priority 1	1753	25.8%
Priority 2	123	1.8%
Priority 3	1261	18.6%
Priority 4	3384	49.9%
Priority 5	267	3.9%
Total	6778	

5.5 Priority Scan Results

A targeted Raman analysis was performed on all the regions identified as Priority 1. Each region was classified as either viable, gamma irradiated or PHBA using the method described in Section 4.3.3 with a high threshold of 0.8 and a low threshold of 0.6. The results are shown in Figure 5.7 with all the viable detections being circled in green or purple for clarity. The green circles correspond to viable spores that were identified in both this Priority 1 scan and in the RHSC analysis. Overall, 10 of the 12 viable spores identified in

the RHSC were also identified in the priority scan method. In addition to those 10, one additional viable spore (circled in purple) was identified using the smart targeting method that was not properly classified using the RHSC analysis.

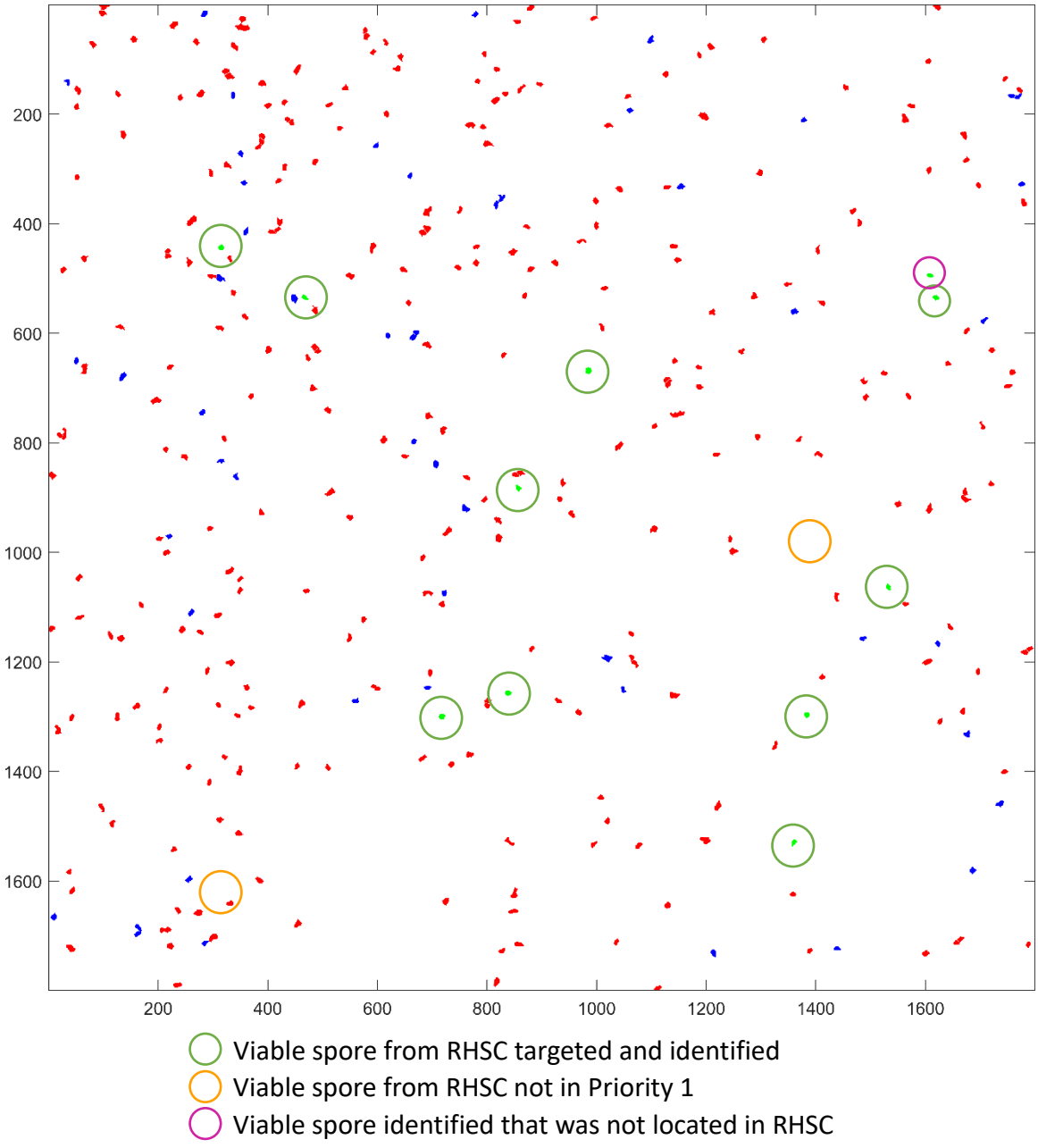

Figure 5.7. Classification results from Priority 1 targets.

Two viable spores identified in the RHSC analysis were not identified in the Priority 1 scan. The approximate locations of these missed identifications are marked with the orange circles. A detailed view of the missed spore located in the lower left-hand side of Figure 5.7 in shown in Figure 5.8. The figure shows the same FOV of the spore in the bright-field image, segmentation image, and RHSC classification image with the specific spore being marked with an arrow in each. This spore was properly segmented, however the minor axis length of 0.89 and an area of 0.84 categorized it as Priority 4 and it was not scanned. The edges of the spore are noticeably more blurred then the spores around it meaning that the spore may oriented in a way that caused it to be slightly out of focus when the bright-field image was collected.

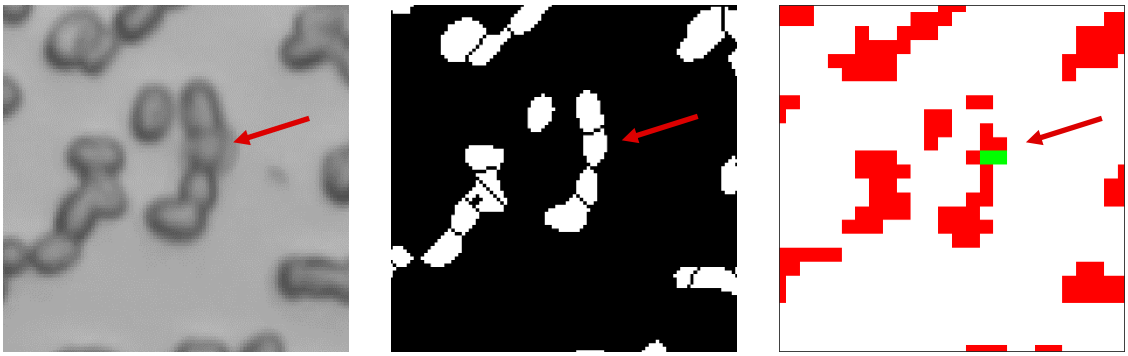

Figure 5.8. Detailed view of missed detection 1 showing the bright-field image (left), segmented regions (center), and RHSC classification (right).

Figure 5.9 shows a similar detailed view of the missed spore located on the right-hand side of Figure 5.7. In this case, the spore was not segmented at all and therefore the size parameters could not be measured nor could the spore be targeted for Raman analysis. Similar to the previous missed spore, the edges of the spore appear blurred implying that the spore is oriented in a way that placed it outside the focal plane of the

microscope objective. However, in this instance the pre-processing performed by the segmentation algorithm (spatial filtering and background removal) created a discontinuity on the watershed line that prevented the spore from being demarcated as its own region and was instead considered background.

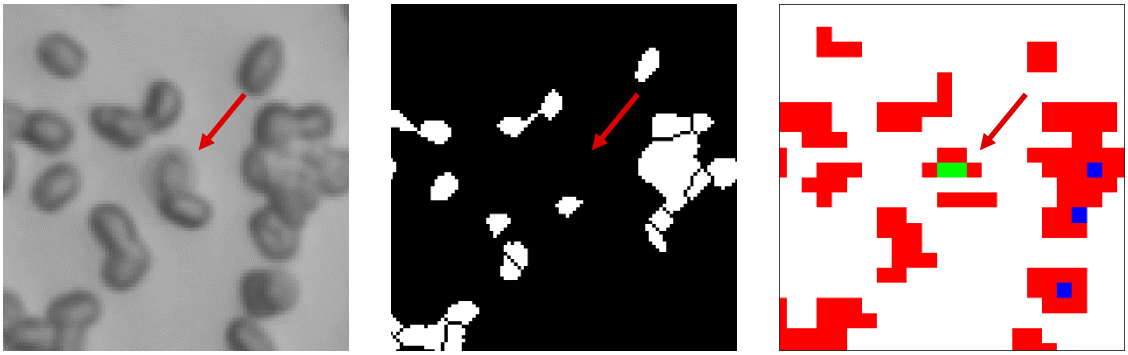

Figure 5.9. Detailed view of missed detection 2 showing the bright-field image (left), segmented regions (center), and RHSC classification (right).

As mentioned above, the targeted analysis did identify a viable spore that was not identified in the RHSC analysis. A detailed view of this region is shown in Figure 5.10a with the specific spore marked with the arrow. Figure 5.10b shows the classification results from the RHSC which had six pixels whose spectra exhibited a C-H stretch feature, but not the 1021 cm^{-1} CaDP peak to be classified as viable. Figure 5.10d shows the average of these 6 spectra in purple with the individual spectra in gray behind it. The average spectrum closely matches the gamma irradiated library shown at the top in red.

Figure 5.10c shows the intensity of the CaDP peak over the 4 × 4 scan area. The two scans on the lower right hand side are significantly stronger than the other 14 spectra. These two spectra closely match the viable library (shown in green in Figure 5.10d) with

both having correlation coefficients of 0.85. The average of these viable spectra are shown in yellow with the individual spectra in gray behind.

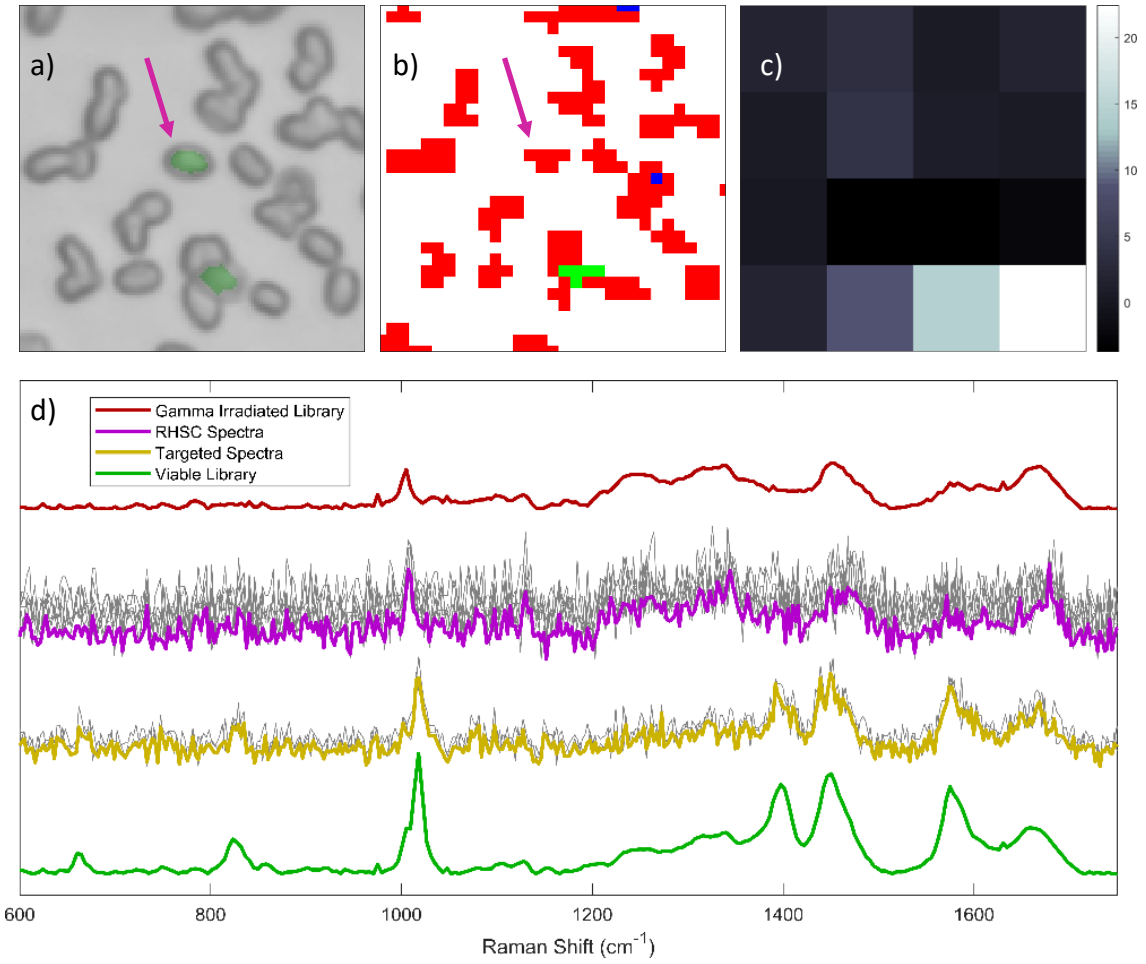

Figure 5.10. Detailed view showing the bright-field image (a) and RHSC classification (b) of the viable spore identified using the smart targeting analysis, but not in the RHSC. c) Intensity of the CaDP peak at 1021 cm^{-1} for the 4×4 Raman map collected at the target location. d) Raman spectra from the identified cluster of the RHSC (purple) compared to the two spectra from the targeted scan identified as viable (yellow). Library spectra for gamma irradiated (red) and viable (green) spores are shown for reference.

There are two possible explanations for this discrepancy. The first is that the short (0.5 s) integration time in the RHSC reduced the SNR of the collected spectra to a point where a viable spore was misclassified as gamma irradiated. However this explanation seems unlikely. Figure 5.6 showed that the CaDP peak was easily discernable using this

integration time for other viable spores. Additionally, the weaker 1005 cm^{-1} peak is present in the RHSC implying that there is enough Raman signal being collected. The spore is not in contact with any other spores which makes it possible to unambiguously associate six specific RHSC spectra with the spore. The correlation coefficient of the average of these spectra compared to the gamma irradiated library is 0.78. When compared to the viable library the correlation coefficient is 0.54.

The second, and more likely, explanation is that misalignment in the stage positioning caused a portion of the nearby viable cell to be inadvertently collected. The edges of the two viable classified (green) spores in Figure 5.10a are approximately 3.4 μm apart in the y-axis. Looking at the peak intensity of the Raman map in Figure 5.10c shows that the viable spore was in the lower right-hand portion of the FOV. The stage likely positioned the center of the Raman map FOV slightly lower than the target spore which resulted in spectra being collected from this lower viable spore. Since the detection results prioritize all viable detection results that caused this spore to be misclassified as viable. However since the goal in this application is to find whether or not there are *any* viable spores present in the overall sample, misclassifying a single spore as viable based on a nearby viable spore is acceptable. The larger concern is the overall precision and reproducibility of the positioning stages to ensure that the target spore falls into the scan FOV.

CHAPTER 6

CONCLUSION

In this thesis, we detailed the development of a novel optical method and demonstrated an approach using image analysis and Raman microscopy to rapidly determine the viability of *Bacillus* spores.

To do this we developed a procedure that was able to segment bright-field images of spores with an accuracy of 97.4% in the test images. Size and shape information was extracted from these segmented regions from populations of viable and gamma-irradiated spores which showed differences that could be used to perform a level of classification based on the bright-field image alone. Using just the measured minor axis length it was possible to classify 67% of the spores with an 18% misclassification rate.

Raman microscopy was then studied as an additional analysis technique to improve on the classification rate. Raman microscopy was capable of discriminating viable spore

from spores inactivated using both gamma irradiation and autoclaving for *B. athracis* Sterne, *B. atrophaeus*, *B. megaterium*, and *B. thuringiensis kurstaki*. Spectra were taken from spore biomarkers which determined that the spectral changes between the viable and inactivated spores were caused by changes in the CaDP concentration within the spore's core.

Three different Raman methods were demonstrated that allowed for the discrimination of viable and inactivated spores mixed within the same FOV. For the first, an RHSC was collected over the area and each pixel location could be classified either by comparing to a library spectrum or by looking for specific peaks. The second method used the same RHSC but also had the bright-field image registered with the RHSC. The bright-field image was then segmented with specific pixels within the bright-field being mapped onto the RHSC. This allowed for a weighted spectrum to be created for each spore to improve the SNR and improve classification. However, both of these methods use the entire RHSC, which is slow to collect over large areas. Additionally, the method in which the spores are deposited onto the microscope slide for analysis caused for a large percentage of the analysis time to be wasted on regions of the sample where no spores were present.

To overcome this limitation, the third method was demonstrated. This method used the segmented bright-field image to locate the centroid of each spore and then direct the microscope objective to that location for analysis. The current methodology to confirm inactivation requires a sampling of spores to be placed into growth media and monitored for 14 days to confirm a lack of germination. In order for this technique to a usable orthogonal method, it must be able to assess 1,000,000 spores in order to reach a SAL of 10^{-6}. To improve the speed in which viable spores are located, a practical demonstration

was performed using a smart-targeting approach which incorporated the size and shape information from the segmented bright-field image to preferentially target spores that are more likely to be viable. In the demonstration a 1:1000 mixture of viable to gamma irradiated spores was prepared. The FOV contained 6778 total spores, of which 12 were viable. The smart-targeting procedure identified 1753 spores (25.8% of the total) as potentially viable spores. After the targeted Raman analysis it was determined that this subset contained 10 (83.3%) of the viable spores. The bright-field image of two missed spores had focus problems which prevented one from being segmented and may have affected the size characteristics of the other.

The main issue observed with this technique was positioning precision of the linear stages within the microscope. The microscope uses two stages; one uses a stepper stage that covers a relatively large scanning range and the other is a high precision piezo stage with small scanning range. In order to position with the accuracy and total range required to target the spores both stages are used, however repetition accuracy and hysteresis in the stages causes the positioning to drift over use. To overcome this issue for our demonstration, a 16 spectrum Raman map was collected over a 2.5 × 2.5 μm in order to overfill the target spore. This was done to ensure that even if the stage became misaligned, the some portion of the target spore should still be located within the scan area. This limitation will need to be overcome in order to make this a practical analysis technique. Improving on the stage precision will allow for the reduction in the number of spectra collected per spore. Figure 6.1 shows an overlay of different sizes of Raman map and how they compare in size to the spore itself. Reducing this value also improves the efficiency factor which for all our demonstrations was fixed at a value of 16 (6.25%). Reducing the

number of spectra collected in the Raman map has a significant impact in the overall collection time. Table 6.1 shows the time required to collect one million spectra using different collection parameters. This would be the number of spores required to confirm an SAL of 10^{-6}. The analysis time includes both the integration time and 1 s to account for travel time between spores. Using the current settings would require 290 days of analysis. Reducing the integration time has a near linear effect on the overall analysis time. Using an integration time of 0.5 s, which was shown to provide a reasonable SNR in Section 3.3.2, has a significant improvement, but the overall analysis time is still 93 days.

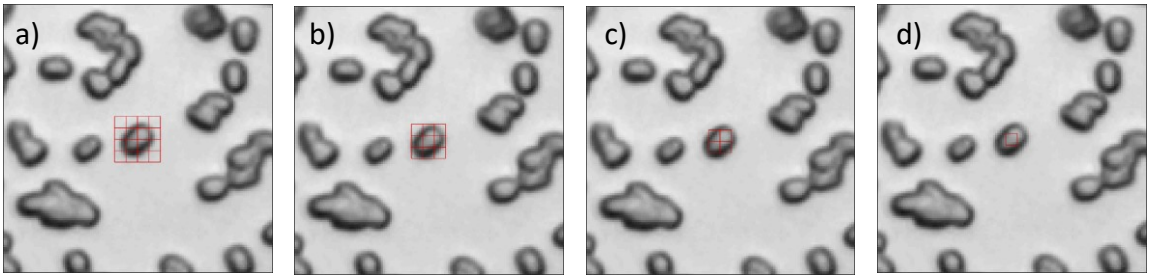

Figure 6.1. Example spore showing the size of a a) 4×4, b) 3×3, and c) 2×2 Raman maps and d) single point spectrum which could be used for interrogation.

The current method to confirm viability takes 14 days. The only way that Raman analysis could measure one million spores in that time frame with reasonable SNR is to go to a single scan measurement. Using a single scan and 1 s integration allows for the measurement to be completed in 12 days.

Table 6.1. Time to analyze one million spores using different acquisition parameters.

Integration Time (s)	Raman Map Size	Time to Analyze 1,000,000 Spores (Days)
1.5	4×4	289.4
1	4×4	185.2
0.5	4×4	92.6
1.5	3×3	156.3
1	3×3	104.2
0.5	3×3	52.1
1.5	2×2	69.4
1	2×2	46.3
0.5	2×2	23.1
1.5	Single Spectrum	17.4
1	Single Spectrum	11.6
0.5	Single Spectrum	5.8

Given these results it is unlikely this method will replace the traditional procedure of confirming lack of growth from an inactivated spore. Currently available linear stages do not have the combination or overall travel range, precision, and travel speed to make the analysis of enough spores to confirm the requires 10^{-6} SAL practical. However, the smart targeting procedure demonstrated the ability to more rapidly locate a small amount of viable spores mixed with inactivated spores which could identify a batch of spores that were not fully inactivated more rapidly than the traditional approach.

6.1 Future Work

Future development of this technique requires positioning stages that have a combination of a relatively large overall travel range (10+ mm) with a small repetition accuracy (<10 nm). This combination is required to interrogate the large number of spores required to confirm the 10^{-6} SAL without accumulating a large enough positioning error to

cause the Raman laser to miss target spores. Advancements in stage positioning will be monitored and incorporated into the configuration as stage technology improves.

Currently, the targeting and spectral library analysis are performed offline from the microscope system. This process involves collecting the bright-field image on one computer system, transferring it to another for targeting in Matlab, copying the target list back to the microscope for Raman collection, and then copying the Raman spectra back to the other computer for spectral processing. The processes performed on these two computer systems will be combined so that the data collection and processing are performed on the same computer. Software applications will be developed to automate the process to minimize the amount of human intervention required and reduce the overall acquisition and analysis time.

Finally, this work demonstrated the ability for Raman microscopy to discriminate viable *B. athracis* Sterne, *B. atrophaeus*, *B. megaterium*, and *B. thuringiensis kurstaki* spores from those that had been deactivated using gamma irradiation and autoclaving. These same spores will be inactivated using two different methods of chemical inactivation (bleach and aldehyde) and one additional radiative method (short wavelength ultraviolet [100-280 nm]). Raman spectra will be collected from the four spore species with all deactivation methods. The spectra will be analyzed to determine whether Raman microscopy can be used to differentiate viable and non-viable for all these deactivation methods. Additional analysis will be performed comparing the spectra collected using the different inactivation methods to better understand the chemical and physical changes that the spores undergo when deactivated.

APPENDIX A

OTHER WORK

The following study of acetylcholinesterase levels in whole sheep's blood using Raman spectroscopy was completed prior to the previously discussed study of *Bacillus* spores. It was presented at the 2014 SPIE Sensing Technology + Applications conference in Baltimore, Maryland. The work in this Appendix was originally published in the proceedings of that conference:

Phillip G. Wilcox, Jin U. Kang, "Raman spectroscopic analysis of whole blood acetylcholinesterase," Proc. SPIE 9112, Sensing Technologies for Global Health, Military Medicine, and Environmental Monitoring IV, 91120V (5 June 2014); doi: 10.1117/12.2052701

A.1 Abstract

Raman spectra were taken from whole sheep's blood with varying levels of acetylcholinesterase (AChE) inhibition using 229 and 532 nm laser excitation wavelengths. AChE levels were inhibited using the organophosphates malathion, paraoxon-ethyl, and octamethyldiphosphoramide and confirmed using the Ellman method. This AChE activity level was investigated with the Raman spectra and analyzed using a partial least squares calibration and cross validation to determine if the AChE activity could be predicted from the Raman spectrum. Correlation scores of 0.78 and 0.26 between the measured and predicted AChE activity were observed using 229 and 532 nm excitation, respectively. An estimated limit of detection was found to be approximately 0.01 ΔA/min.

A.2 Introduction

Acetylcholinesterase (AChE) is an enzyme used to break down the neurotransmitter acetylcholine. Exposure to organophosphate (OP) nerve agents and insecticides can inhibit AChE levels which can lead to a range of physiological responses including restlessness and agitation to seizures, coma, and eventually death [114]. There are currently two main methods used to measure AChE activity – the Ellman assay and the Michel assay. Both methods involve drawing a blood sample from a patient, adding reagents, and observing a chemical reaction over several minutes. The Ellman assay (or modified versions of it) measures the change in optical absorbance at a fixed wavelength and the Michel method measures the change in pH [115, 116].

A drop in AChE activity levels can indicate OP exposure even before symptoms are present. A quick test without any consumables would allow for more frequent monitoring of AChE activity and could reduce the time between exposure and beginning treatment. In this effort, we examined the ability to use ultraviolet (UV) and visible Raman spectroscopy as a rapid and reagentless method to measure AChE activity in whole blood. Raman scattering has been used to measure other constituents of whole blood such as glucose, cholesterol, and hemoglobin [117, 118], but to the best of our knowledge no one has tried to determine AChE activity levels. Raman spectroscopy can be scaled to interrogate very small volumes of liquid which would reduce amount of blood needed down to a finger prick instead of a full blood draw.

A.3 Experimental Setup

To determine whether Raman spectroscopy can be used to measure AChE activity, Raman spectra were taken on heperinized whole sheep's blood (Hemostat Laboratories, Dixon, CA) using various excitation wavelengths. All blood samples arrived the day after it was drawn from the animal. Blood was stored at 5 ^{o}C between arrival and used less than 11 days later. AChE levels were inhibited using the organophosphates paraoxon-ethyl (CAS# 311-45-5), malathion (CAS# 121-65-5), and octamethyldiphosphoramide (OMPA – CAS# 152-16-9). The paraoxon-ethyl and malathion were commercially available from Sigma-Aldrich (St. Louis, MO) and the OMPA was acquired through a custom synthesis from Hestia Laboratories (New Berlin, WI). An Ellman assay (described in section 2.3) was run simultaneously with the UV and visible Raman measurements to correlate the spectra to a known AChE activity level.

A.3.1 Blood Sample Preparation and Measurements

At the beginning of each sequence of measurements, the heparinized whole sheep's blood was added to three containers. 4 mL was placed in a glass vial for the 532 nm Raman measurements and organophosphate contamination, 0.5 mL was placed in a small 25 mm wide open air dish for 229 nm Raman measurements, and 5 µL was added to a 10mm square polystyrene UV-Vis cuvette for Ellman measurements. These measurements were run simultaneously. After these measurements were completed, 0.2 µL of one of the OP compounds was added to the 4 mL glass vial and slowly inverted 10 times to ensure thorough mixing and placed in an ice bath for 5 minutes. After 5 minutes, 0.5 mL of the mixture was taken for 229 nm Raman measurements, 0.5 µL was taken for the Ellman assay, and the remaining ~3.5 mL was taken for 532 nm Raman measurements – which were run simultaneously. Afterwards, another 0.2 µL of OP compound was added to the remaining ~3.5 mL vial and the sequence was repeated until the AChE level was fully inhibited.

A.3.2 Raman Instrumentation

The 229 nm measurements were collected using a Princeton Instruments Acton SP2500 Spectrometer and Pixas 2K camera with approximately 8 cm^{-1} resolution. The 229 nm excitation came from a Coherent Sabre FreD continuous wave (CW) frequency doubled argon ion laser which delivered approximately 5 mW at the sample. All samples were measured in an open air plastic dish approximately 25 mm in diameter. A magnetic stir bar was used to minimize damage to the sample caused by the UV laser. The 532 nm

measurements were collected using high resolution echelle spectrograph from EIC Laboratories with Andor iDus 420A-OE CCD camera with approximately 1 cm^{-1} resolution. The 532 nm excitation light came from an Oxxius 532-300-COL-PP CW frequency doubled single longitudinal mode Nd:YAG laser. 532 nm excitation and collection was performed through an EIC RamanProbe fiber optic probe which delivered approximately 150 mW to the sample. All blood samples were measured through a 4 mL glass vial.

A.3.3 Ellman Assay

AChE levels were measured using the Ellman assay [115]. Prior to the measurements 2 reagents were made. The first was a 10.6 mM solution of 5,5'-dithiobis(2-nitrobenzoic acid) (DTNB – CAS# 69-78-3) in phosphate buffer solution (PBS). This DTNB solution is also known as Ellman's reagent. The second reagent was a 76.3 mM solution of acetylthiocholine iodide (ATCI – CAS# 1866-15-5). The PBS used for these measurements was at 1.0 M and 7.4 pH (25 ^{o}C). All reagents were stored at 5 ^{o}C and were used within 30 days.

To perform these measurements, 3 mL of PBS was placed in a 10x10 mm polystyrene cuvette. The cuvette was placed into a Thermo Evolution 60 UV-Visible spectrometer to take a reference background spectrum. Then 5 μL of whole blood, 25 μL of DTNB solution, and 20 μL of ATCI solution were added to the PBS. The cuvette was then inverted approximately 10 times and returned to the spectrometer. The optical absorbance at 410 nm was monitored for 5 minutes. A linear fit was used to determine the change in optical absorbance over time (ΔA/min). This change in absorbance directly corresponds to

enzyme activity (µmol/L/min) through the factor of 13.6 $mM^{-1} \cdot cm^{-1}$. Throughout the remainder of the paper all AChE activity values are given in ΔA/min. For reference, uninhibited blood ΔA/min varied from 0.17-0.26 ΔA/min with fully inhibited blood getting as low as 0.00087 ΔA/min.

A.4 Data

Raman spectra of the uninhibited blood were taken at 4 different excitation wavelengths ranging from the visible to near-infrared at the beginning of this effort. Figure shows a representative spectrum from each wavelength along with the integration time. The 785 nm excitation resulted in a large fluorescence signal which overwhelmed the Raman signal. Raman scattering has a relationship proportional to λ^{-4} which can be observed as the required integration time greatly reduced from 300 s to 10 s as the excitation wavelength shortened from 785 nm to 229 nm.

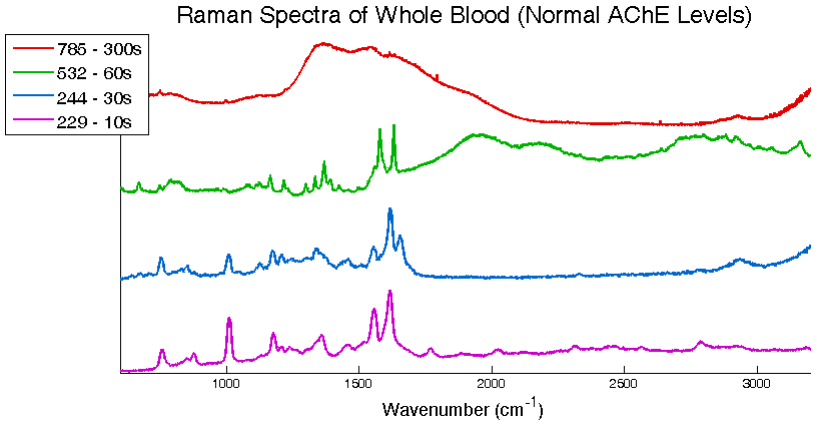

Figure A.1. Raman spectra for uninhibited whole blood using 785, 532, 244, and 229 nm excitation with integration times ranging from 10-300 seconds.

Based on our test configuration, only one UV wavelength could be selected for further AChE measurements therefore 229 nm was selected along with 532 nm for further analysis. The integration time of 60 s for 532 nm and 10 s for 229 nm were kept constant throughout the study. Five (5) spectra were collected at 532 nm and ten (10) spectra were collected at 229 nm for each AChE concentration. Figure A.2 shows the average spectrum for each AChE concentration for 532 nm (left) and 229 nm (right).

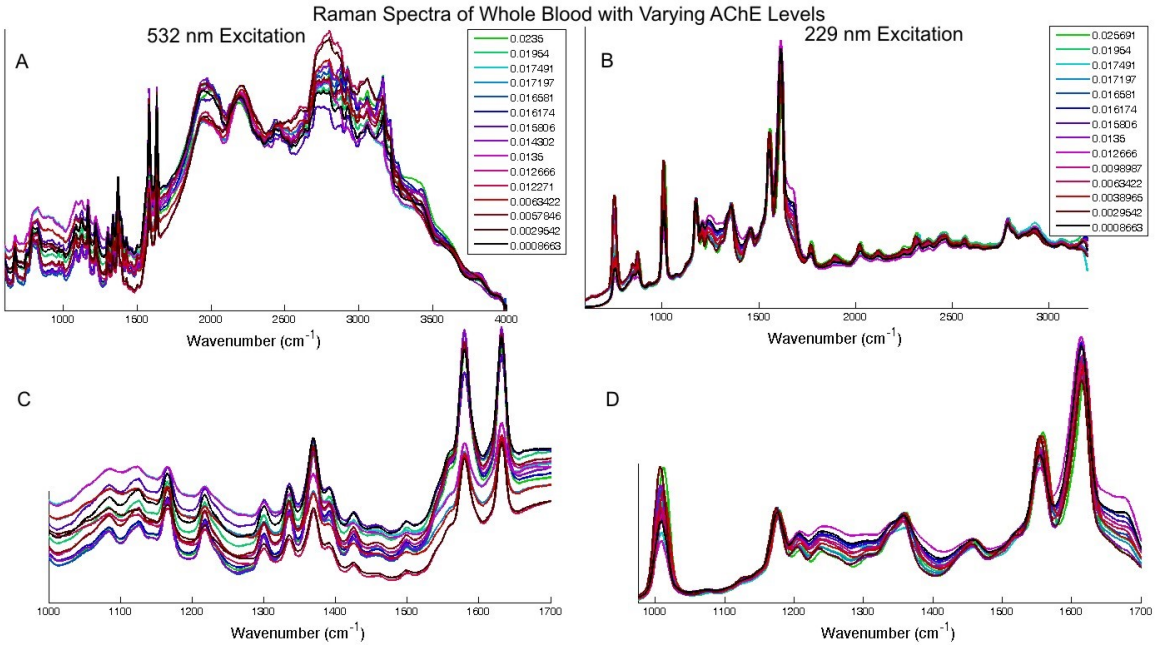

Figure A.2. Average Raman spectrum for each measured AChE concentration using excitation wavelengths of (A) 532 nm and (B) 229 nm. Expanded views from ~1000-1700 cm^{-1} are shown for (C) 532 nm excitation and (D) 229 cm^{-1} excitation. Concentration values are listed in the legend and expressed in ΔA/min acquired using the Ellman assay.

A.5 Analysis

A.5.1 Data Pretreatment

Some of the 229 nm spectra had cosmic rays which were removed using a five point median filter. A seven point mean filter was then used to smooth the data. The 532 did not have cosmic rays and was not median filtered. Because the 532 nm spectra were taken on a higher resolution instrument a wider mean filter of 23 points was used to smooth the data. All spectra were normalized to a common area.

A.5.2 Partial Least Squares Calibration

All spectra were individually analyzed using PLS calibration. This technique is detailed by Haaland and Thomas [119]. The PLS calibration algorithm combines the Raman spectra and the measured Ellman values to generate two outputs – the PLS loading vectors and a relating score vector. The PLS loading vectors are a series of *i* component spectra that can be linearly combined to create each of the Raman spectra, *S*, using a series of scalars, a_i, and some residual *R* as shown in Equation 1.

$$S = a_1V_1 + a_2V_2 + \cdots a_iV_i + R \qquad \text{(A.1)}$$

The relating score vector relates the a_i scalars to the measured Ellman concentration, c^m. The loading vectors and relating score vector can then be applied to an unknown spectrum and predict the concentration, c^p. The data was analyzed using a cross validation in which all replicate spectra taken at a given AChE data were removed and the loading and relating score vectors were created using the remaining dataset. The removed spectra were then analyzed one at a time using these vectors to predict the concentration of the removed spectra. These results were then compared against the measured values. This was repeated until the concentrations had been predicted for all spectra. The 229 nm data

used 6-8 loading vectors and the 532 nm data used 4-8 loading vectors. These numbers were selected to minimize the root mean squared error of prediction (RMSEP) defined in Equation 2, where *n* is the total number of spectra collected.

$$RMSEP = \sqrt{\frac{\sum_{k=1}^{n}(c_k^m - c_k^p)^2}{n}} \quad \text{(A.2)}$$

In addition to full spectrum analysis, the spectra were truncated so that only certain areas of the spectrum were used in the analysis. Spectral windows around the Raman fingerprint region of 700-1700 cm^{-1} were isolated for analysis, but did not significantly change the results as shown in Table A.1 (532 nm) and Table A.2 (229 nm). Figure A.3 shows the prediction plot for analysis of the 708-1056 cm^{-1} region for 229 nm excitation and 1257-1656 cm^{-1} for 532 nm excitation. The measured Ellman concentrations are along the x-axis and the PLS prediction concentration is along the y-axis. The prediction for the 532 nm data was slightly better than the 229 nm data with a lower RMSEP (0.01247 compared to 0.02255) and a higher Pearson correlation (0.492 compared to 0.238); however the error for both is too large to provide any useful prediction information.

Table A.1. Correlation and RMSEP values for PLS predictions calculated using Raman spectra collected with 532 nm laser excitation.

Spectral Range	Correlation	RMSEP	# of PLS Vectors
562-3991 cm^{-1} (Whole Spectrum)	0.031	0.01524	5
636-1656 cm^{-1}	0.326	0.01394	5
1011- 1447 cm^{-1}	0.351	0.01457	8
1257-1656 cm^{-1}	0.492	0.01247	7
1479-1656 cm^{-1}	0.358	0.01375	6

Table A.2. Correlation and RMSEP value for PLS predictions calculated using Raman spectra collected with 229 nm laser excitation.

Spectral Range	Correlation	RMSEP	# of PLS Vectors
460-3200 cm^{-1} (Whole Spectrum)	0.115	0.02886	8
708-1746 cm^{-1}	0.203	0.02538	8
708-1056 cm^{-1}	0.238	0.02255	6
1104-1810 cm^{-1}	0.150	0.02581	8
1486-1810 cm^{-1}	0.117	0.2566	7

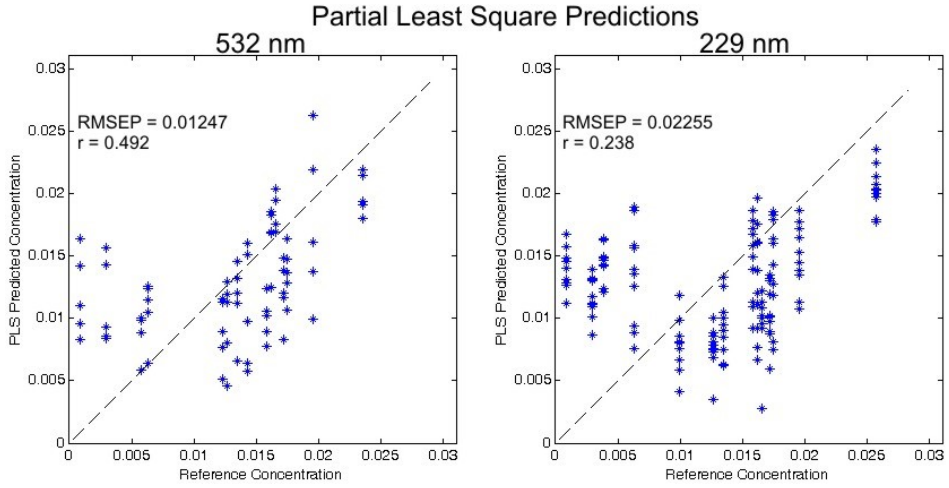

Figure A.3. Comparison of PLS predicted concentrations to Ellman measured values for 532 nm from 1257-1656 cm^{-1} (left) and 229 nm from 708-1056 cm^{-1} (right). Analysis was performed using a cross validation technique. Plots list the RMSEP and Pearson correlation score, r.

During analysis, two trends were noticed. First, the spread of the predicted data was larger than expected. This was attributed to photo damage from the lasers. To mitigate this effect in the calculations, only the first two spectra collected at each concentration was used in the calculations below. Additionally, it was noticed that the data points with low AChE activity had worse correlation than the data points with higher AChE activity. This can be observed by looking at 229 nm data in Figure A.3. The average prediction

concentrations at the concentrations above 0.01 ΔA/min follows a trend in the correct direction, however the average of the prediction values less than 0.01 ΔA/min remains fairly constant. The data was reanalyzed to include only the concentrations above 0.01 ΔA/min with the results shown in Table A.3 and Figure A.4.

Table A.3. Correlation and RMSEP value for PLS predictions calculated using Raman spectra collected with 532 nm laser excitation for samples with concentrations >0.01 ΔA/min.

Spectral Range	Correlation	RMSEP	# of PLS Vectors
562-3991 cm^{-1} (Whole Spectrum)	0.037	0.00602	16
636-1656 cm^{-1}	-0.036	0.00571	3
1011- 1447 cm^{-1}	0.116	0.004938	7
1257-1656 cm^{-1}	0.310	0.00477	7
1479-1656 cm^{-1}	0.233	0.005127	6

Table A.4. Correlation and RMSEP value for PLS predictions calculated using Raman spectra collected with 229 nm laser excitation for samples with concentrations >0.01 ΔA/min.

Spectral Range	Correlation	RMSEP	# of PLS Vectors
460-3200 cm^{-1} (Whole Spectrum)	0.895	0.00230	6
708-1746 cm^{-1}	0.915	0.00208	7
708-1056 cm^{-1}	0.865	0.00284	4
1104-1810 cm^{-1}	0.831	0.00282	3
1486-1810 cm^{-1}	0.940	0.00200	8

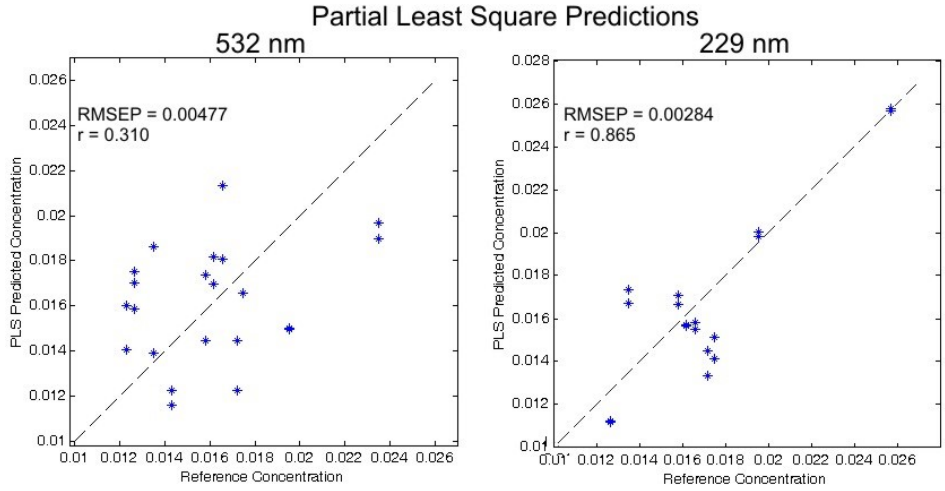

Figure A.4. PLS Prediction plots using the first two spectra at each points where AChE activity was measured at greater than 0.01 ΔA/min for 532 nm from 1257-1656 cm^{-1} (left) and 229 nm from 708-1746 cm^{-1} (right).

The analysis performed in Figure A.4 covers the same the spectral regions as the Figure A.3 analysis (708-1056 cm^{-1} for 229 nm and 1257-1656 cm^{-1} for 532 nm). The RMSEP for both excitation wavelengths decreased and the correlation greatly increased for the 229 nm data. The 229 nm data used four (4) loading vectors and the 532 nm used seven (7). Correlation values above 0.9 were obtained by analyzing the 708-1746 and 1486-1810 cm^{-1} regions of the 229 data using 7 and 8 loading vectors to minimize the RMSEP, respectively. If the number of loading vectors is reduced to 4 (708-1746 cm^{-1}) and 3 (1486-1810 cm^{-1}), the correlations still remain at 0.877 and 0.830. The analysis on this reduced data set points to a limit of detection of approximately 0.01 ΔA/min. For comparison, uninhibited blood varied from 0.17-0.26 ΔA/min in this study.

A.6 Conclusion

There was no main spectral feature that could be directly correlated to AChE activity, however using a multivariate PLS calibration technique focused from 708-1810 cm^{-1} it was possible to predict a trend in AChE activity using Raman spectra using 229 nm excitation. This spectral region includes a number of peaks which changed in intensity and shifted frequency as the AChE levels changed. This does not show the same quality of results as a laboratory technique, but could potentially be used as a screening for a blood draw and more precise measurement using the current methodology. After analyzing the Raman data a limit of detection corresponding to approximately 0.01 ΔA/min was noticed. Removing this data from the training algorithm significantly improved the prediction results. The technique is rapid and reagentless and could be performed on very small blood samples (i.e. finger prick) which could be performed with greater frequency. More frequent measurements would lead to earlier diagnosis and treatment of OP exposure.

From this study, it is unclear whether the spectral changes directly relate to AChE activity or a different chemical reaction related to the introduction of OP compounds to the blood, but ultimately may not matter as long as it is a consistent effect of OP poisoning. This was mitigated in our experiment by using three (3) different OP compounds of varying toxicities.

ACRONYMS

AChE	Acetylcholinesterase
AFM	Atomic Force Microscopy
ATCC	American Type Culture Collection
ATCI	Acetylthiocholine Iodide
BAS	*Bacillus anthracis* Sterne
BAt	*B. atrophaeus*
BM	*B. megaterium*
BT	*B. thuringiensis kurstaki*
BW	Biological Warfare
BWC	Biological Warfare Convention
CaDP	Calcium Dipicolinate
CAS #	Chemical Abstracts Service Registry Number
cfu	Colony Forming Unit
CNR	Contrast to Noise Ratio
DNA	Deoxyribonucleic Acid

DSM	Difco Sporulation Media
DTNB	5,5’-dithiobis(2-nitrobenzoic acid)
FOV	Field of View
NA	Numerical Aperture
NB	Nutrient Broth
OMPA	Octamethyldiphosphoramide
OP	Organophosphate
PCA	Principal Component Analysis
PCR	Polymerase Chain Reaction
PHBA	Polyhydroxybutyric Acid
PLS	Partial Least Squares
PSF	Point Spread Function
qPCR	Quantitative Polymerase Chain Reaction
RHSC	Raman Hyperspectral Cube
RMSEP	Root Mean Squared Error of Prediction
rpm	Revolutions per Minute
SAL	Sterility Assurance Level
SEM	Scanning Electron Microscopy
SERS	Surface Enhanced Raman Spectroscopy
SNR	Signal to Noise Ratio
UV	Ultraviolet

BIBLIOGRAPHY

1. M. K. Jacobs, "The history of biologic warfare and bioterrorism," Dermatol Clin **22**, 231-246, v (2004).
2. S. Riedel, "Biological Warfare and Bioterrorism: A Historical Review," Baylor University Medical Center Proceedings **17**, 400-406 (2004).
3. G. W. Christopher, T. J. Cieslak, J. A. Pavlin, and E. M. Eitzen, Jr, "Biological Warfare: A Historical Perspective," JAMA **278**, 412-417 (1997).
4. R. J. Manchee, M. G. Broster, J. Melling, R. M. Henstridge, and A. J. Stagg, "*Bacillus anthracis* on Gruinard Island," Nature **294**, 254-255 (1981).
5. P. Aldhous, "Gruinard Island handed back," Nature **344**, 801-801 (1990).
6. C. J. Davis, "Nuclear blindness: An overview of the biological weapons programs of the former Soviet Union and Iraq," Emerg Infect Dis **5**, 509-512 (1999).
7. H. J. Jansen, F. J. Breeveld, C. Stijnis, and M. P. Grobusch, "Biological warfare, bioterrorism, and biocrime," Clinical Microbiology and Infection **20**, 488-496 (2014).
8. United States Department of Justice, "Amerithrax Investigative Summary," (2010).

9. D. L. Greenberg, J. D. Busch, P. Keim, and D. M. Wagner, "Identifying experimental surrogates for *Bacillus anthracis* spores: a review," Investigative Genetics **1**, 4 (2010).

10. E. A. Spotts Whitney, M. E. Beatty, T. H. Taylor, Jr., R. Weyant, J. Sobel, M. J. Arduino, and D. A. Ashford, "Inactivation of *Bacillus anthracis* spores," Emerg Infect Dis **9**, 623-627 (2003).

11. W. H. Coleman, D. Chen, Y.-q. Li, A. E. Cowan, and P. Setlow, "How Moist Heat Kills Spores of *Bacillus subtilis*," Journal of Bacteriology **189**, 8458-8466 (2007).

12. C. K. Cote, T. Buhr, C. B. Bernhards, M. D. Bohmke, A. M. Calm, J. S. Esteban-Trexler, M. Hunter, S. E. Katoski, N. Kennihan, C. P. Klimko, J. A. Miller, Z. A. Minter, J. W. Pfarr, A. M. Prugh, A. V. Quirk, B. A. Rivers, A. A. Shea, J. L. Shoe, T. M. Sickler, A. A. Young, D. P. Fetterer, S. L. Welkos, J. A. Bozue, D. McPherson, A. W. Fountain, and H. S. Gibbons, "A Standard Method To Inactivate *Bacillus anthracis* Spores to Sterility via Gamma Irradiation," Applied and Environmental Microbiology **84**, e00106-00118 (2018).

13. L. A. Dauphin, B. R. Newton, M. V. Rasmussen, R. F. Meyer, and M. D. Bowen, "Gamma irradiation can be used to inactivate *Bacillus anthracis* spores without compromising the sensitivity of diagnostic assays," Applied and environmental microbiology **74**, 4427-4433 (2008).

14. V. Majidi, "Review Comittee Report: Inadvertant Shipment of Live *Bacillus Anthracis* Spores by DoD," (Department of Defense, 2015).

15. J. Akers and J. Agalloco, "Sterility and Sterility Assurance," PDA Journal of Pharmaceutical Science and Technology **51**, 72-77 (1997).

16. R. M. Atlas, "The Medical Threat of Biological Weapons," Critical Reviews in Microbiology **24**, 157-168 (1998).

17. T. V. Inglesby, D. A. Henderson, J. G. Bartlett, M. S. Ascher, E. Eitzen, A. M. Friedlander, J. Hauer, J. McDade, M. T. Osterholm, T. O'Toole, G. Parker, T. M. Perl, P. K. Russell, K. Tonat, and f. t. W. G. o. C. Biodefense, "Anthrax as a Biological Weapon Medical and Public Health Management," JAMA **281**, 1735-1745 (1999).

18. A. Driks, "The *Bacillus anthracis* spore," Molecular Aspects of Medicine **30**, 368-373 (2009).

19. P. Setlow, "Spores of *Bacillus subtilis*: their resistance to and killing by radiation, heat and chemicals," Journal of Applied Microbiology **101**, 514-525 (2006).

20. United States Department of Health and Human Services, "Guide to Understanding Anthrax," National Center for Emerging and Zoonotic Infectious Diseases, ed. (2016).

21. C. Paul, S. Filippidou, I. Jamil, W. Kooli, G. L. House, A. Estoppey, M. Hayoz, T. Junier, F. Palmieri, T. Wunderlin, A. Lehmann, S. Bindschedler, T. Vennemann, P. S. G. Chain, and P. Junier, "Bacterial spores, from ecology to biotechnology," Adv Appl Microbiol **106**, 79-111 (2019).

22. R. J. Manchee, M. G. Broster, I. S. Anderson, R. M. Henstridge, and J. Melling, "Decontamination of *Bacillus anthracis* on Gruinard Island?," Nature **303**, 239-240 (1983).

23. N. Ulrich, K. Nagler, M. Laue, C. S. Cockell, P. Setlow, and R. Moeller, "Experimental studies addressing the longevity of *Bacillus subtilis* spores – The first data from a 500-year experiment," PLOS ONE **13**, e0208425 (2018).

24. M. J. Leggett, G. McDonnell, S. P. Denyer, P. Setlow, and J.-Y. Maillard, "Bacterial spore structures and their protective role in biocide resistance," Journal of Applied Microbiology **113**, 485-498 (2012).

25. Centers for Disease Control and Prevention, "Public Health Image Library" (December 20, 2017), retrieved November 7, 2009, https://phil.cdc.gov/Details.aspx?pid=1934.

26. ANSI/AMMI/ISO, "Sterilization of medical devices – Microbiological methods," in *Part 2: Tests of viability performed in the definition, validation and maintenance of a sterilization process,* (2014).

27. A. Martinon, U. P. Cronin, J. Quealy, A. Stapleton, and M. G. Wilkinson, "Swab sample preparation and viable real-time PCR methodologies for the recovery of Escherichia coli, Staphylococcus aureus or Listeria monocytogenes from artificially contaminated food processing surfaces," Food Control **24**, 86-94 (2012).

28. A. Rueckert, R. S. Ronimus, and H. W. Morgan, "Rapid differentiation and enumeration of the total, viable vegetative cell and spore content of thermophilic bacilli in milk powders with reference to *Anoxybacillus flavithermus*," Journal of Applied Microbiology **99**, 1246-1255 (2005).

29. P. R. Murray, K. S. Rosenthal, and M. A. Pfaller, *Medical Microbiology,* 8 ed. (Elsevier Health Sciences, Philadelphia, PA, 2016).

30. M. G. Wilkinson, "Flow cytometry as a potential method of measuring bacterial viability in probiotic products: A review," Trends in Food Science & Technology **78**, 1-10 (2018).

31. P. D'Incecco, L. Ong, S. Gras, and L. Pellegrino, "A fluorescence in situ staining method for investigating spores and vegetative cells of Clostridia by confocal laser scanning microscopy and structured illuminated microscopy," Micron **110**, 1-9 (2018).

32. H. Firstencel, T. M. Butt, and R. I. Carruthers, "A fluorescence microscopy method for determining the viability of entomophthoralean fungal spores," Journal of Invertebrate Pathology **55**, 258-264 (1990).

33. L. C. Green, P. J. LeBlanc, and E. S. Didier, "Discrimination between viable and dead Encephalitozoon cuniculi (Microsporidian) spores by dual staining with sytox green and calcofluor white M2R," Journal of clinical microbiology **38**, 3811-3814 (2000).

34. H. S. Shafaat and A. Ponce, "Applications of a rapid endospore viability assay for monitoring UV inactivation and characterizing arctic ice cores," Applied and environmental microbiology **72**, 6808-6814 (2006).

35. W.-W. Yang and A. Ponce, "Rapid endospore viability assay of Clostridium sporogenes spores," International Journal of Food Microbiology **133**, 213-216 (2009).

36. K. S. Kalasinsky, T. Hadfield, A. A. Shea, V. F. Kalasinsky, M. P. Nelson, J. Neiss, A. J. Drauch, G. S. Vanni, and P. J. Treado, "Raman Chemical Imaging

Spectroscopy Reagentless Detection and Identification of Pathogens: Signature Development and Evaluation," Analytical Chemistry **79**, 2658-2673 (2007).

37. A. Tripathi, R. E. Jabbour, J. A. Guicheteau, S. D. Christesen, D. K. Emge, A. W. Fountain, J. R. Bottiger, E. D. Emmons, and A. P. Snyder, "Bioaerosol Analysis with Raman Chemical Imaging Microspectroscopy," Analytical Chemistry **81**, 6981-6990 (2009).

38. A. Tripathi, R. E. Jabbour, P. J. Treado, J. H. Neiss, M. P. Nelson, J. L. Jensen, and A. P. Snyder, "Waterborne Pathogen Detection Using Raman Spectroscopy," Applied Spectroscopy **62**, 1-9 (2008).

39. H.-W. Cheng, Y.-Y. Chen, X.-X. Lin, S.-Y. Huan, H.-L. Wu, G.-L. Shen, and R.-Q. Yu, "Surface-enhanced Raman spectroscopic detection of *Bacillus subtilis* spores using gold nanoparticle based substrates," Analytica Chimica Acta **707**, 155-163 (2011).

40. J. Guicheteau, L. Argue, D. Emge, A. Hyre, M. Jacobson, and S. Christesen, "*Bacillus* Spore Classification via Surface-Enhanced Raman Spectroscopy and Principal Component Analysis," Applied Spectroscopy **62**, 267-272 (2008).

41. R. M. Jarvis, A. Brooker, and R. Goodacre, "Surface-enhanced Raman scattering for the rapid discrimination of bacteria," Faraday Discussions **132**, 281-292 (2006).

42. P. Zhang, L. Kong, P. Setlow, and Y.-q. Li, "Characterization of Wet-Heat Inactivation of Single Spores of *Bacillus* Species by Dual-Trap Raman Spectroscopy and Elastic Light Scattering," Applied and Environmental Microbiology **76**, 1796-1805 (2010).

43. P. Zhang, L. Kong, G. Wang, P. Setlow, and Y.-q. Li, "Monitoring the Wet-Heat Inactivation Dynamics of Single Spores of *Bacillus* Species by Using Raman Tweezers, Differential Interference Contrast Microscopy, and Nucleic Acid Dye Fluorescence Microscopy," Applied and Environmental Microbiology **77**, 4754-4769 (2011).

44. S. Wang, C. J. Doona, P. Setlow, and Y.-q. Li, "Use of Raman Spectroscopy and Phase-Contrast Microscopy To Characterize Cold Atmospheric Plasma Inactivation of Individual Bacterial Spores," Applied and Environmental Microbiology **82**, 5775-5784 (2016).

45. Centers for Disease Control and Prevention, "Anthrax Sterne strain (34F2) of *Bacillus anthracis*" (August 27, 2009), retrieved November 2, 2019, https://www.cdc.gov/nczved/divisions/dfbmd/diseases/anthrax_sterne/.

46. S. Inoué and R. Oldenbourg, "Microscopes," in *Handbook of Optics,* 2nd Edition ed., M. Bass, ed. (McGraw-Hill, New York, 1995).

47. D. Coling and B. Kachar, "Theory and Application of Fluorescence Microscopy," Current Protocols in Neuroscience **00**, 2.1.1-2.1.11 (1997).

48. C. A. Combs, "Fluorescence microscopy: a concise guide to current imaging methods," Current protocols in neuroscience **Chapter 2**, Unit2.1-Unit2.1 (2010).

49. J. Goldstein, D. Newbury, D. Joy, C. Lyman, P. Echlin, E. Lifshin, L. Sawyer, and J. Michael, *Scanning Electron Microscopy and X-Ray Microanalysis,* Third Edition ed. (Springer US, New York, 2003).

50. N. Jalili and K. Laxminarayana, "A review of atomic force microscopy imaging systems: application to molecular metrology and biological sciences," Mechatronics **14**, 907-945 (2004).

51. T. Hashimoto, W. R. Frieben, and S. F. Conti, "Germination of Single Bacterial Spores," Journal of Bacteriology **98**, 1011-1020 (1969).

52. A. D. Hitchins, A. J. Kahn, and R. A. Slepecky, "Interference Contrast and Phase Contrast Microscopy of Sporulation and Germination of *Bacillus megaterium*," Journal of Bacteriology **96**, 1811-1817 (1968).

53. L. Kong, C. J. Doona, P. Setlow, and Y.-q. Li, "Monitoring Rates and Heterogeneity of High-Pressure Germination of *Bacillus* Spores by Phase-Contrast Microscopy of Individual Spores," Applied and Environmental Microbiology **80**, 345-353 (2014).

54. L. Kong, P. Zhang, P. Setlow, and Y.-q. Li, "Characterization of Bacterial Spore Germination Using Integrated Phase Contrast Microscopy, Raman Spectroscopy, and Optical Tweezers," Analytical Chemistry **82**, 3840-3847 (2010).

55. L. Kong, P. Zhang, G. Wang, J. Yu, P. Setlow, and Y.-q. Li, "Characterization of bacterial spore germination using phase-contrast and fluorescence microscopy, Raman spectroscopy and optical tweezers," Nature Protocols **6**, 625-639 (2011).

56. J. Liang, P. Zhang, P. Setlow, and Y.-Q. Li, "High-Precision Fitting Measurements of the Kinetics of Size Changes during Germination of Individual *Bacillus* Spores," Applied and Environmental Microbiology **80**, 4606-4615 (2014).

57. M. E. Sharpe, P. M. Hauser, R. G. Sharpe, and J. Errington, "*Bacillus subtilis* Cell Cycle as Studied by Fluorescence Microscopy: Constancy of Cell Length at

Initiation of DNA Replication and Evidence for Active Nucleoid Partitioning," Journal of Bacteriology **180**, 547-555 (1998).

58. P. Zhang, L. Kong, G. Wang, M. Scotland, S. Ghosh, B. Setlow, P. Setlow, and Y.-Q. Li, "Analysis of the slow germination of multiple individual superdormant *Bacillus subtilis* spores using multifocus Raman microspectroscopy and differential interference contrast microscopy," Journal of Applied Microbiology **112**, 526-536 (2012).

59. S. Wang, J. R. Faeder, P. Setlow, and Y.-q. Li, "Memory of Germinant Stimuli in Bacterial Spores," mBio **6**, e01859-01815 (2015).

60. C. Robinow and E. Kellenberger, "The bacterial nucleoid revisited," Microbiological Reviews **58**, 211-232 (1994).

61. A. M. Glauert, E. M. Brieger, and J. M. Allen, "The fine structure of vegetative cells of *Bacillus subtilis*," Experimental Cell Research **22**, 73-85 (1961).

62. D. A. Wood, "Sporulation in *Bacillus subtilis*. Properties and time of synthesis of alkali-soluble protein of the spore coat," Biochem J **130**, 505-514 (1972).

63. R. A. Zolock, G. Li, C. Bleckmann, L. Burggraf, and D. C. Fuller, "Atomic force microscopy of *Bacillus* spore surface morphology," Micron **37**, 363-369 (2006).

64. J. C. Fernandes, P. Eaton, A. M. Gomes, M. E. Pintado, and F. Xavier Malcata, "Study of the antibacterial effects of chitosans on *Bacillus cereus* (and its spores) by atomic force microscopy imaging and nanoindentation," Ultramicroscopy **109**, 854-860 (2009).

65. G. Keresztury, "Raman Spectroscopy: Theory," in *Handbook of Vibrational Spectroscopy*, J. M. Chalmers and P. R. Griffiths, eds. (John Wiley & Sons Ltd., New York, NY, 2002), pp. 71-87.

66. S. A. Asher, "UV resonance Raman spectroscopy for analytical, physical, and biophysical chemistry. Part 1," Analytical Chemistry **65**, 59A-66A (1993).

67. J. De Gelder, K. De Gussem, P. Vandenabeele, and L. Moens, "Reference database of Raman spectra of biological molecules," Journal of Raman Spectroscopy **38**, 1133-1147 (2007).

68. K. Maquelin, C. Kirschner, L. P. Choo-Smith, N. van den Braak, H. P. Endtz, D. Naumann, and G. J. Puppels, "Identification of medically relevant microorganisms by vibrational spectroscopy," Journal of Microbiological Methods **51**, 255-271 (2002).

69. A. A. Gowen, Y. Feng, E. Gaston, and V. Valdramidis, "Recent applications of hyperspectral imaging in microbiology," Talanta **137**, 43-54 (2015).

70. J. Ma and D. Ben-Amotz, "Rapid Micro-Raman Imaging Using Fiber-Bundle Image Compression," Applied Spectroscopy **51**, 1845-1848 (1997).

71. S. Stewart, R. J. Priore, M. P. Nelson, and P. J. Treado, "Raman Imaging," Annual Review of Analytical Chemistry **5**, 337-360 (2012).

72. O. Hollricher and W. Ibach, "High-Resolution Optical and Confocal Microscopy," in *Confocal Raman Microscopy*, T. Dieing, O. Hollricher, and J. Toporski, eds. (Springer-Verlag, Berlin, 2011), pp. 1-42.

73. R. H. Webb, "Confocal optical microscopy," Reports on Progress in Physics **59**, 427-471 (1996).

74. S. Farquharson, C. Shende, W. Smith, H. Huang, F. Inscore, A. Sengupta, J. Sperry, T. Sickler, A. Prugh, and J. Guicheteau, "Selective detection of 1000 *B. anthracis* spores within 15 minutes using a peptide functionalized SERS assay," Analyst **139**, 6366-6370 (2014).

75. W. H. Woodruff, T. G. Spiro, and C. Gilvarg, "Raman spectroscopy *in vivo*: Evidence on the structure of dipicolinate in intact spores of *Bacillus megaterium*," Biochemical and Biophysical Research Communications **58**, 197-203 (1974).

76. A. P. Esposito, C. E. Talley, T. Huser, C. W. Hollars, C. M. Schaldach, and S. M. Lane, "Analysis of Single Bacterial Spores by Micro-Raman Spectroscopy," Applied Spectroscopy **57**, 868-871 (2003).

77. H. Shibata, S. Yamashita, M. Ohe, and I. Tani, "Laser Raman Spectroscopy of Lyophilized Bacterial Spores," Microbiology and Immunology **30**, 307-313 (1986).

78. G. Rusciano, G. Zito, R. Isticato, T. Sirec, E. Ricca, E. Bailo, and A. Sasso, "Nanoscale Chemical Imaging of *Bacillus subtilis* Spores by Combining Tip-Enhanced Raman Scattering and Advanced Statistical Tools," ACS Nano **8**, 12300-12309 (2014).

79. J. W. Chan, A. P. Esposito, C. E. Talley, C. W. Hollars, S. M. Lane, and T. Huser, "Reagentless Identification of Single Bacterial Spores in Aqueous Solution by Confocal Laser Tweezers Raman Spectroscopy," Analytical Chemistry **76**, 599-603 (2004).

80. P. Zhang, P. Setlow, and Y. Li, "Characterization of single heat-activated *Bacillus* spores using laser tweezers Raman spectroscopy," Opt. Express **17**, 16480-16491 (2009).

81. A. E. Carpenter, T. R. Jones, M. R. Lamprecht, C. Clarke, I. H. Kang, O. Friman, D. A. Guertin, J. H. Chang, R. A. Lindquist, J. Moffat, P. Golland, and D. M. Sabatini, "CellProfiler: image analysis software for identifying and quantifying cell phenotypes," Genome Biology **7**, R100 (2006).

82. J. Schindelin, I. Arganda-Carreras, E. Frise, V. Kaynig, M. Longair, T. Pietzsch, S. Preibisch, C. Rueden, S. Saalfeld, B. Schmid, J.-Y. Tinevez, D. J. White, V. Hartenstein, K. Eliceiri, P. Tomancak, and A. Cardona, "Fiji: an open-source platform for biological-image analysis," Nature Methods **9**, 676 (2012).

83. Y. Fang, C. Zheng, C. Pan, and L. Liu, "White Blood Cell Image Segmentation Using On-line Trained Neural Network," in *2005 IEEE Engineering in Medicine and Biology 27th Annual Conference*, 2005), 6476-6479.

84. C. Fatichah, D. Purwitasari, V. Hariadi, and F. Effendy, "Overlapping white blood cell segmentation and counting on microscopic blood cell images," International Journal on Smart Sensing and Intelligent Systems **7**, 1271 – 1286 (2014).

85. J. Kan, L. Qing-Min, and D. Sheng-Yang, "A novel white blood cell segmentation scheme using scale-space filtering and watershed clustering," in *Proceedings of the 2003 International Conference on Machine Learning and Cybernetics (IEEE Cat. No.03EX693)*, 2003), 2820-2825 Vol.2825.

86. F. Buggenthin, C. Marr, M. Schwarzfischer, P. S. Hoppe, O. Hilsenbeck, T. Schroeder, and F. J. Theis, "An automatic method for robust and fast cell detection in bright field images from high-throughput microscopy," BMC Bioinformatics **14**, 297 (2013).

87. I. Simon, C. R. Pound, A. W. Partin, J. Q. Clemens, and W. A. Christens-Barry, "Automated image analysis system for detecting boundaries of live prostate cancer cells," Cytometry **31**, 287-294 (1998).

88. C. Jung, C. Kim, S. W. Chae, and S. Oh, "Unsupervised Segmentation of Overlapped Nuclei Using Bayesian Classification," IEEE Transactions on Biomedical Engineering **57**, 2825-2832 (2010).

89. N. Malpica, C. O. de Solórzano, J. J. Vaquero, A. Santos, I. Vallcorba, J. M. García-Sagredo, and F. del Pozo, "Applying watershed algorithms to the segmentation of clustered nuclei," Cytometry **28**, 289-297 (1997).

90. M. Tscherepanow, F. Zöllner, M. Hillebrand, and F. Kummert, "Automatic Segmentation of Unstained Living Cells in Bright-Field Microscope Images," in Advances in Mass Data Analysis of Images and Signals in Medicine, Biotechnology, Chemistry and Food Industry (Springer Berlin Heidelberg, 2008), 158-172.

91. C. L. Jones, G. T. Lonergan, and D. E. Mainwaring, "The use of image analysis for spore counts of white-rot fungi," Biotechnology Techniques **6**, 417-422 (1992).

92. R. Korsnes, K. Westrum, E. Fløistad, and I. Klingen, "Computer-assisted image processing to detect spores from the fungus Pandora neoaphidis," MethodsX **3**, 231-241 (2016).

93. S. Nasr-Isfahani, A. Mirsafian, and A. Masoudi-Nejad, "A New Approach for Touching Cells Segmentation," in *2008 International Conference on BioMedical Engineering and Informatics*, 2008), 816-820.

94. K.-B. Oh, Y. Chen, H. Matsuoka, A. Yamamoto, and H. Kurata, "Morphological recognition of fungal spore germination by a computer-aided image analysis and its application to antifungal activity evaluation," Journal of Biotechnology **45**, 71-79 (1996).

95. P. Perner, S. Jänichen, and H. Perner, "Case-based object recognition for airborne fungi recognition," Artificial Intelligence in Medicine **36**, 137-157 (2006).

96. J. Wagner and J. Macher, "Automated Spore Measurements Using Microscopy, Image Analysis, and Peak Recognition of Near-Monodisperse Aerosols," Aerosol Science and Technology **46**, 862-873 (2012).

97. P. Xu and J. Li, "Computer Assistance Image Processing Spores Counting," in *2009 International Asia Conference on Informatics in Control, Automation and Robotics*, 2009), 203-206.

98. E. Bengtsson, C. Wahlby, and J. Lindblad, "Robust cell image segmentation methods," Pattern Recognition and Image Analysis C/c of Raspoznavaniye Obrazov i Analiz Izobrazhenii. **14**, 157-167 (2004).

99. E. Meijering, "Cell Segmentation: 50 Years Down the Road," IEEE Signal Processing Magazine **29**, 140-145 (2012).

100. S. Beucher and F. Meyer, "The Morphological approach of segmentation: the watershed transformation," in *Mathematical Morphology in Image Processing*, E. R. Dougherty, ed. (CRC Press, New York, New York, 1992), pp. 433-481.

101. M. Carrera, R. O. Zandomeni, J. Fitzgibbon, and J. L. Sagripanti, "Difference between the spore sizes of *Bacillus anthracis* and other *Bacillus* species," Journal of Applied Microbiology **102**, 303-312 (2007).

102. T. L. Buhr, A. A. Young, Z. A. Minter, C. M. Wells, D. C. McPherson, C. L. Hooban, C. A. Johnson, E. J. Prokop, and J. R. Crigler, "Test method development to evaluate hot, humid air decontamination of materials contaminated with *Bacillus anthracis* ΔSterne and *B. thuringiensis* Al Hakam spores," Journal of Applied Microbiology **113**, 1037-1051 (2012).

103. B. A. Ramsay, K. Lomaliza, C. Chavarie, B. Dubé, P. Bataille, and J. A. Ramsay, "Production of poly-(beta-hydroxybutyric-co-beta-hydroxyvaleric) acids," Applied and environmental microbiology **56**, 2093-2098 (1990).

104. K.-H. Law, Y.-C. Leung, H. Lawford, H. Chua, W.-H. Lo, and P. H. Yu, "Production of polyhydroxybutyrate by *Bacillus* species isolated from municipal activated sludge," Applied Biochemistry and Biotechnology **91**, 515-524 (2001).

105. G. Strahs and R. E. Dickerson, "The crystal structure of calcium dipicolinate trihydrate (a bacterial spore metabolite)," Acta Crystallographica Section B **24**, 571-578 (1968).

106. B. Setlow, S. Atluri, R. Kitchel, K. Koziol-Dube, and P. Setlow, "Role of Dipicolinic Acid in Resistance and Stability of Spores of *Bacillus subtilis* with or without DNA-Protective α/β-Type Small Acid-Soluble Proteins," Journal of Bacteriology **188**, 3740-3747 (2006).

107. A. Dychalska, P. Popielarski, W. Franków, K. Fabisiak, K. Paprocki, and M. Szybowicz, "Study of CVD diamond layers with amorphous carbon admixture by Raman scattering spectroscopy," **33**, 799 (2015).

108. H. Abdi and L. J. Williams, "Principal component analysis," Wiley Interdisciplinary Reviews: Computational Statistics **2**, 433-459 (2010).

109. I. T. Jolliffe and J. Cadima, "Principal component analysis: a review and recent developments," Philosophical Transactions of the Royal Society A: Mathematical, Physical and Engineering Sciences **374**, 20150202 (2016).

110. T. J. Ronningen, J. M. Schuetter, J. L. Wightman, A. Murdock, and A. P. Bartko, "Raman spectroscopy for biological identification," in *Biological Identification*, R. P. Schaudies, ed. (Woodhead Publishing, 2014), pp. 313-333.

111. P. J. Yunker, T. Still, M. A. Lohr, and A. G. Yodh, "Suppression of the coffee-ring effect by shape-dependent capillary interactions," Nature **476**, 308-311 (2011).

112. B. W. Kammrath, A. Koutrakos, J. Castillo, C. Langley, and D. Huck-Jones, "Morphologically-directed Raman spectroscopy for forensic soil analysis," Forensic Science International **285**, e25-e33 (2018).

113. A. Tripathi, E. D. Emmons, P. G. Wilcox, J. A. Guicheteau, D. K. Emge, S. D. Christesen, and A. W. Fountain III, "Semi-Automated Detection of Trace Explosives in Fingerprints on Strongly Interfering Surfaces with Raman Chemical Imaging," Applied Spectroscopy **65**, 611-619 (2011).

114. C. A. Burtis and E. R. Ashwood, *Tietz Fundamentals of Clinical Chemistry* (W.B. Saunders Company, Philadelphia, PA, 2001).

115. G. L. Ellman, K. D. Courtney, V. Andres, and R. M. Featherstone, "A new and rapid colorimetric determination of acetylcholinesterase activity," Biochemical Pharmacology **7**, 88-95 (1961).

116. J. R. Haigh, L. J. Lefkowitz, B. R. Capacio, B. P. Doctor, and R. K. Gordon, "Advantages of the WRAIR whole blood cholinesterase assay: Comparative

analysis to the micro-Ellman, Test-mate ChE™, and Michel (ΔpH) assays," Chemico-Biological Interactions **175**, 417-420 (2008).

117. A. J. Berger, T.-W. Koo, I. Itzkan, G. Horowitz, and M. S. Feld, "Multicomponent Blood Analysis by Near-Infrared Raman Spectroscopy," Appl. Opt. **38**, 2916-2926 (1999).

118. A. M. K. Enejder, T.-W. Koo, J. Oh, M. Hunter, S. Sasic, M. S. Feld, and G. L. Horowitz, "Blood analysis by Raman spectroscopy," Opt. Lett. **27**, 2004-2006 (2002).

119. D. M. Haaland and E. V. Thomas, "Partial least-squares methods for spectral analyses. 1. Relation to other quantitative calibration methods and the extraction of qualitative information," Analytical Chemistry **60**, 1193-1202 (1988).

BIOGRAPHY

Phillip G. Wilcox was born in 1982 in the USA.

Phillip completed his undergraduate studies at the University of Delaware where he majored in Electrical Engineering with a concentration in semiconductor devices and materials while also minoring in Physics and Material Science.

After graduation he worked for a short time at Northrop Grumman before getting a job at the US Army Edgewood Chemical Biological Center (now known as the Combat Capabilities Development Command Chemical Biological Center) in 2005. Phillip has worked on the Spectroscopy Branch since that time, performing basic and applied research to detect and identify chemical and biological hazards using Raman spectroscopy.

In 2008, he earned a Master's degree in Electrical Engineering with a concentration in Photonics from Johns Hopkins University's Engineering and Applied Science Program for Professionals.

He began his Ph.D. studies in 2009 while continuing his work as a civilian employee of the US Army.

PUBLICATIONS

1. Tripathi A, Emmons ED, **Wilcox PG**, Guicheteau JA, Emge DK, Christesen SD, et al. Semi-Automated Detection of Trace Explosives in Fingerprints on Strongly Interfering Surfaces with Raman Chemical Imaging. *Applied Spectroscopy*. 2011;65(6):611-9.
2. Guicheteau JA, Swofford H, Tripathi A, **Wilcox PG**, Emmons ED, Christesen SD, et al. Sequential Raman Chemical Imaging and Biometric Analysis on Fingerprints for Rapid Identification of Threat Materials and Individuals. *Journal of Forensic Identification*. 2013;63(1):90-101.
3. Guicheteau, J., S. Christesen, D. Emge, **P. Wilcox** and A. W. Fountain III (2011). "Assessing Metal Nanofabricated Substrates for Surface-Enhanced Raman Scattering (SERS) Activity and Reproducibility." *Applied Spectroscopy* 65: 144-151.
4. Guicheteau, J. A., M. E. Farrell, S. D. Christesen, A. W. Fountain, P. M. Pellegrino, E. D. Emmons, A. Tripathi, **P. Wilcox** and D. Emge (2013). "Surface-Enhanced Raman Scattering (SERS) Evaluation Protocol for Nanometallic Surfaces." *Applied Spectroscopy* 67(4): 396-403.
5. **Phillip G. Wilcox**, Jin U. Kang, "Raman spectroscopic analysis of whole blood acetylcholinesterase," Proc. SPIE 9112, Sensing Technologies for Global Health, Military Medicine, and Environmental Monitoring IV, 91120V (5 June 2014)
6. **Phillip G. Wilcox**, Jason A. Guicheteau, "Comparison of handheld Raman sensors through opaque containers," Proc. SPIE 10629, Chemical, Biological,

Radiological, Nuclear, and Explosives (CBRNE) Sensing XIX, 106290M (16 May 2018)

7. Ashish Tripathi, Rabih E. Jabbour, Jason A. Guicheteau, **Phillip G. Wilcox**, A. Peter Snyder, "Biomolecule Raman spectral temporal flux from resting *Bacillus* spores in deionized water matrix," Proc. SPIE 8358, Chemical, Biological, Radiological, Nuclear, and Explosives (CBRNE) Sensing XIII, 83580D (5 May 2012)
8. Jason Guicheteau, Ashish Tripathi, Jennifer Minter, **Phillip Wilcox**, Steven Christesen, "Fate study of water-borne gram positive vegetative bacterial cells with Raman microscopy," Proc. SPIE 7665, Chemical, Biological, Radiological, Nuclear, and Explosives (CBRNE) Sensing XI, 766502 (5 May 2010)
9. Eric Roy, **Phillip G. Wilcox**, Soren Hoffland, Ian Pardoe, "Detection of munitions grade g-series nerve agents using Raman excitation at 1064 nm," Proc. SPIE 9455, Chemical, Biological, Radiological, Nuclear, and Explosives (CBRNE) Sensing XVI, 94550V (19 May 2015)
10. Jason A. Guicheteau, Steven D. Christesen, Ashish Tripathi, Erik D. Emmons, **Phillip G. Wilcox**, Darren K. Emge, Ian J. Pardoe, Augustus W. Fountain, "Proximal and point detection of contaminated surfaces using Raman spectroscopy," Proc. SPIE 8189, Optics and Photonics for Counterterrorism and Crime Fighting VII; Optical Materials in Defence Systems Technology VIII; and Quantum-Physics-based Information Security, 818902 (13 October 2011)
11. Jason A. Guicheteau, Mikella E. Hankus, Steven D. Christesen, Augustus Way Fountain, Paul M. Pellegrino, Erik D. Emmons, Ashish Tripathi, **Phillip Wilcox**,

Darren Emge, "Standard method for characterizing SERS substrates," Proc. SPIE 8373, Micro- and Nanotechnology Sensors, Systems, and Applications IV, 837320 (3 May 2012)

12. Jason A. Guicheteau, Ashish Tripathi, McKay Allred, Tattianna Olvera, Erik D. Emmons, **Phillip G. Wilcox**, Kevin Hung, Anthony Koertner, Augustus W. Fountain, "Chemical fingerprint identification system: beyond concept and towards applications for field expeditionary military forensic analysis," Proc. SPIE 10802, Counterterrorism, Crime Fighting, Forensics, and Surveillance Technologies II, 1080208 (8 October 2018)
13. Ashish Tripathi, Erik D. Emmons, Jason A. Guicheteau, Steven D. Christesen, **Phillip G. Wilcox**, Darren K. Emge, Augustus W. Fountain, "Trace explosive detection in fingerprints with Raman chemical imaging," Proc. SPIE 7665, Chemical, Biological, Radiological, Nuclear, and Explosives (CBRNE) Sensing XI, 76650N (28 April 2010)

Oral Presentations

1. **Wilcox, PG**; Tripathi, A; Kim, MH; Kang, JU; “Bright-Field Segmentation and Registration of Raman Hyperspectral Images for Single Spore Analysis.” Federation of Analytical Chemistry and Spectroscopy Societies 2018 SCIX Conference (Atlanta, GA, October 23, 2018)
2. **Wilcox, PG**; Guicheteau, JA; Tripathi, A; Kim, MH; Emmons, ED; Buhr, A; Cote C; Bozue, J; Gibbons, HS; Kang, JU, “Raman Chemical Imaging Based Cell Cytometry: Differentiation and Quantification of Viable and Gamma Deactivated

B. anthracis Sterne Spores." Federation of Analytical Chemistry and Spectroscopy Societies 2017 SCIX Conference (Reno, NV, October 12, 2017)

3. **Wilcox, PG**, Guicheteau, JA; Tripathi, A; Christesen, SD, "Spatially Offset Raman Spectroscopic Probe for Through Barrier Identification," Federation of Analytical Chemistry and Spectroscopy Societies 2016 SCIX Conference (Minneapolis, MN, October 20, 2016)
4. **Wilcox, PG**; Kang, JU, "Raman Spectroscopic Analysis of Whole Sheep's Blood Acetylcholinesterase." SPIE Sensing Technology + Applications 2014 (Baltimore, MD, May 6, 2014)
5. **Wilcox, PG**; Guicheteau, JA; Tripathi, A; Christesen, SD, "Proximal Raman Detection of Chemicals and Explosives on Surfaces." Federation of Analytical Chemistry and Spectroscopy Societies Conference 2011 (Reno, NV, October 6, 2011)
6. **Wilcox, PG**; Pardoe, IJ; Guicheteau, JA; Christesen, SD; Emge, DK, Effect of Laser Angle Interrogation on Raman Signal." Federation of Analytical Chemistry and Spectroscopy Societies Conference 2010 (Raleigh, NC, October 18, 2010)
7. **Wilcox, PG**; Guicheteau, JA; Tripathi, A, "Spatially Offset Raman Spectroscopy for Subsurface Chemical Detection." 2009 Defense Threat Reduction Agency Chemical and Biological Defense S&T Conference (Dallas, TX, November 19, 2009)